Direct and indirect cholinergic septo-hippocampal pathways cooperate to structure spiking activity in the hippocampus

Dissertation
zur
Erlangung des Doktorgrades (Dr. rer. nat.)
der
Mathematisch-Naturwissenschaftlichen Fakultät
der
Rheinischen Friedrich-Wilhelms-Universität Bonn

vorgelegt von

Holger Dannenberg

aus
Köln

Bonn, 2015

Angefertigt mit Genehmigung der Mathematisch-Naturwissenschaftlichen
Fakultät der
Rheinischen Friedrich-Wilhelms-Universität Bonn

1. Gutachter: Prof. Dr. Heinz Beck
2. Gutachter: Prof. Dr. Walter Witke

Tag der Promotion: 16.09.2015
Erscheinungsjahr: 2015

Erklärung

Hiermit erkläre ich, dass ich die vorliegende Dissertation selbständig angefertigt habe. Es wurden nur die in der Arbeit ausdrücklich benannten Quellen und Hilfsmittel benutzt. Wörtlich oder sinngemäß übernommenes Gedankengut habe ich als solches kenntlich gemacht.

Ort, Datum Unterschrift

Summary

The medial septum/vertical diagonal band of Broca complex (MSvDB) is a key structure that modulates hippocampal rhythmogenesis. Cholinergic neurons of the MSvDB play a central role in generating and pacing theta-band oscillations in the hippocampal formation during exploration, novelty detection, and memory encoding. However, how precisely cholinergic neurons affect hippocampal oscillatory activity and spiking rates of hippocampal neurons *in vivo*, has remained elusive. I therefore used silicon probe recordings of local field potentials and unit activity in the dorsal hippocampus in combination with cell type specific optogenetic activation of cholinergic MSvDB neurons to study the effects of synaptically released acetylcholine on hippocampal network activity in urethane-anesthetized mice. *In vivo* optogenetic activation of cholinergic MSvDB neurons induced hippocampal rhythmogenesis at the theta (3–6 Hz) and slow gamma (26–48 Hz) frequency range with a suppression of peri-theta frequencies. Interestingly, this effect was independent from the stimulation frequency. In addition, stimulation of cholinergic MSvDB neurons resulted in a net increase of interneuron firing with a concomitant net decrease of principal cell firing in the hippocampal CA3 subfield. I used focal injections of cholinergic blockers either into the MSvDB or the hippocampus to demonstrate that cholinergic MSvDB neurons modulate hippocampal network activity via two distinct pathways. Focal injection of a cholinergic blocker cocktail into the hippocampus strongly diminished the cholinergic stimulation-induced spiking rate modulation of hippocampal interneurons and principal cells. This demonstrates that modulation of neuronal activity in hippocampal subfield CA3 by cholinergic MSvDB neurons is mediated via direct septo-hippocampal projections. In contrast, focal injection of atropine, a blocker of the muscarinic type of acetylcholine receptors, into the MSvDB had no effect on spiking rate modulation in CA3, but abolished hippocampal theta synchronization. This strongly suggests that activity of an indirect septo-hippocampal pathway induces hippocampal theta oscillations via an intraseptal relay. Furthermore, cholinergic neurons depolarized parvalbumin-positive (PV^+) GABAergic neurons within the MSvDB *in vitro*, and optogenetic activation of these fast spiking neurons *in vivo* induced hippocampal rhythmic activity precisely at the stimulation frequency. Taken together, these data suggest an intraseptal relay with a strong contribution of PV^+ GABAergic MSvDB neurons in pacing hippocampal theta oscillations. Activation of both the direct and indirect pathways causes a reduction in CA3 pyramidal neuron firing and a more precise coupling to theta oscillatory phase with CA3 interneurons preferentially firing at the descending phase and CA3 principal neurons preferentially firing near the trough of the ongoing theta oscillation recorded at the pyramidal cell layer. The two identified anatomically and functionally distinct pathways are likely relevant for cholinergic control of encoding vs. retrieval modes in the hippocampus.

Contents

1. Introduction

1.1. The hippocampus as a memory system

The hippocampal formation is known to play a key role in the formation of episodic memories in humans and spatial memories in rodents. One famous example of its critical role in encoding episodic memory in humans is the epilepsy patient Henry Gustav Molaison (widely known as patient H.M., 1926–2008). After the bilateral resection of large parts of the hippocampal formation, he was free of epileptic seizures, but could not acquire new episodic memories for the rest of his life (Scoville and Milner, 1957). Notably, performance in working memory tasks and procedural memory were spared from this anterograde amnesia. In rodents, the hippocampus initially attained a lot of interest due to the discovery of "place cells" in freely moving rats (O'Keefe and Dostrovsky, 1971). These cells are named after their property to fire only at specific locations during the passage through an environment. This discovery stimulated rodent research on the role of the hippocampal formation for spatial memory and allocentric navigation through space. Later studies revealed cells with similar place-selective firing patterns as hippocampal place cells to be present also in the subiculum (Sharp and Green, 1994) and the medial entorhinal cortex (Quirk et al., 1992). Based mainly on the properties of hippocampal place cells, John O'Keefe and Lynn Nadel introduced a theoretical framework, in which the hippocampus serves as a cognitive map (O'Keefe and Nadel, 1978). This theory of a cognitive map was further supported in the following years by the discovery of grid- (Hafting et al., 2005), head-direction- (Taube et al., 1990), and boundary vector cells (Lever et al., 2009). Grid cells were first discovered in the medial entorhinal cortex (Hafting et al., 2005), but later also found in the pre- and parasubiculum (Boccara et al., 2010). The defining characteristic of grid cells is that they fire at equally spaced triangularly distributed locations in space. If one imagines lines between these locations, the resulting picture would appear as a grid, inspiring their name. The orientation and spacing of the grid, as well as the spatial phase vary in a systematic fashion from cell to cell (Fyhn et al., 2008; Hafting et al., 2005). Different cells recorded at the same electrode, however, have the same grid spacing and orientation relative to the environment, but differ in their spatial phase. Therefore, local grid cell ensembles are thought to cover and spatially structure the whole environment by superimposing their individual grid patterns. Head direction cells were first discovered in the dorsal presubiculum (Taube et al., 1990), but have since been found in several other brain regions, namely the anterodorsal thalamus (Taube, 1995), lateral mammillary nuclei (Stackman

and Taube, 1998), retrosplenial cortex (Chen et al., 1994), lateral dorsal thalamus (Mizumori and Williams, 1993), striatum (Wiener, 1993), and entorhinal cortex (Sargolini et al., 2006). Their firing rate is modulated by the direction of the head relative to a fixed point in an environment. Boundary vector cells fire at the borders of an enclosed environment (e.g. walls) and are found in the subiculum (Lever et al., 2009), pre- and parasubiculum (Boccara et al., 2010), as well as the entorhinal cortex (Solstad et al., 2008). Grid-, head direction-, and boundary vector cells build the basis of the concept of path integration, i.e. integration of linear and angular self-motion. Obviously, spatial memory is an important aspect of episodic memory, which was first defined by Endel Tulving (Tulving and Donaldson, 1972) as a "neurocognitive system that enables human beings to remember past experiences" (Tulving, 2002) as episodes of "what" happened "where" and "when". We do not know, however, whether rodents or other animals are capable of conscious mental time travel as we experience it while remembering autobiographical episodes. However, a study by Fortin et al. (Fortin et al., 2002) demonstrated that hippocampal lesions produce a severe and selective impairment in the capacity of rats to remember the sequence of events. Additionally, neuronal activity in area CA1 of the hippocampus signals the timing of key events in sequences and differentiates distinct types of sequences (MacDonald et al., 2011). Furthermore, a study by Mankin et al. (2012) revealed a neuronal code for extended time in CA1. Therefore, it is reasonable to assume that the neuronal activity of a rodent exploring and navigating through space and time corresponds to the human capacity of episodic memory.

1.2. Functional anatomy of the rodent hippocampus

The hippocampus derives its name from its macroscopic appearance as a seahorse-like structure in the medial temporal lobe. Unfortunately, the term "hippocampus" and especially the adjective "hippocampal" is often used in an ambiguous manner. To be more precise, the macroscopically defined sea-horse like structure is composed of two closely connected regions, namely the dentate gyrus (DG) and the hippocampus proper. Using the nomenclature suggested by Amaral and Lavenex (2006), in the following text the term "hippocampus" will only refer to the latter structure, although the term "hippocampal" will be used depending on context to refer to either the hippocampus or the hippocampal formation. Because of its bent form, the hippocampus is also called cornu ammonis (CA) after the Egyptian god Amun Kneph, whose symbol was a ram. The hippocampus can be subdivided into three subfields, which are termed CA1, CA2, and CA3. The hippocampus and DG form the central part of the hippocampal formation, which further includes the subiculum, presubiculum, parasubiculum, and the entorhinal cortex. Together with the subiculum, the DG and hippocampus belong to the phylogenetically old allocortex. The cytoarchitectonically defining attribute of this cortex type is its three-layered structure, typically made up by a single principal cell layer with fiber-rich plexiform layers above and below the cell

layer. In contrast to the modularly organized, six-layered neocortex with mostly local wiring, the allocortex contains a large random connection space, which is a requisite for combining arbitrary information (Buzsáki, 2011). The existence of such a random connectivity space sets the allocortex functionally apart from the neocortex. Whereas the neocortical architecture is supposed to be more suitable to extract statistical regularities of the experienced world, the DG and hippocampus are more suitable to link information about objects, space, and time (Buzsáki, 2011), which is a fundamental requisite for episodic memory. A unique outstanding feature of the hippocampal formation is the largely unidirectional[1] information flow within the canonical "trisynaptic circuit", which is formed by excitatory connections from layer II of the entorhinal cortex to the DG (first synapse), from the DG to CA3 (second synapse), and from CA3 to CA1 (third synapse). However, the reader should keep in mind that this is a very simplified view containing only the main excitatory, i.e. glutamatergic, connections within the DG and hippocampus. Nevertheless, I will use this view to begin a more detailed description of the cytoarchitectonic organization of each hippocampal subfield. The first synapse of the trisynaptic circuit is located in the superficial plexiform layer of the DG, called the molecular layer. This layer is further subdivided based on three clearly separable regions of synaptic input. The outer third receives input from the lateral entorhinal cortex, the middle third from the medial entorhinal cortex, and the inner third from associational and commissural fibers originating in the ipsilateral and contralateral hilar region. The molecular layer mainly consists of the apical dendrites of the granule cells. These are the principal cells inside the relatively densely packed cell layer of the DG. They received their name after their elliptic form and the relatively small size of their somata (10–18 μm, Amaral and Lavenex, 2006; Claiborne et al., 1990). The granule cell layer and the molecular layer together are called the fascia dentata. This region is U- or V-shaped and encloses the so-called hilus, a region of loosely packed polymorphic cells, therefore also called the polymorphic layer. Besides the granule cells, there are two more known excitatory cell tpyes in the DG, namely the semilunar granule cells, and the hilar mossy cells. Semilunar granule cells are spiny, granule-like neurons located in the inner third of the molecular layer with a larger dendritic arborization in the molecular layer than granule cells. They have been shown to excite hilar interneurons and mossy cells, and—in contrast to granule cells—possess axon collaterals in the inner molecular layer (Williams et al., 2007). Hilar mossy cells have a large triangular or multipolar shaped cell body (25–35 μm in diameter), from which three or more thick dendrites originate to span large parts of the hilus (Amaral and Lavenex, 2006). Their axons project to the inner third of the molecular layer of the ipsilateral and contralateral hemisphere, and thereby appear to be the major source of the

[1] There are several exceptions to the rule of unidirectionality. For instance, proximal CA3 neurons in the ventral part of the hippocampus send collaterals into the hilus as well as the granule cell- and inner molecular layer of the DG (Scharfman, 2007). Furthermore, Jackson et al. (2014) recently demonstrated that theta rhythms generated in the rat subiculum *in vivo* could flow backwards relying on inhibitory GABAergic signaling to modulate spike timing and network rhythms in CA3.

excitatory associational/commissural projection to the DG (Amaral and Lavenex, 2006; Scharfman and Myers, 2012). The axons from granule cells are called mossy fibers. They innervate the polymorphic layer and project to CA3. On their way, they perforate the proximal CA3 pyramidal layer to form a narrow fiber zone superficial to the pyramidal cell layer, which is called stratum (str.) lucidum. The deep plexiform layer of CA3, which contains the basal dendrites of pyramidal cells (the principal cell type of the CA), is called str. oriens. The superficial plexiform layer comprises the str. radiatum, which contains the apical dendrites of pyramidal cells, and the str. lacunosum-moleculare, which contains the apical dendritic tuft and is delimited at the superficial site by the hippocampal fissure. Strata oriens and radiatum can also be defined as the regions where the ipsilateral as well as contralateral longitudinal associational and commissural fibers of CA3 pyramidal cells are located. These connections are the basis of an extensive autoassociative network, which is a functional hallmark of CA3. The cytoarchitectonic organization in CA1 is similar to that found in CA3. However, pyramidal cells in CA1 have a smaller soma size (ca. 15 μm in diameter) and are more densely packed than the ones in CA3, which have soma sizes between 20 and 30 μm in diameter depending on the proximo-distal position along the transverse axis of the hippocampus. In addition, a str. lucidum is absent in CA1, because of the lack of mossy fiber innervation. The fibers from CA3 pyramidal cells projecting to CA1 are called the Schaffer collaterals. They are located in str. radiatum and oriens of CA1 and innervate in a highly systematic fashion as much as two thirds of the septotemporal extent of the ipsilateral and contralateral CA1 field (Amaral and Lavenex, 2006). The border between CA1 and the subiculum is marked by the end of the Schaffer collateral projection. In sharp contrast to CA3, CA1 gives rise to only sparse associational and commissural projections. CA1 instead provides two projections inside the hippocampal formation: a topographically organized projection to the adjacent subiculum as well as to the entorhinal cortex, mainly terminating in its deep layers V and VI. Between the hippocampal regions CA3 and CA1, there is an additional subfield, namely CA2. CA2 pyramidal cells are morphologically similar to CA3 cells, and likewise project to CA1. In contrast to CA3, however, they lack thorny excrescences[1]. In addition, CA2 receives strong hypothalamic innervation from the supramammillary nucleus. The classic definition of CA2 includes the lack of mossy fiber innervation. However, recent studies redefined CA2 based on the expression of molecular markers, namely PCP4 (Lein et al., 2005), RGS14, STEP and MAP3K15 (Kohara et al., 2014). The main differences to the classically defined CA2 cells are a greater width along the transverse axis (ca. 300 μm compared to ca. 100 μm) and direct innervation by DG granule cells via abundant longitudinal mossy fiber projections (Kohara et al., 2014). This

[1] Mossy fibers possess large presynaptic terminals forming irregular interdigitated attachments with complex spines on hilar mossy cells as well as on proximal dendrites of CA3 pyramidal cells. These unique synaptic structures are called thorny excrescences and are the reason for the microscopic "mossy" appearance of the mossy fiber tract.

longitudinal projection fashion is different from the mainly transverse projection to CA3. In addition, the functional synaptic connections made by CA2 cells were found to be about 2.5-fold stronger with the deep rather than superficial CA1 cells (Kohara et al., 2014). This pathway, therefore, might act in parallel to the classical trisynaptic circuit.

The main cortical input to the DG and hippocampus arrives from layer II and III of the entorhinal cortex to the DG molecular layer and hippocampal str. lacunosum-moleculare. Fibers from layer II make synapses onto DG granule cells, and CA2/3 principal cells. In contrast, CA1 principal cells receive input from layer III of the entorhinal cortex. The inputs from layer II to CA2/3 and DG have a laminar organization: Fibers from the lateral entorhinal cortex terminate in the outer third of the DG molecular layer and the superficial part of str. lacunosum-moleculare in CA2/3. Likewise, fibers from the medial entorhinal cortex terminate in the middle third of the DG molecular layer and the deeper part of str. lacunosum-moleculare in CA2/3. In contrast, the inputs from entorhinal cortex layer III to CA1 are structured in a topographical fashion: Fibers from the lateral entorhinal cortex terminate in the distal zone along the transverse axis of the hippocampus, whereas fibers from the medial entorhinal cortex terminate in the proximal zone. In addition, laterally and caudally situated portions of the entorhinal cortex (both medial and lateral) project to septal levels of the DG and hippocampus, whereas progressively more medial and rostral portions project to more temporal levels of the DG and hippocampus (Amaral and Lavenex, 2006). Although the left and right hemispheres of the hippocampal formation do not appear to differ on a macroscopic level, more recent studies highlight clear differences on a subcellular and functional level. For instance, functional magnetic resonance imaging data obtained from humans revealed a left hippocampal dominance when semantic information was most task-relevant, but a right hippocampal dominance, when spatial information was more important to the task (Motley and Kirwan, 2012). Likewise, functional left-right asymmetry has been demonstrated in respect to long-term memory in mice (Shipton et al., 2014), which is in line with left-right synaptic differences (Kawakami et al., 2003; Shinohara et al., 2008).

1.3. Hippocampal interneurons

So far, I have only described the main excitatory connections within the DG and hippocampus. For a functional network, however, inhibition must be provided to prevent reverberatory excitation. Furthermore, inhibition is a requisite for high functional versatility, as it can provide autonomy to principal cell ensembles as well as meaningful temporal coordination. The task of inhibition is mainly delegated to highly heterogenous populations of locally connected interneurons, which use gamma-aminobutyric acid (GABA) as their main neurotransmitter. Interneurons are found in all layers of the DG and hippocampus and are usually classified based on a combination of morphological criteria and genetic marker expression. The most common morphological

criteria used for classification are the location of the soma, the orientation and laminar distribution of the dendrites, and, most importantly, the target area of their axonal plexus. Additionally, interneurons falling into different classes often differ in their electrophysiological properties. One of the most intensively studied interneuron types is the basket cell, whose soma generally lies along the deep surface of the DG granule cell layer, or inside or adjacent to the hippocampal pyramidal cell layer. Their dendrites branch into all layers, while the axon forms basket-like structures with multiple synapses at the principal cell somata and proximal dendrites (Freund and Buzsáki, 1996). There are two subtypes of basket cells which can be discriminated via the specific marker protein expression of either parvalbumin (PV) or cholecystokinin (CCK). CCK^+ cells are electrophysiologically characterized by a regular firing pattern and are well suited to modulate synchronous ensemble activities as a function of subcortical inputs. In contrast, the PV^+ basket cells have only a few receptor types for subcortical modulatory signals, but can efficiently be driven by local principal cells to fire at high rates (Freund and Katona, 2007). Like the basket cell, the so-called axo-axonic cell is characterized by a profound axonal innervation of the principal cell layer. The somata are also located within or immediately adjacent to the DG or hippocampal principal cell layers and give rise to axons which collateralize profusely inside the principal cell layer to exclusively terminate on the axon initial segments of the respective principal cells (Freund and Buzsáki, 1996). From a functional network perspective, perisomatic inhibition by basket and axo-axonic cells is ideally suited to control spiking activity, i.e. the output and thereby also the synchrony of principal cell ensembles. Other interneuron types possess an axonal plexus distributed in the associational/commissural pathway termination zone. One example in the DG is the HICAP-cell (hilar neuron with its axon distributed in the commissural/associational pathway termination zone), which has a dendritic distribution similar to the basket and axo-axonic cells. In the hippocampus proper, the bistratified cell gives rise to an axon, which specifically innervates str. radiatum and str. oriens, i.e. the input zones of the associational/commissural connections in CA3 or Schaffer collaterals in CA1. Its soma is located to the pyramidal cell layer with its dendrites spanning all layers except the str. lacunosum moleculare. Interneuron types with an axonal distribution inside the input zone of the perforant path fibers are the MOPP- (molecular layer perforant path-associated) and the HIPP- (hilar perforant path-associated) cells in the DG, and the O-LM- (oriens lacunosum-moleculare associated) cell in the CA region. The MOPP cell possesses a multipolar or triangular cell body with dendritic and axonal distributions in the outer two thirds of the molecular layer (Han et al., 1993). The HIPP cell is a fusiform cell, which resides in the hilar region with an axonal distribution within the outer two thirds of the molecular layer. O-LM cells have dense axonal plexus confined to str. lacunosum-moleculare, while their somata are scattered around all strata except str. lacunosum-moleculare in CA3, or confined to str. oriens in CA1. Functionally, distal dendrite-targeting cells like the dentate HIPP- and MOPP-, or the hippocampal O-LM cells are in a strategic position

to modulate dendritic inputs from the entorhinal cortex (but see Gidon and Segev, 2012). In addition to the interneuon types described so far, the IS- (interneuron-specific) cell is noteworthy, as it specifically innervates other interneurons (Freund and Buzsáki, 1996).

1.4. Hippocampal rhythms

One way to measure ongoing brain activity is via recordings of extracellular local field potential (LFP) signals. These typically show a rhythmic pattern at a variety of different frequency ranges. Importantly, these frequency ranges are not just randomly distributed over the frequency domain, but form a hierarchical system of overlapping bandwidths with peaks at multiples of natural log integer values following a scale free 1/f power law with $f = frequency$ (see Penttonen and Buzsáki, 2003, for a more detailed review on natural logarithmic relationship between brain oscillators). In humans and rodents, most of these frequency ranges have clear behavioral correlates and are therefore named for classification by greek letters, namely (for rodents) delta (1.5–4 Hz), theta (4–10 Hz)[1], beta (10–30 Hz), and gamma, which is further subdivided into slow gamma (30–80 Hz) and fast gamma (90–150 Hz) oscillations. Besides these frequency ranges there exist slow frequency oscillations with periods of tens of seconds, and high frequency events, e.g. hippocampal ripples (140–220 Hz). The interesting point of the 1/f characteristic of the LFP power spectrum is that this power spectrum resembles the most complex form of noise. This so-called pink[2] noise is the golden mean between disorder with high information content (would resemble a flat $1/f^0$ distribution, i.e. white noise) and the predictability of low information content (would resemble a $1/f^2$ distribution, i.e. brown noise, Buzsáki, 2011).

Theta oscillations, initially discovered by Jung and Kornmüller (Jung and Kornmüller, 1938), are a prominent rhythm in the hippocampal formation correlated in animals with behavioral states of arousal (Green and Arduini, 1954), active exploration and navigation (Vanderwolf, 1969), or rapid-eye-movement (REM) sleep (Jouvet, 1969). Electrolytic lesions to the medial septal nucleus in rats, which appeared to eliminate hippocampal theta rhythmic activity, resulted in spatial memory deficits (Winson, 1978), suggesting a functional role of hippocampal theta oscillations in information processing. Furthermore, successful memory encoding in animals is accompanied by increases in theta oscillatory power, as first shown in rabbits by Berry and Thompson (1978). Likewise, theta rhythmic oscillations in the medial temporal lobe of humans

[1] For humans, the clinical definition of theta is 4–8 Hz, and the frequency range of 8–12 Hz is referred to as alpha. The human theta and alpha frequency ranges, however, appear to be the same physiological entity in rodents. Thus, the human theta-alpha frequency band is combined in rodents to one theta range.

[2] Whereas the term brown noise is named after Robert Brown in honor of his discovery of Brownian movement of molecules and small particles, which follows a $1/f^2$ distribution, the terms white and pink noise are derived from the transference of the power spectrum to a color spectrum. The white color spectrum follows a $1/f^0$ distribution, and the pink color spectrum follows a 1/f distribution.

increase during virtual navigation (Ekstrom et al., 2005; Kahana et al., 1999) and working memory tasks (Raghavachari et al., 2001), and are important for encoding novel information (Lega et al., 2012). How does theta rhythmic activity contribute to memory encoding? First, it can act as a global synchronizing mechanism not only for facilitating information processing between each hippocampal region, but also across different brain regions. In line with this, a study by Sirota et al. (2008) showed that a significant fraction of neurons in neocortical areas as well as locally emerging gamma oscillations were phase-modulated by the hippocampal theta rhythm. Furthermore, LFP coherence between the medial prefrontal cortex and the hippocampus was increased in the theta range at the choice point of a Y-maze, where rats had to make a decision based on the memory of the previous trial (Benchenane et al., 2010). Outside the hippocampal formation, theta-phase coupling was shown to occur between area V4 of the visual cortex and the prefrontal cortex in humans, and the coupling strength was predictive for short-term memory performance (Liebe et al., 2012). Different frequency ranges of simultaneously ongoing oscillations allow to process and synchronize multiple layers of information via phase-coupling of the different rhythms. One example of such cross-frequency coupling is the coupling of hippocampal theta and gamma oscillations during exploratory activity and REM sleep, also known as theta-nested gamma oscillations (Belluscio et al., 2012; Bragin et al., 1995), which is hypothesized to be important for multi-item processing (Lisman and Jensen, 2013). Interestingly, gamma oscillations in the CA1 area of the rat hippocampus was separable into distinct fast (65–140 Hz) and slow (25–50 Hz) frequency components that were coherent with fast or slow gamma oscillations in the medial entorhinal cortex or CA3, respectively (Colgin et al., 2009). In concordance with this finding, Schomburg et al. (2014) showed that gamma oscillations in CA1 can be decomposed using an independent component analysis into a slow component most prominent in str. radiatum and a fast component most prominent in str. lacunosum moleculare, matching the input zones of CA3 and entorhinal cortex afferent fibers, respectively. Slow gamma oscillations predominantly occurred at the descending phase, whereas the fast gamma oscillations were coupled to the peak of theta measured at the CA1 pyramidal cell layer. In addition to gamma frequency, gamma power also varied as a function of the theta cycle in CA1 (Bragin et al., 1995), with the power of gamma (here defined as 40–100 Hz oscillations) reaching a maximum shortly after the peak of pyramidal layer theta. This phase of theta coincides with maximal interneuron activity in mice (Buzsáki et al., 2003). Such phase-amplitude theta-gamma coupling was shown to correlate with performance accuracy in a conditional discrimination task, where rats learned to associate contexts with the location of a subsequent food reward (Tort et al., 2009). Furthermore, theta-gamma coupling was larger during periods of working memory maintenance in humans. Additionally, when gamma power was concentrated during a narrower range of the theta phase, decisions in memory tasks arrived earlier (Axmacher et al., 2010). Second, theta rhythmic activity is thought to provide a temporal framework for the timing of spikes inside the hippocampal

formation, and across brain regions. A famous example inside the hippocampus is the phase coding mechanism used by place cells. These fire at progressively earlier phases at each successive cycle of the ongoing theta oscillation, when the animal traverses the cell's place field (O'Keefe and Recce, 1993; Skaggs et al., 1996), a phenomenon called phase precession. Likewise, spike-phase coupling and even spike-phase precession can occur between cortical and hippocampal circuits. This was shown in rats for neurons in the medial prefrontal cortex, which fired phase-locked to the hippocampal theta rhythm (Jones and Wilson, 2005a; Siapas et al., 2005). Based on this finding, Jones and Wilson (2005b) went on to show that correlated firing in the medial prefrontal cortex and CA1 of the rat hippocampus is selectively enhanced during retention of spatial working memory with concomitant enhanced LFP coherence at the theta range. Moreover, neurons in the medial prefrontal cortex increased phase-coupling to hippocampal theta oscillations in accordance with increased LFP theta coherence (Benchenane et al., 2010). Third, the temporal framework provides control over the modification of synaptic weights, i.e. synaptic plasticity (Hyman et al., 2003; Orr et al., 2001; Pavlides et al., 1988). Interestingly, the same high-frequency stimulus in CA1 of rat hippocampal slices can induce both long-term potentiation (LTP) or long-term depression (LTD) at Schaffer-collateral synapses, depending on the phase of the theta oscillation at which it is given (Huerta and Lisman, 1995). These physiological data inspired a model proposed by Hasselmo et al. (2002), in which different phases of the ongoing theta rhythm mediate separate phases of encoding and retrieval. The peak of theta measured at the principal cell layer of the hippocampus is the putative encoding phase, whereas the trough of theta is the putative retrieval phase. In line with this model, entorhinal cortex input to the hippocampus is highest during the peak of the pyramidal cell layer theta, as measured by intracellular recordings of CA1 pyramidal cells in urethane-anesthetized rats *in vivo* (Kamondi et al., 1998). At the same time perisomatic inhibition is greatest, which prevents spiking activity. These data from CA1 are consistent with a model of CA3 activity, which proposes that phasic perisomatic inhibition prevents activation of the CA3 autoassociative network during the peak of pyramidal cell layer theta (Kunec et al., 2005). Furthermore, during the encoding phase at the peak of theta measured at the principal layer, the intrinsically generated input from the associational and commissural network of CA3 is attenuated, whereas the extrinsic synaptic responses of inputs from the entorhinal cortex to the DG and hippocampus are left unaffected in rats exploring a novel environment (Villarreal et al., 2007). During the retrieval phase at the trough of pyramidal cell theta, however, the synaptic responses upon entorhinal cortex input are attenuated, whereas the synaptic inputs arriving from the autoassociative CA3 network are left unaffected. At the same time, CA1/3 receive least inhibition at this theta phase, thereby allowing most spiking activity. Taken together, direct entorhinal input conveying sensory information can depolarize pyramidal cell distal dendrites at the phase which is optimal for LTP, thereby facilitating the storage of new information content. Conversely, retrieval activity in CA3 coincides

with the phase, in which LTD is favored, preventing the misinterpretation of retrieved information as novel content (Hasselmo and Stern, 2013). Interestingly, this differential theta modulation of CA3 afferent inputs habituates with familiarity of the rat to the environment (Villarreal et al., 2007), and is blocked by systemic atropine application. I will come back to the special role of hippocampal acetylcholine for learning and memory processes later.

In the rodent hippocampus, the largest-amplitude theta oscillations are present at the level of the hippocampal fissure (Brankack et al., 1993; Buzsáki et al., 2003). In CA1, theta oscillations show a gradual phase shift from the pyramidal cell layer through the str. radiatum, reaching a full reversal (180 °) in str. lacunosum-moleculare (Buzsáki et al., 2003). This gradual phase shift with no zone of zero power of oscillatory activity indicates the presence of multiple, at least two, current generators. Current source density analyses have been used to identify the sources of the underlying theta generating currents (Brankack et al., 1993). This approach could be further refined in the future by applying independent component analysis to disentangle the different LFP sources (Makarov et al., 2010). One major theta current generator is in str. lacunosum-moleculare. Thus, synchronous and layered excitatory input from the entorhinal cortex in combination with rhythmic and phase-coupled distal inhibition is assumed to result in rhythmic changes of current sinks in this layer. A second current generator is found in str. radiatum, i.e. the input zone of CA3 collaterals (Kocsis et al., 1999). Finally, a third major current generator is inside or adjacent to the principal cell layer, i.e. at the target site of perisomatic inhibition (Brankack et al., 1993). Hippocampal theta activity is comprised of two components, which were initially separated pharmacologically, but also have clear behavioral correlates. One component of lower frequency theta oscillations (3–6 Hz) occurs in isolation during alert immobility as well as under urethane anesthesia (Kramis et al., 1975). This type of theta is fully abolished by intraperitoneal (i.p.) injection of the muscarinic acetylcholine (ACh) receptor antagonist atropine, and was therefore called atropine-sensitive theta (Kramis et al., 1975). The second component of theta is of faster frequency (8–12 Hz) and is prominent during movement. This type of theta is not blocked by applying muscarinic ACh receptor antagonists and was therefore called atropine-resistant theta. However, in contrast to the atropine-sensitive component, the atropine-resistant component is sensitive to anesthesia, such as ether or urethane anesthesia, as first demonstrated by Kramis et al. (1975). A full block of all theta activity can be achieved by a combination of muscarinic blocker and ether or urethane anesthesia (Kramis et al., 1975), indicating that two different rhythm generators are involved. Like for urethane, application of the N-methyl-D-aspartate (NMDA) receptor antagonist ketamine selectively blocks the fast atropine-resistant component of theta and results in a similar laminar LFP depth-profile (Soltesz and Deschenes, 1993). Therefore, and because *in vitro* experiments indicate a greater NMDA component of the entorhinal input versus the associational/commissural input to CA1 (Otmakhova et al., 2002), it was proposed that the glutamatergic afferents from the entorhinal cortex to the distal apical

dendrites play a major role for the atropine-resistant component of theta (Buzsáki, 2002). Indeed, isolation of the entorhinal cortex from its cortical inputs in combination with systemic atropine application completely abolished hippocampal theta oscillations (Buzsáki et al., 1983). Another way to eliminate both types of theta in urethane-anesthetized (Andersen et al., 1979), or awake animals (Donovick, 1968; Green and Arduini, 1954; Green and Rawlins, 1979) is by lesioning the medial septum/vertical limb of the diagonal band of Broca (MSvDB) complex, or by cutting its fiber projections to the hippocampus, which mainly run through the fimbria-fornix. Likewise, global pharmacological inhibition of MSvDB activity in freely moving animals eliminates theta oscillations (Chrobak et al., 1989; Givens and Olton, 1994; Lawson and Bland, 1993). These experiments indicate a major role of the MSvDB for hippocampal theta generation. The presence of rhythmically bursting cells in the MSvDB, initially discovered in rabbits (Petsche et al., 1962), gave rise to the hypothesis that the MSvDB serves as a "pacemaker" for hippocampal theta rhythms.

1.5. The medial septum and the vertical limb of the diagonal band of Broca

1.5.1. The cholinergic system

In rodents, the medial septum (MS) and the vertical limb of the diagonal band of Broca (vDB) are located in the dorsal rostral and intermediate basal forebrain, which contains several nuclei with widespread cholinergic projections to the allocortex and isocortex (Woolf, 1991). The MS lies along the midline of the septum, whereas the vDB appears as a boomerang-shaped structure along the ventro-lateral border of the MS. The first unambiguous experiments to study the cholinergic organization of the basal forebrain system were done with retrograde tracing experiments using local injections of horseradish peroxidase conjugated covalently to wheat germ agglutinin in combination with choline acetyltransferase (ChAT) immunohistochemistry in rats. These experiments revealed a clear topographical organization of the projection fibers from the individual cholinergic nuclei of the basal forebrain (Mesulam et al., 1983; Rye et al., 1984). Rye et al. (1984) studied this topographical organization in rats and quantified the proportion of $ChAT^+$ cells within the population of retrogradely stained projection neurons. Briefly, the horizontal diagonal band of Broca nucleus, which lies more ventrally and rostrally inside the basal forebrain, projects heavily to the olfactory bulb, but only 10–20 % of these projecting cells are $ChAT^+$. The substantia innominata and the nucleus basalis of Meynert, which lie in the caudal and ventral part of the basal forebrain, project mainly to the amygdala and the cortical mantle. 80–90 % of these cells were demonstrated to be $ChAT^+$. In line with other studies (Mesulam et al., 1983; Woolf, 1991; Woolf et al., 1984), the MS and the vDB were shown to project to the hippocampal

formation and provide most of its cholinergic input. Both nuclei also send fibers to hypothalamic areas and the mammillary complex, and the MS additionally projects to the ventral tegmental area, raphe nuclei, and thalamus (Swanson and Cowan, 1979). Within the MS and vDB approximately 30–50 % and 50–75 % of all cells are ChAT$^+$, respectively (Mesulam et al., 1983). Within the population of only the retrogradely traced septo-hippocampal projection neurons 30–35 % of cells inside the MS and 45–55 % of cells inside the vDB appeared to be ChAT$^+$ (Wainer et al., 1985). However, this proportion of ChAT$^+$ retrogradely labeled cells ranged from 23 % to 77 % in different experiments depending on the exact retrograde tracer injection site and the exact spot studied inside the MSvDB due to a topographic organization of the septo-hippocampal projection (Amaral and Kurz, 1985). In general, a lower percentage of ChAT$^+$ cells project to the septal levels of the hippocampus than to more temporal levels (Amaral and Kurz, 1985). In addition, septal levels of the hippocampus receive the major portion of their cholinergic input from the vDB, whereas the MS projects more heavily to temporal levels (Amaral and Kurz, 1985). Furthermore, there is a mediolateral topographical organization: Cells located medially inside the MSvDB preferentially project to the septal pole of the hippocampus, whereas more lateral aspects of the MSvDB project to progressively more caudal or temporal levels (Amaral and Kurz, 1985; Wainer et al., 1985). Fibers from the basal forebrain travel via four routes to the hippocampus, namely the fimbria, the dorsal fornix, the supracallosal striae, and a ventral route passing through the amygdala, as initially shown for the cholinergic fibers (Amaral and Kurz, 1985). This projection is mainly ipsilateral, but some contralateral projections are observed as well (Kiss et al., 1990a,b). Inside the hippocampus, cholinergic fibers are found in all subfields with a more dense concentration around the proximal dendrites of CA pyramidal cells, as well as in str. lacunosum-moleculare of the hippocampus, and the molecular layer of the DG (see Figure 1.1).

In addition to the extensive septo-hippocampal cholinergic input, ChAT$^+$ non-GABAergic cell bodies exist in the DG and hippocampus. However, they are very sparsely distributed (Frotscher et al., 1986, 2000; Wainer et al., 1985). Nevertheless, Cobb and Davies (2005) have demonstrated in hippocampal slices from fimbria-fornix lesioned animals that endogenous activation of nAChRs tailors the pattern of CA3 network activity into theta-frequency depolarizing episodes, suggesting a possible role of these cells in synchronization of hippocampal oscillatory states.

1.5.2. Hippocampal acetylcholine and memory

In vivo microdialysis experiments in rats demonstrated that hippocampal ACh levels increased during active exploration (Marrosu et al., 1995), further increased during exploration of novel in comparison to familiar space (Aloisi et al., 1997; Bianchi et al., 2003; Giovannini et al., 2001), and during learning of a spatial memory task (Stancampiano et al., 1999). Using a combination

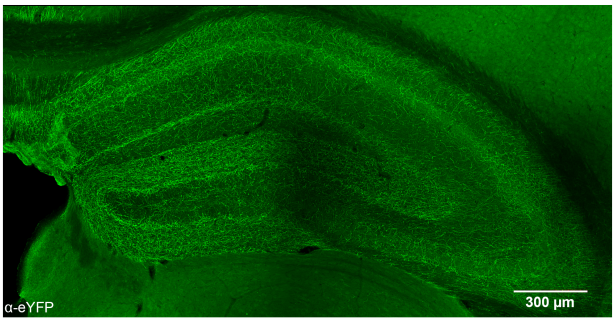

Figure 1.1 – Hippocampal distribution of septo-hippocampal cholinergic fibers. ChR2-eYFP$^+$ cholinergic septo-hippocampal fibers preferentially terminate in str. oriens and pyramidale around the proximal dendrites of CA pyramidal cells, in str. lacunosum-moleculare of the hippocampus (covering the whole layer in CA3 and a narrower band within str. lacunosum-moleculare of the CA1 subfield), and the molecular layer of the DG. Fluorescence of ChR2-eYFP transgene expression was enhanced by immunohistochemical staining against eYFP (see Materials and Methods). Image is a maximum intensity projection of confocal images taken from a 50 μm coronal slice of a ChAT-Cre mouse locally injected into the MSvDB with a Cre-dependent rAAV coding for ChR2-eYFP (see Materials and Methods). Scale bar is 300 μm. Courtesy of Jurij Rosen.

of LFP recordings and a novel amperometric approach (Burmeister et al., 2008) for detection of synaptically released ACh levels at a second-by-second time resolution in urethane-anesthetized rats *in vivo*, Zhang et al. (2010) found that ACh release was highly correlated with the appearance of both spontaneous and induced theta oscillations.

In the central nervous system (CNS), ACh mainly acts as a neuromodulator, i.e. its main effects on network activity do usually not derive from direct excitatory or inhibitory actions as it is the case for glutamate or GABA, respectively, but via modulation of neuronal excitability, presynaptic release probability, postsynaptic responsiveness, or synaptic plasticity. In sharp contrast to GABAergic synaptic varicosities, only 7 % of ChAT$^+$ axon terminals in CA1 of the rat hippocampus exhibit synaptic junctional specializations, indicating that volume transmission is the preferential mode of cholinergic modulation (Umbriaco et al., 1995; Yamasaki et al., 2010). ACh can act on two different types of receptors, namely the nicotinic and muscarinic type (nAChR and mAChR, respectively), which can be found pre- and postsynaptically on both interneurons and principal cells (Levey et al., 1995; Picciotto et al., 2012) as well as astrocytes (Sharma and Vijayaraghavan, 2001; Van Der Zee et al., 1993). The nicotinic type is a ionotropic receptor built as a homo- or heteromeric pentamer, which can be activated pharmacologically by the drug nicotine and functions as a non-selective, excitatory cation channel (Changeux et al., 1998; Picciotto et al., 2012). On a behavioral level, local infusion of nicotinic antagonists into the hippocampus was demonstrated to impair working memory in rats (Ohno et al., 1993). The predominant nAChR type in the hippocampus is the $(\alpha 7)_5$ homomer (Radcliffe et al., 1999; Seguela

et al., 1993), followed in expression levels by the heteromeric $(\alpha4)_2(\beta2)_3$ and $(\alpha3)_2(\beta4)_3$ channel compositions (Radcliffe et al., 1999; Zoli et al., 1998). Principal neurons and interneurons are differentially affected by nAChRs. In region CA1 of rat hippocampal slices, most pyramidal cells show only small changes of membrane potential or membrane currents in response to nicotinic agonists (McQuiston and Madison, 1999b). However, functional calcium imaging with Fura-2-acetoxymethyl ester revealed functional $\alpha7$ nAChRs in CA3 principal as well as DG granule cells (Grybko et al., 2010). Likewise, in region CA1 of rat hippocampal slices *in vitro*, the stimulation with choline, which is a selective $\alpha7$ nAChR agonist, in combination with an allosteric modulator of $\alpha7$ nAChRs evoked small but reliable membrane depolarizations of ca. 4 mV (Kalappa et al., 2010). Taken together, these experiments provide evidence for functional somato-dendritic $\alpha7$ nAChRs on DG granule as well as CA pyramidal cells. Furthermore, there is a strong functional expression of $\alpha7$ nAChRs on glutamatergic presynaptic terminals inside region CA3 (Gray et al., 1996), which can enhance the release of glutamate via protein kinase A activation (Cheng and Yakel, 2014). Activation of these receptors induced high-frequency bursts of miniature excitatory postsynaptic currents (mEPSCs) in CA3 pyramidal cells in rat hippocampal slices (Gray et al., 1996; Sharma and Vijayaraghavan, 2003). Such mEPSCs were sufficient to drive postsynaptic spiking in the absence of incoming action potentials, which were inhibited by tetrodotoxin application (Sharma and Vijayaraghavan, 2003). Consistent with these observations, nicotine has been demonstrated *in vitro* to increase intracellular Ca^{2+} in mossy fiber presynaptic terminals and to enhance the frequency of mEPSCs, but also miniature inhibitory postsynaptic currents (mIPSCs) recorded from CA3 neurons in rat hippocampal slices (Radcliffe et al., 1999). Likewise, nicotine application caused a short initial reduction followed by a longer period of enhancement of stimulation-induced field excitatory postsynaptic potential (EPSP) amplitudes (Giocomo and Hasselmo, 2005). This effect was selective for str. lacunosum-moleculare, and absent in str. radiatum of CA3. Taken together, these *in vitro* results indicate a selective nicotinic receptor-mediated enhancement of afferent inputs to hippocampal CA3, whereas recurrent excitation appears to remain unaffected.

In contrast to principal cells, interneurons can have very large nAChR currents, which were shown to have fast kinetics and to be mainly mediated by the $\alpha7$ subtype, both in the hippocampus (Frazier et al., 1998; Jones and Yakel, 1997) and the DG (Frazier et al., 2003). However, these experiments were done with ACh applied directly onto the cell bodies in hippocampal slices. In contrast, a more recent study from Bell et al. (2011) using synaptically released acetylcholine in mouse brain slices were not able to reproduce these results. Instead, they found that synaptically released acetylcholine upon optogenetic stimulation resulted in mostly subthreshold depolarizations with slow kinetics mediated by the activation of $\alpha4\beta2$ nicotinic receptors in CA1 interneurons with their somata and dendrites located in str. oriens or str. lacunosum-moleculare.

Interestingly, the slow kinetics of the $\alpha4\beta2$ nAChR subtype-mediated depolarizations have previously been shown in rat hippocampal slices (Alkondon et al., 1999) and are consistent with volume transmission. Nevertheless, a single interneuron type can be modulated by all three nAChR subtypes (Alkondon and Albuquerque, 2004). On the network level, strong nAChR-mediated excitation of interneurons in CA1 led to inhibition or disinhibition of principal cells *in vitro* (Ji and Dani, 2000). In line with this, activation of preterminal axonal nAChRs of the $\alpha4\beta2$ type caused GABA release from interneurons to other interneurons or principal cells (Albuquerque et al., 2009). In contrast, axonal nAChRs of the $\alpha3\beta4$ type enhanced both glutamatergic (Albuquerque et al., 2009) and GABAergic transmission (Tang et al., 2011) to other interneurons. In addition, nAChRs can also regulate a number of other neurotransmitter systems in the hippocampus. For instance, $\alpha3$ and $\beta2$ subunit containing nAChRs with unclear pre- or postsynaptic localization have been demonstrated to be involved in release of noradrenaline (Sershen et al., 1997).

In contrast to the ionotropic nature of the nicotinic AChR type, the muscarinic AChR, which is activated by the drug muscarine, is metabotropic, i.e. it acts via functional coupling and activation of heteromeric G proteins. Five subtypes of muscarinic ACh receptors have been identified and termed M1–5. The receptor types M1, M3, and M5 are coupled to G_q proteins which activate phospholipase C, which eventually leads to Ca^{2+} influx and activation of intracellular signaling cascades. In contrast, the type M2 and M4 receptors are coupled to $G_{i/o}$ proteins, that inhibit the adenylyl cyclase and thereby reduce the production of cAMP (Wess, 2003). A quantification of relative proportions of the M1–M5 mAChR subtypes with immunoprecipitation followed by a radioligand binding assay in post-mortem tissue of the human hippocampus yielded ca. 60 % M1, 20 % M2, 15 % M4, and a minor contribution of ca. 5 % M3 receptor expression (Flynn et al., 1995). Similarly, the same method applied to rat hippocampal tissue revealed a proportion of ca. 36 % M1, 33 % M2, and 27 % M4 receptor expression with M3 not tested (Levey et al., 1995). Although M5 mRNA can be detected by in-situ hybridization histochemistry in CA1 pyramidal cells of the rat hippocampus (Vilaró et al., 1990), the protein expression is very low (Wall et al., 1992) with unknown functional significance. Hence, M1, M2, and M4 are the most prevalent receptor subtypes in the hippocampus. M1 is widely distributed within the hippocampus and preferentially expressed in somata and dendrites of hippocampal pyramidal and DG granule cells (Levey et al., 1995; Yamasaki et al., 2010), with only a small fraction expressed on axons and terminals. From a functional perspective, M1 receptors are mainly responsible for the modulation of pyramidal cell excitability upon transient/phasic ACh application in slices (Gulledge and Kawaguchi, 2007). Interestingly, CA1 and CA3 principal cells respond differently to such phasic local ACh puff applications: ACh application near the somata of CA1 principal cells resulted in a hyperpolarization of the membrane potential ca. 2.5 mV via calcium dependent activation of small conductance calcium activated potassium (SK) channels, but ACh applied to CA3 principal cells generated a small depolarization of ca. 0.6 mV. In contrast to phasic application, tonic

cholinergic modulation of CA1 principal cells via application of the stable cholinergic agonist carbachol decreased medium afterhyperpolarizations (AHPs) and the early component of the slow AHPs, generated afterdepolarizations (ADPs) via M1 mAChRs, and depolarized CA1 principal neurons via M1 and M3 mAChRs (Dasari and Gulledge, 2011). In CA3, however, tonic carbachol application did not significantly modulate the resting membrane potential, but induced "shoulder potentials" following depolarizing current steps via M1 and M3 mAChRs. Besides M1, M4 is the other major mAChR subtype responsible for direct cholinergic modulation of the excitatory hippocampal circuit. In contrast to the preferential somato-dendritic localization of M1, M4 is mainly located in glutamatergic terminals and mediates cholinergic suppression of Schaffer collateral EPSPs *in vitro* (Dasari and Gulledge, 2011; Shirey et al., 2008). The expression of the M2 subtype is restricted to interneurons, thus not present on principal cells (Levey et al., 1995).

In contrast to the mainly slow depolarizing synaptic response mediated by mAChR activation in principal cells, hippocampal interneurons respond with a much greater diversity regarding the waveform of synaptic potentials, as shown for CA1 interneurons in rat hippocampal slices with electrical (McQuiston and Madison, 1999a; Widmer et al., 2006) or optogenetic stimulation of synaptic acetylcholine release (Bell et al., 2013). Importantly, interneurons that responded to optogenetically released acetylcholine predominantly had muscarinic- (80 %) vs. nicotinic- (17 %) mediated changes in membrane potential, and only 3 % of interneurons had mixed responses (Bell et al., 2013). In the studies from Widmer et al. (2006) and Bell et al. (2013) the majority of interneurons (64 % and 40 %, respectively) responded with an atropine-sensitive slow depolarization upon synaptic ACh release, 13 % and 25 %, respectively, responded with a biphasic first hyper-, then depolarizing response, and 20 % and 35 %, respectively, showed a pure hyperpolarizing response. A minor fraction of cells in the study from Widmer et al. (2006) responded with membrane potential oscillations (2 %) without any obvious correlation to a morphological classification of the different interneurons. In the study from Bell et al. (2013), the hyperpolarizing response was demonstrated to be mediated via activation of an inwardly rectifying potassium channel by activation of the M4 mAChR subtype, whereas the depolarizations were likely produced by M3 receptor activation. Considering the correlation of acetylcholine levels with different functional network states, it is noteworthy that hyperpolarizing responses required less optogenetic stimulation strength, i.e. less synaptic acetylcholine release, than depolarizing responses. This favors a model proposed by McQuiston (2014), in which low levels of acetylcholine favor disinhibition, whereas higher levels of acetylcholine favor inhibition of hippocampal principal cells. If interneurons are depolarized by M1/M3 mAChR activation, this can lead to consistently enhanced firing frequency and the production of ADPs , as shown for O-LM interneurons (Lawrence et al., 2006b) as well as basket cells (Cea-del Rio et al., 2010) in CA1. Concomitantly, mAChR activation enhances firing reliability and precision to theta frequency input in O-LM (Lawrence et al., 2006a) as well as CCK^+ Schaffer collateral associated and basket cells (Cea-del Rio et al.,

2011). Interestingly, PV^+ basket cells express M1 mAChR mRNA, but entirely lack M3 mRNA, whereas CCK^+ basket cells show robust expression of both M1 and M3 mRNA. The additional expression of M3 makes the CCK^+ basket cells more sensitive than PV^+ basket cells for increases in firing rates upon cholinergic input, as shown in CA1 of mouse hippocampal slices (Cea-del Rio et al., 2010). Dendritically projecting Schaffer collateral-associated CCK^+ cells, which shape dendritic excitability and synaptic integration, showed similar changes in excitability, except that they showed a biphasic change corresponding to an initial M1-mediated hyperpolarization, followed by an M3-mediated depolarization of their membrane potential (Cea-del Rio et al., 2011). In line with the activation of perisomatic inhibitory interneurons, optogenetically released acetylcholine resulted in an increase of IPSCs onto CA1 pyramidal neurons (Bell et al., 2014; Nagode et al., 2011). Interestingly, the theta-rhythmic IPSCs could be blocked by endocannabinoid release from pyramidal cells, providing further support that the main source of IPSCs are type 1 cannabinoid receptor expressing CCK^+ basket cells (Nagode et al., 2011, 2014). Despite the effect of increasing IPSC frequency in pyramidal neurons, activation by carbachol significantly decreased the amplitude of IPSCs mediated by perisomatic inhibitory interneurons via a direct postsynaptic and an indirect presynaptic suppression of transmitter release in area CA3: Presynaptic M2-type mAChRs were responsible for the reduction in IPSC amplitude in axo-axonic- and PV^+ basket cell-pyramidal cell pairs, whereas postsynaptic M1/M3 receptors in pyramidal cells triggered the synthesis of endoannabinoids, which activated type 1 cannabinoid receptors at the terminals of CCK^+ basket cells, resulting in reduced GABA release (Szabó et al., 2010). Besides their abundant presynaptic location, M2 mACRs are also expressed postsynaptically in dendrites and somata of hippocampal interneurons located inside or close to str. oriens as well as hilar interneurons (Hájos et al., 1998; Rouse et al., 1998). Furthermore, M2 mAChRs are located not only on non-cholinergic, but also cholinergic terminals (Rouse et al., 2000), where they can function as presynaptic autoreceptors, the activation of which inhibits ACh release, as shown in synaptosomes from rat hippocampus (Raiteri et al., 1984). In summary, the subtype-specific cholinergic modulation of interneuron activity can have severe impacts on network dynamics supporting learning and memory. Evidence for this was given recently by an *in vivo* study from Lovett-Barron et al. (2014), in which aversive stimuli were shown to activate CA1 O-LM interneurons via cholinergic input, leading to inhibition of the distal dendrites of CA1 principal cells, which was necessary for successful fear learning.

1.5.3. Effects of acetylcholine on synaptic plasticity

Because ACh affects memory and learning, the question arises, how ACh modulates synaptic plasticity, which is generally assumed to be the cellular and molecular correlate of learning. Two very prominent forms of synaptic plasticity are LTP, and LTD of postsynaptic responses upon

presynaptic activation. Importantly, the direction of the induced synaptic plasticity depends on the precise timing in relation to the ongoing theta oscillation: A single burst given *in vitro* at the peak of theta measured in str. radiatum near to the pyramidal cell layer induced homosynaptic LTP, whereas the same stimulus given at the theta trough induced homosynaptic LTD (Huerta and Lisman, 1995). These results were later confirmed with a similar burst stimulation in awake behaving rats (Hyman et al., 2003). In addition, single burst stimulation-induced LTP at basal dendrites of CA1 was significantly larger, when it was induced during walking than during awake immobility, slow wave sleep, or REM sleep of rats (Leung et al., 2003). On the receptor level, pre- and postsynaptic nAChR and mAChR activity on principal cells and interneurons are involved in the modulation of synaptic plasticity in a complex manner. For instance, nAChR activity could enhance or depress synaptic plasticity with the form of the modulation depending on the location and timing of the nAChR activity relative to the electrical stimulation used for LTP induction in mouse hippocampal slices (Ji et al., 2001): Local puff application of ACh to the apical dendrites was sufficient to boost short term plasticity of Schaffer collateral synapses to LTP. When the same stimulus was delayed until nAChR-mediated GABAergic inhibition reached the pyramidal neuron, however, LTP was prevented. In addition to nAChR activity, mAChR activation was shown to modulate the induction and amplitude of LTP at hippocampal Schaffer collateral synapses in slice preparations from rats (Buchanan et al., 2010; Huerta and Lisman, 1995) or mice (Shinoe et al., 2005). Similar results were obtained, when cholinergic activity was evoked by tail pinch or electrical stimulation of the medial septum nuclei in anesthetized rats *in vivo* (Navarrete et al., 2012). Induction of LTP was blocked in this study by systemic atropine application, confirming the contribution of mAChRs. Mechanistically, Buchanan et al. (2010) showed that postsynaptic activation of the muscarinic M1 receptor subtype resulted in the inhibition of SK channels, allowing enhanced NMDA receptor activity and eventually leading to a facilitation of LTP induction.

1.5.4. Acetylcholine effects on astrocytes

Besides its effects on neurons, ACh also acts on astrocytes. Calcium imaging from acute rat hippocampal slices demonstrated the presence of functional α7-containing nAChRs on astrocytes in the CA1 (Shen and Yakel, 2012) and CA3 region (Grybko et al., 2010). Although the current density is very low, the calcium response upon receptor activation is robust due to the calcium induced calcium release from the endoplasmic reticulum mediated via inositol trisphosphate (IP3) receptor activation (Grybko et al., 2010; Sharma and Vijayaraghavan, 2001). In contrast to these studies, synaptically released ACh in CA1 of rat hippocampal slices did not reveal significant nicotinic receptor-mediated effects, but instead mobilized Ca^{2+} from intracellular stores via muscarinic receptor activation (Araque et al., 2002). In this study, different regions in the recorded

astrocytes showed independent stimulus-induced Ca^{2+} variations, suggesting the existence of subcellular domains in the astrocytic responses evoked by the synaptic cholinergic activity. One caveat of this study, however, is that the potassium channel blocker 4-aminopyridine (4-AP) was added to the slice in order to enhance synaptic release of acetylcholine. *In vivo* astrocytes in the barrel cortex of mice exhibited elevated intracellular calcium levels during the induction of LTP, as revealed by calcium imaging (Takata et al., 2011). Moreover, the induction of LTP could not be induced in IP3 receptor type 2 knockout mice, indicating that calcium release from intracellular stores in astrocytes might be necessary for LTP induction. Likewise, ACh release evoked *in vivo* by tail pinch or electrical stimulation of the medial septum nuclei in anesthetized rats increased Ca^{2+} in hippocampal astrocytes and induced LTP at Schaffer collateral synapses, which required mAChR activation (Navarrete et al., 2012). Further follow-up experiments performed *in vitro* confirmed the necessity of Ca^{2+} elevations in astrocytes for LTP induction at the Schaffer collateral synapse in the hippocampus, as previously shown for synapses in the barrel cortex. Given the various functions of astrocytes for neuronal and network functions (reviewed in Volterra and Meldolesi, 2005), including contributions to gamma oscillations and novel object recognition (Lee et al., 2014), the functional impact of cholinergic modulation of astrocytes on hippocampal network function has not been fully appreciated so far.

1.5.5. Acetylcholine effects on memory

In humans, pharmacological disruption of cholinergic function by systemic administration of the muscarinic receptor antagonist scopolamine impaired new word paired-associate learning (Atri et al., 2004). Furthermore, systemic administration of scopolamine to humans impaired both object and spatial *n*-back working memory (Green et al., 2005). In the same study, simultaneous application of scopolamine and the nicotinic receptor antagonist mecamylamine produced even greater impairments, suggesting synergistic actions of muscarinic and nicotinic receptor activation for this kind of working memory. Likewise, pharmacological blockade of either hippocampal nicotinic receptors or M1 muscarinic receptors by local drug injections in rats impairs working memory (Ohno et al., 1993, 1994). One possible mechanism contributing to the maintenance of information during working memory tasks as well as during the encoding of novel information is the cell-intrinsic capacity of persistent spiking activity, which has been demonstrated *in vitro* in neurons of the entorhinal cortex (Egorov et al., 2002; Klink and Alonso, 1997; Yoshida et al., 2008) and dorsal presubiculum (Yoshida and Hasselmo, 2009) in rats. *In vitro* these neurons can fire up to minutes after an initial depolarizing current injection, if the cholinergic agonist carbachol (Egorov et al., 2002; Klink and Alonso, 1997) or an agonist of the metabotropic glutamate receptor has previously been applied (Yoshida et al., 2008). Persistent spiking has also been demonstrated to be present *in vivo*: Suzuki et al. (1997) observed sample-specific delay activity

in the entorhinal cortex during the delay intervals of a place memory task in macaques, and Young et al. (1997) observed for the parahippocampal region that "a substantial proportion of cells showed odor-selective activity throughout or at the end of the memory delay period" of an odor-guided delayed nonmatching-to-sample task in rats. Furthermore, head-direction cells recorded from the dorsal presubiculum *in vivo* show a very similar persistence of spiking, as these neurons continue to spike, when the animal's head remains in the preferred direction of the cell (Taube and Muller, 1998). Similar to the effects on working memory, direct injection of the muscarinic receptor blocker scopolamine into the dorsal hippocampus impaired encoding of spatial information in the Morris water maze-task (Blokland et al., 1992). Importantly, local injections of scopolamine into the hippocampal CA3 or CA1 subfields in rats performing the modified Hebb-Williams maze-task selectively disrupted encoding of spatial information, while sparing retrieval (Rogers and Kesner, 2003). Conversely, enhancing ACh levels in CA3 or CA1 by local injections of the acetylcholinesterase inhibitor physostigmine selectively disrupted retrieval, but spared encoding. Taken together with the positive effects of hippocampal acetylcholine on synaptic plasticity and theta oscillations, these data favor a model, in which high levels of acetylcholine promote an encoding state of the entorhinal-hippocampal network.

1.5.6. The GABAergic neurons of the MSvDB

Retrograde fluorescent tracing combined with glutamic acid decarboxylase (GAD)-immunohistochemistry revealed the presence of approximately 30 % GABAegic cells in the MSvDB that project to the hippocampus (Amaral and Kurz, 1985; Köhler et al., 1984). Inside the MS, the GABAergic cells mainly harbor the medial portion along the midline, which is relatively spared by the cholinergic cells. These data are in line with retrograde tracer experiments from Kiss et al. (1990a,b) showing that 33 % of the neurons, which were retrogradely labeled after hippocampal tracer injection, were immunoreactive for PV, which has been established as a marker protein for medial septal GABAergic neurons (Freund, 1989). Whereas the cholinergic projection terminates both on principal cells and interneurons (Frotscher and Léránth, 1985), the septal GABAergic neurons selectively innervate hippocampal interneurons (Freund and Antal, 1988). Fibers from PV^+ MSvDB neurons are evenly distributed around the DG hilus, as well as CA str. oriens, pyramidale, and radiatum. Interestingly, fibers neither innervate the molecular layer of the DG, nor the str. moleculare of the hippocampus proper (see Figure 1.2).

1.5.7. The glutamatergic neurons of the MSvDB

Beside the cholinergic and GABAergic neurons within the MSvDB, the identity of the remaining cell populations have remained elusive, until the discovery of a substantial portion of MSvDB neurons expressing transcripts for either solely or both of the vesicular glutamate transporters

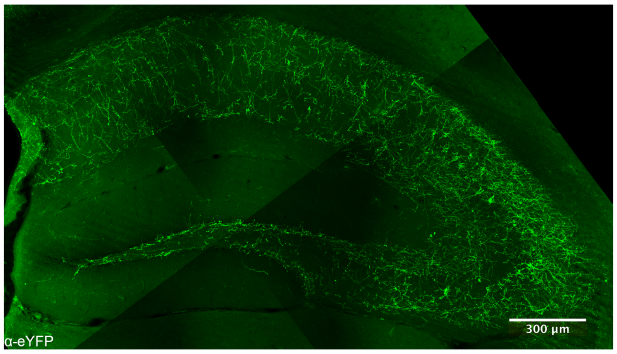

Figure 1.2 – Hippocampal distribution of septo-hippocampal PV$^+$ GABAergic fibers. ChR2-eYFP$^+$ septo-hippocampal PV$^+$ GABAergic fibers terminate in str. oriens, pyramidale, and radiatum of the CA fields, and in the hilus of the DG. Fibers are virtually absent within hippocampal str. lacunosum-moleculare and the the molecular layer of the DG. Fluorescence of ChR2-eYFP transgene expression was enhanced by immunohistochemical staining against eYFP (see Materials and Methods). Image is a maximum intensity projection of confocal images taken from a 50 μm coronal slice of a PV-Cre mouse locally injected into the MSvDB with a Cre-dependent rAAV coding for ChR2-eYFP (see Materials and Methods). Scale bar is 300 μm. Courtesy of Jurij Rosen.

VGLUT1 or VGLUT2, but no transcripts for GAD or ChAT, which identifies these cells as putative glutamatergic (Sotty et al., 2003). Retrograde tracing via fluorogold injections into the hippocampus or DG in combination with immunohistochemistry of septal slices with anti-glutamate antiserum showed that approximately 23 % of the septo-hippocampal fibers are indeed glutamatergic projections (Colom et al., 2005). In addition to the glutamatergic MSvDB neurons contributing to septo-hippocampal projections, glutamate might be released as a cotransmitter from other septo-hippocampal projection neurons. Indirect support for this hypothesis comes from the study of Colom et al. (2005), in which only 46 % of the glutamatergic septo-hippocampal projection neurons solely immuno-reacted with an antiglutamate antibody, but 20 % were dual positive for glutamate and ChAT, 16 % were dual positive for glutamate and PV, and 8 % were triple positive to glutamate, ChAT, and PV. Using electrical stimulation of the fornix as well as direct activation of MSvDB neurons via NMDA microinfusion in an *in vitro* septo-hippocampal preparation revealed that VGLUT2$^+$ MSvDB neurons provide excitatory synaptic input to CA3 pyramidal cells (Huh et al., 2010). Furthermore, multisynaptic IPSPs were frequently observed, indicating that the glutamatergic MSvDB neurons might also excite hippocampal interneurons.

1.5.8. Electrophysiological properties of MSvDB neurons

Cholinergic MSvDB neurons are characterized *in vitro* by a slow, regular firing pattern, a broad action potential width, and a prolonged slow AHP (Griffith and Matthews, 1986; Markram and

Segal, 1990). In contrast, most GABAergic MSvDB neurons *in vitro* display fast- or burst-firing properties and a large hyperpolarization-activated inward current (I_h[1]) with action potentials of significantly shorter duration than the ones from regular-spiking putative cholinergic neurons (Morris et al., 1999; Sotty et al., 2003). The GABAergic MSvDB neurons have long been suggested to pace hippocampal rhythmic activity at the theta range via disinhibition of hippocampal principal cells. This idea is tempting, because—as previously mentioned—septo-hippocampal projections of PV^+ MSvDB neurons terminate selectively on hippocampal interneurons, mainly on perisomatic inhibitory basket cells (Freund and Antal, 1988; Serafin et al., 1996; Tóth et al., 1997), and PV^+ neurons in the MSDB indeed lead the hippocampal network during theta oscillations (Hangya et al., 2009; Huh et al., 2010; Varga et al., 2008). Furthermore, GABAergic MSvDB neurons *in vivo* form two populations of rhythmically bursting cells, which fire bursts phase locked either to the trough or the peak of the ongoing hippocampal theta oscillations (Borhegyi et al., 2004).

Initially, the putative glutamatergic MSvDB neurons have been described to display electrophysiological properties *in vitro* similar to $ChAT^+$ slow-firing neurons such as the occurrence of a very small I_h. However, nearly half of the glutamatergic neurons exhibited cluster firing properties (Sotty et al., 2003). Likewise, in an *in vitro* septo-hippocampal preparation VGLUT2 expressing MSvDB neurons built a highly heterogenous group of cells displaying different electrophysiological properties characterized by slow-, fast-, burst-, or cluster-firing patterns (Huh et al., 2010). The cluster-firing pattern appeared to be unique to glutamatergic MSvDB neurons. Remarkably, cells exhibiting fast-firing properties possessed a prominent I_h and showed rhythmic spontaneous firing similar to GABAergic MSvDB neurons.

1.5.9. Intraseptal connectivity

There are extensive anatomical and functional interactions between the three main groups of MSvDB neurons: Earlier anatomical studies demonstrated that non-cholinergic MSvDB neurons are contacted by putative cholinergic terminals (Bialowas and Frotscher, 1987; Léránth and Frotscher, 1989). From a functional perspective, carbachol elicited a depolarization in putative glutamatergic MSvDB neurons in an intact half-septum preparation (Manseau et al., 2005), and acetylcholinesterase (AChE) inhibitors were shown to activate septo-hippocampal GABAergic neurons in rat hippocampal slices *in vitro* (Wu et al., 2003b). The latter excitatory effects on GABAergic MSvDB neurons were mediated via muscarinic receptors of the M3 subtype with no involvement of nicotinic receptors. Further support for the absence of postsynaptic nicotinic

[1] This current can underlie rhythmic pacemaker activity, as the underlying channel's opening is caused by hyperpolarizing the neuron's membrane potential, but the channel inactivates during depolarization, thereby leading to intrinsically generated rhythmic changes of the neuron's membrane potential.

responses within the MSvDB is provided by paired recordings with presynaptic cholinergic neurons performed in mouse slices (Leao et al., 2014). Nevertheless, nicotine application to MSvDB slices from rats evoked depolarization and an increase of spiking rates in septo-hippocampal GABAergic neurons (Wu et al., 2003a). However, these effects required the recruitment of a local glutamatergic septal network, which was further confirmed anatomically by showing VGLUT immunoreactive terminals making contacts with PV^+ septo-hippocampal neurons. Moreover, the glutamatergic axons within the MSvDB remained intact after lesions of afferent inputs to the septal nuclei, indicating that they have an intraseptal origin (Hajszan et al., 2004). Beside the glutamatergic excitatory effects on GABAergic MSvDB neurons, strong glutamatergic responses were also present in electrophysiologically identified putative cholinergic and glutamatergic neurons (Manseau et al., 2005), further confined by immunohistochemical evidence of $VGLUT2^+$ puncta in proximity to $ChAT^+$, $GAD67^+$, and $VGLUT2^+$ neurons. Likewise, in paired recordings in mouse MSvDB slices presynaptic activation of GABAergic neurons produced postsynaptic currents in other MSvDB neurons, with little variability between IPSC amplitudes among different cell types (Leao et al., 2014).

1.5.10. Afferent connections to the MSvDB

The MSvDB itself receives afferent connections from several midline caudal diencephalic nuclei (posterior hypothalamic and supramammillary nucleus), as well as from the raphe nucleus, and the locus coeruleus (Woolf, 1991). Interestingly, electrical stimulation of the brainstem reticular formation elicits hippocampal theta oscillations (Green and Arduini, 1954), probably via activation of the supramammillary nucleus, which innervates cholinergic and GABAergic rhythmically bursting septo-hippocampal MSvDB neurons (Borhegyi et al., 1998; Vertes and Kocsis, 1997). In addition, GABAergic backprojections from hippocampal and entorhinal cortex long-range interneurons exist (Woolf, 1991). Indeed, 94 % of hippocampo-septal axons terminating in the MSvDB are GABAergic (Tóth et al., 1993). Given that the MSvDB has a great impact on rhythmic activity inside the hippocampus, the target cells of the hippocampo-septal backprojection are of special interest. 93 % of the hippocampo-septal projection neurons were immunoreactive for the marker protein somatostatin (SST), and could most frequently observed in the str. oriens of CA1 and CA3, as well as in the hilus (Jinno and Kosaka, 2002). Via anterograde tracing experiments using local injections of phaseolus vulgaris leucoagglutinin into str. oriens of CA1 combined with immunocytochemical double staining for PV and ChAT, Tóth et al. (1993) demonstrated that the majority of hippocampo-septal axon terminals contact PV^+ MSvDB neurons. A smaller number of contacts, however, was also found on $ChAT^+$ neurons. Interestingly, PV^+ septo-hippocampal projection neurons in the MSvDB, which were identified by retrograde tracer injections into the hippocampus, also received input from hippocampo-septal neurons, thereby closing a GABAergic

septo-hippocampo-septal loop. Noteworthy, basal forebrain-projecting glutamatergic pyramidal neurons of the hippocampus mainly target only the lateral septum, which has only very sparse GABAergic connections to MSvDB neurons (Leranth et al., 1992), highlighting the role of the direct hippocampo-septal projection.

1.6. The MSvDB-hippocampus network and neurological disorders

Given the outstanding role of the septo-hippocampal pathway for the modulation of hippocampal network states and learning behavior, it is not surprising that the MSvDB-hippocampus network appears to be affected in neurological disorders, especially Alzheimer's disease (AD) and epilepsy.

AD is the most common form of dementia in the elderly with progressive episodic memory deficits and global impairment of cognitive function at later disease states. The definitive diagnosis of AD is still based on post-mortem histophathological examinations of the patients' brains. AD is characterized anatomically by cortical and white matter atrophy and histologically by the presence of large numbers of extracellular amyloid β (Aβ) plaques, as well as intracellular neuropil threads and neurofibrillary tangles consisting of twisted filaments of hyperphosphorylated tau protein, which also accumulates in the extracellular space after neuronal death (see Serrano-Pozo et al. (2011) for review). The extent of neurofibrillary tangles and neuropil threads found in different brain areas of post-mortem brains correlate with disease states: Neurofibrillary changes are first observed in the entorhinal cortex, spreading to the hippocampus, and finally found in all isocortical areas correlating with neuronal damage (Braak and Braak, 1991). Given the the central roles of acetylcholine and the hippocampal formation for learning and memory, a cholinergic deficit, particularly within the hippocampal formation, has been suggested to contribute to the memory deficits observed in the elderly and particularly in AD. Supporting this hypothesis, the number of $ChAT^+$ neurons was found to be reduced along the entire length of the basal forebrain in aged versus young rats (Smith et al., 1993). Furthermore, the proportion of rhythmically bursting neurons inside the MSvDB was lower in aged versus young rats, especially during immobile arousal states associated with atropine-sensitive theta activity (Apartis et al., 2000). Likewise, a substantial decrease of AChE and ChAT enzyme activity in many cortical areas, including the hippocampus, has been observed in post-mortem tissue of AD patients (Davies, 1979). This led to the use of AChE inhibitors for treatment of mild to moderate AD, which are still the most used drugs for treatment. However, a meta-study on the efficacy of these drugs on clinical outcome showed only small benefits of the medication, questioning the benefit of the treatment (Kaduszkiewicz et al., 2005). Nevertheless, binding of [^{3}H]-labeled nicotine to the DG granule cell layer, the presubiculum, and the parahippocampal gyurs in post-mortem tissue of AD patients was found to be reduced by around 30 % relative to age-matched elderly control subjects (Perry et al., 1995), suggesting a decrease of nAChR expression in these areas. Moreover, $A\beta_{1-42}$

peptide was found to bind to nicotinic receptors of both the $\alpha 7$ and the non-$\alpha 7$ subtype (with higher affinity to the $\alpha 7$ subtype (Wang et al., 2000a,b). On a functional level, this binding has been demonstrated to inhibit nicotinic currents in rat hippocampal slices (Pettit et al., 2001). Recently, research therefore focused on the role of nicotinic AChRs, especially of the $\alpha 7$ subtype, for possible treatment options in AD (Vallés et al., 2014). Beside the involvement of the cholinergic system and the hippocampus in AD, no specific role of the septo-hippocampal cholinergic system has crystallized so far. Understanding the physiological function of the septo-hippocampal cholinergic system therefore remains an important step in basic research. This applies not only for AD, but also for other neurological disorders, e.g. epilepsy.

Epilepsy is not a singular disease entity, but a group of neurological disorders characterized clinically by an enduring predisposition to generate epileptic seizures (Fisher et al., 2005). An epileptic seizure is defined as a transient occurrence of signs and/or symptoms due to abnormal excessive or synchronous neuronal activity in the brain (Fisher et al., 2005). One widely used animal model of epilepsy in basic research is the pilocarpine-induced epilepsy model. *In vivo* application of the mAChR agonist pilocarpine (together with methyl-scopolamine to block the action of pilocarpine on AChRs in the periphery) readily induces epileptic seizures and may lead to status epilepticus, resulting in spontaneous recurrent seizures following a latent period of epileptogenesis (Friedman et al., 2007). However, under physiological conditions, septal cholinergic neurons appear to suppress seizure activity, as indicated by a study from Ferencz et al. (2001), in which the authors showed that cholinergic septo-hippocampal deafferentiation facilitated hippocampal kindling in rats. Interestingly, chronic epileptic rats show a neuronal loss in the medial and lateral septum, which is mainly due to the loss of GABAergic neurons (80–97 %), suggesting that the processing of information in the septo-hippocampal networks might be altered (Garrido Sanabria et al., 2006). In line with the hypothesized role of GABAergic MSvDB neurons for pacing hippocampal theta rhythm, early deficits are observed in spatial memory and theta rhythmic activity in such chronic epileptic rats (Chauvière et al., 2009). Conversely, epileptic seizures are less frequent during behavioral states associated with hippocampal theta rhythmic activity, e.g. active wakefulness or REM sleep, and microinjections of the muscarinic agonist carbachol into the MSvDB not only elicited theta rhythmic activity, but also stopped pentylenetetrazol-induced facial-forelimb seizures in rats (Miller et al., 1994). Further highlighting the role of a theta rhythmic functional network state inhibiting seizure production, electrical stimulation of the MSvDB at the theta frequency range had similar effects as the carbachol microinjection. Degeneration of septal neurons, as observed in AD, might also contribute to epileptic seizures, which have a very high prevalence of 10–22 % in AD patients (Mendez and Lim, 2003).

1.7. Key questions

Given that most of the previous studies on cholinergic MSvDB neuron function were obtained using either pharmacological manipulation or permanent lesions, I studied the effect of transient, temporally precise, and cell-type specific cholinergic MSvDB neuron activation on hippocampal network dynamics in an intact network *in vivo*. This study was made possible by the recent development of optogenetic techniques allowing cell type specific and millisecond-precise stimulation of neurons, as well as synaptic release of neurotransmitters. To study hippocampal network dynamics, I used silicon probe recordings of hippocampal single unit and LFP signals, and analyzed spike-phase coupling. Keeping in mind the important role of acetylcholine for hippocampus-dependent learning and memory, I focused on area CA3 of the hippocampus, because area CA3 is an autoassociative network, which is hypothesized to be in the center of the retrieval process of previously encoded information. Since the cholinergic MSvDB neurons target hippocampal neurons directly (direct pathway), and additionally have extensive intraseptal connections to other cell types, which again project to the hippocampus (indirect pathway), I asked which of the effects on hippocampal network activity are mediated via the direct or indirect pathway, and how these pathways might act together in order to structure hippocampal firing patterns. To differentiate between the two pathways I combined the optogenetic stimulation and hippocampal recordings with local application of cholinergic antagonists either into the MSvDB or the dorsal hippocampus. Furthermore, I studied the effect of cholinergic MSvDB neuron activity on other septal cell types.

2. Materials and Methods

2.1. Mice

B6;129P2-Pvalb$^{tm1(cre)Arbr}$/J PV-IRES-Cre (PV-Cre) knockin mice and B6;129S6-Chat$^{tm1(cre)Lowl}$/J ChAT-IRES-Cre (ChAT-Cre) knockin mice were purchased from "The Jackson Laboratory" (USA). Adult homozygous PV-Cre and heterozygous ChAT-Cre mice of both sexes were used for experiments. PV-Cre mice were bred as homozygotes, and ChAT-Cre mice as heterozygotes (wild type female mice were interbred with heterozygous male mice). Mice were maintained in an animal facility under pathogen free conditions on a 12 h light-dark cycle in groups of two to four animals per cage with free access to rodent chow and water. Male mice were separated and housed as singles if they had undergone surgery. Genotyping of ChAT-Cre and PV-Cre mice was performed via polymerase chain reaction (PCR) for Cre-recombinase (see Table 2.1 for primer sequences, Table 2.2 for PCR reaction components, and Table 2.3 for cycling steps) followed by gel electrophoresis on a 1.5 % agarose gel (85 V for 30–45 min). DNA samples for genotyping were obtained by lysis of tail biopsies obtained from mice aged $\leq$21 days using the Direct PCR© Tail Lysis Reagent (Cat. No. 31-101-T, peqlab, VWR International GmbH, Erlangen, Germany). To this end, the tissue sample was incubated for 4 h at 55 °C in 140 μl Direct PCR© Tail Lysis Reagent mixed with 20 μl Proteinase K (Cat. No. 70663, Merck Millipore, Merck KgaA, Darmstadt, Germany) and 140 μl Ampuwa® water (Fresenius Kabi Deutschland GmbH, Germany). After incubation of the lysis mix at 86 °C for 45 min in order to inactivate the Proteinase K-component, the mix was used as the DNA sample for PCR.

All animal experiments were conducted in accordance with the guidelines of the Animal Care and Use Committee of the University of Bonn.

2.2. Transduction

We used a recombinant adeno-associated virus (rAAV) of the serotype 2 genome contained in a hybrid serotype 1 and 2 capsid (S2/1) carrying the humanized channelrhodopsin 2 with the H134R mutation for larger stationary photocurrents (ChR2, Nagel et al. 2005) fused to the enhanced yellow fluorescent protein (eYFP) in a double floxed inverted open reading frame (DIO) under control of the constitutive human elongation factor-1α (EF-1α) promoter and followed by the woodchuck hepatitis virus posttranscriptional regulatory element (WPRE). This rAAV was

Table 2.1 – Primer sequences for genotyping of ChAT-Cre and PV-Cre mice

Primer type	Sequence
Forward	CCATCTGCCACCAGCCAG
Reverse	TCGCCATCTTCCAGCAGG

The expected result after separation of the PCR products by gel electrophoresis is a 281 bp band verifying the presence of the Cre-recombinase gene.

Table 2.2 – PCR reaction components for genotyping of ChAT-Cre and PV-Cre mice

Reaction component	Volume (μl)
REDExtract-N-Amp™ PCR Ready Mix™	7
10 μM forward primer	0.5
10 μM reverse primer	0.5
DNA sample	2.0

Table 2.3 – PCR cycling steps for genotyping of ChAT-Cre or PV-Cre mice

Step #	Temperature (°C)	Time	Note
1	95	5 min	—
2	95	30 s	—
3	60	40 s	—
4	72	50 s	repeat steps 2–4 for 35 cycles
5	72	10 min	—
6	10	—	hold

injected under stereotactical control into the MSvDB of ChAT-Cre or PV-Cre mice to achieve specific expression of ChR2-eYFP in cholinergic neurons or GABAergic neurons, respectively. The plasmid (Addgene plasmid 20298) was provided by Karl Deisseroth (Stanford University), and the rAAV was produced in the lab of Susanne Schoch (University of Bonn) using the following protocol published by van Loo et al. (2012). rAAV2/1 genomes were generated by large scale triple transfection of HEK293 cells. The adeno-associated virus (AAV)-EF1α-DIO-ChR2-eYFP-WPRE plasmid, helper plasmids encoding rep and cap genes (pRV1 and pH21), and adenoviral helper pFΔ6 (Stratagene, Agilent Technologies, Santa Clara, CA, USA) were transfected using standard $CaPO_4$ transfection. Cells were harvested ca. 60 h after transfection. Cell pellets were lysed in the presence of 0.5 % sodium deoxychalate (Sigma-Aldrich, St. Louis, MO, USA) and 50 units/ml Benzonase endonuclease (Sigma-Aldrich, St. Louis, MO, USA). rAAV particles were purified from the cell lysate by HiTrap™ heparin column purification (GE Healthcare, Chalfont St Giles, UK) and then concentrated using Amicon Ultra Centrifugal Filters (Merck Millipore, Merck KgaA, Darmstadt, Germany) until a final stock volume of 500 μl was reached. Purity of viral particles was validated by Coomassie Blue staining of sodium-dodecylsulfate polyacrylamide gels loaded with 7–15 μl virus stock.

For virus injection, mice with an age of six to ten weeks were anesthetized via an intraperitoneal (i.p.) injection of ketamine (100 mg/kg body weight, WDT, Garbsen, Germany) and medetomidine (1 mg/kg body weight, Domitor®, Orion Pharma GmbH, Hamburg, Germany). Both drugs were diluted in sterile 0.9 % sodium chloride solution (Fresenius Kabi Deutschland GmbH, Bad Homburg, Germany) to inject a volume of 100 μl per 10 g body weight. During surgery, mice were kept on a 37 °C heating table and eye ointment (Bepanthen®, Bayer, Leverkusen, Germany) was used to prevent corneal drying. Local anesthesia (10 % lidocaine, Xylocain® pumpspray, AstraZeneca, London, UK) was applied to the skin above the skull before making an incision to expose the skull surface. After scraping away the pericranium a burr hole was made at a stereotactically identified site above the MSvDB (see Table 2.4) with a micro drill (OmniDrill 35, WPI, Sarasota, FL, USA) and a 0.8 mm carbide ball mill (WPI, Sarasota, FL, USA). The stereotactic coordinates were taken from the atlas of Paxinos and Franklin (2008) (see Tables 2.4 and 2.5). The needle was implanted using a polar angle of 10° to prevent rupturing the superior sagittal sinus. A total amount of 2 μl was injected via a microcontroller (SYS-MICRO4, WPI, Sarasota, FL, USA) operated electrical micropump (UMP3, WPI, Sarasota, FL, USA) at a rate of 100 nl per min through a 34 g beveled needle (NanoFil, WPI, Sarasota, FL, USA) at two ventral sites (1 μl at each site, see Table 2.5). The needle was kept in place for 3 min after injection at the first position and for 5 min after injection at the second position before withdrawal to prevent backflow of the virus. A broadband antibiotic ointment (Polyspectran®, Alcon Pharma GmbH, Freiburg i.B., Germany) was applied to the wound, and the skin was sutured using an absorbable antibacterial thread (Coated VICRYL® Plus antibacterial (polyglactin 910) 5-0 RB1

Table 2.4 – Drilling coordinates and implantation parameters for viral injection from bregma

AP (cm)	L (cm)	V (cm)	Azimuth angle(°)	Polar angle(°)
+0.10	+0.07	−0.48 and −0.44	−90	10

The azimuth and polar angle coordinates refer to a spherical coordinate system with the anteroposterior axis defining the 0° azimuth and the dorsoventral axis defining the 0° polar angle. AP = anteroposterior, L = lateral (+ right hemisphere), V = ventral.

Table 2.5 – Target coordinates for viral injection from bregma

AP (cm)	L (cm)	V (cm)
+0.10	0.00	−0.47 and −0.43

AP = anteroposterior, L = lateral, V = ventral.

0.70 suture, Johnson & Johnson Medical GmbH, Ethicon Deutschland, Norderstedt, Germany). Buprenorphine hydrochloride (50 µg/kg body weight, B9275, Sigma-Aldrich, St. Louis, MO, USA) for analgesia and atipamezole (5 mg/kg body weight, Antisedan, Orion Pharma, Hamburg, Germany) for antagonizing medetomidine were injected i.p. after surgery. Both drugs were diluted in 0.9 % sodium chloride solution to inject a volume of 50 µl per 10 g body weight in case of the buprenorphine dilution, or 100 µl per 10 g body weight in case of the medetomidine solution. Mice were housed for at least three weeks before performing electrophysiological experiments to give the mice time to recover and ChR2 time to accumulate in the cell membrane.

2.3. *In vivo* electrophysiological recordings

Electrophysiological recordings *in vivo* were performed in urethane-anesthetized mice, implanted with a light fiber (0.22 numerical aperture (NA), 550 µm core, BFL22-550, Thorlabs, Newton, NJ, USA) to illuminate the MSvDB, a 1.2 mm major diameter screw (00-96x1/16 mouse screw, PlasticsOne, Roanoke, VA, USA) serving as the ground and reference electrode above the cerebellum, and a silicon probe (A4x8-5mm-100-400-413-A32, NeuroNexus®, Ann Arbor, MI, USA) for electrophysiological recordings of LFPs and single unit activity in the right hemisphere of the dorsal hippocampus. In experiments with focal drug application, an additional injection needle (34 g beveled NanoFil, WPI, Sarasota, FL, USA) was lowered to the MSvDB or into the dorsal hippocampus for drug delivery.

2.3.1. Surgery

For electrophysiological experiments mice were anesthetized via two i.p. injections of urethane (U2500, Sigma-Aldrich, USA) separated by 30–45 min. Urethane was dissolved at a concentration of 0.1 g/ml in Ampuwa® water. The first injection was done at a concentration of 1.5 g/kg body weight (150 μl per 10 g body weight), the second at 0.375 g/kg body weight (37.5 μl per 10 g body weight). The mouse's head was fixed inside a stereotactic frame (Model 900, David Kopf Instruments, USA), while mice were kept on a heating plate to keep their body temperature stable between 36 °C and 37 °C throughout the experiment. Body temperature was monitored via a rectal probe. 200 μl of Glucosteril® 5 % (Fresenius Kabi Deutschland GmbH, Germany) were administered subcutaneously every two hours until the end of the experiment. Local anesthesia (10 % lidocaine, Xylocain® pumpspray, AstraZeneca GmbH) was applied to the skin over the skull before making an incision to expose the skull surface. After scraping away the pericranium holes were drilled with a micro-drill (OmniDrill 35, WPI, Sarasota, FL, USA) and a 0.8 mm carbide ball mill (Size #1, WPI, Sarasota, FL, USA) to implant the end of the bare light fiber into the MSvDB, and a 1.2 mm carbide ball mill (Size #3, WPI, Sarasota, FL, USA) to implant the 1.2 mm major diameter screw above the cerebellum serving as the ground electrode. For experiments with focal injections into the MSvDB or hippocampus, an additional hole was drilled for insertion of the injection needle. A cranial window was drilled with a 0.7 mm carbide ball mill (Size #1/2, WPI, Sarasota, FL, USA) and the dura mater was removed above the dorsal hippocampus to implant a silicon probe. For focal drug delivery to the MSvDB, the tip of the injection needle was positioned just above the MSvDB, for focal drug delivery to the dorsal hippocampus, the tip of the injection needle was targeted to str. radiatum of CA3, 200 μm rostral to the nearest shank of the silicon probe. See Tables 2.6 and 2.7 for the stereotactic coordinates (Paxinos and Franklin, 2008). In experiments with focal drug application, the microsyringe needle for focal drug injections was carefully advanced in a stepwise manner to the final position just above the MSvDB using a 3-axis micromanipulator (Model Min 25-X/Y/Z R, Luigs & Neumann, Ratingen, Germany) and an SM-5 controller (Luigs & Neumann, Ratingen, Germany). Hippocampal field potentials were recorded simultaneously. This allowed me to monitor if the needle insertion itself affected the effects of medial septal optogenetic stimulation. This was never the case if the final location of the needle tip was above the MSvDB as described. I did, however, observe strong effects of microinjection needle insertion if the needle tip was advanced further into the MSvDB. Data from these recordings were discarded.

I used electrocardiography to monitor the heart rate of the mouse throughout the experiment. To this aim, a steel needle was placed beneath the skin of the fore- or hindpaw, and electrocardiography (ECG) was performed using the EPMS 07 modular amplifier system (NPI Electronic GmbH, Tamm, Germany) housing a BRAMP-01R amplifier with a gain of 10, and a BF-48DGX

Table 2.6 – Drilling coordinates and implantation parameters for *in vivo* electrophysiology

	AP (cm)	L (cm)	Radial distance (cm)	Azimuth angle(°)	Polar angle(°)
Light fiber	+0.10	−0.07	−0.40 [a]	-90	10
MSvDB inj. needle	+0.16	+0.06	−0.41 [b]	45	10
Hipp. inj. needle	+0.01	+0.27	−0.27 [b]	55	45
Silicon probe	−0.17	+0.10 to +0.22	−0.22 [c]	90	0

AP = anteroposterior from bregma, L = lateral (+ right, − left hemisphere) from bregma, [a] from skull surface, [b] from bregma, [c] from cortical surface, Hipp. = hippocampus.

Table 2.7 – Target coordinates from bregma for *in vivo* electrophysiology

	AP (cm)	L (cm)	V (cm)
Light fiber	+0.10	0.00	−0.40
MSvDB inj. needle	+0.12	+0.02	−0.40
Hipp. inj. needle	−0.15	+0.16	−0.19
Silicon probe	−0.17	+0.10 to +0.22	−0.24

AP = anteroposterior, L = lateral (+right hemisphere), V = ventral, Hipp. = hippocampus.

differential amplifier/filter module used for signal filtering (300 Hz low-pass, 0.3 Hz high-pass, and notch filter). ECG signals were acquired continuously at 1 kHz using a MiniDigi 1B acquisition system and AxoScope 10.2 software (Molecular Devices, Sunnyvale, CA, USA).

2.3.2. Data acquisition

The silicon probe (A4x8-5mm-100-400-413-A32, NeuroNexus®, Ann Arbor, MI, USA) used for *in vivo* recordings of LFP and single unit activity had 32 electrode contacts, each with a surface area of 413 μm^2, distributed on four 15 μm thick shanks with each shank having eight electrodes vertically distributed with 100 μm spacing. The distance between shanks was 400 μm. Intrahippocampal LFP signals were amplified (100 x) and acquired continuously at 48 kHz on a 32-channel recording system with 16 bit resolution (dacqUSB, Axona, St. Albans, UK).

2.3.3. Reconstruction of electrode position

For determination of the electrode positions, a micro-spatula tip of a high molecular weight (500,000 MW) lysine-fixable biotinylated dextran conjugate (Cat. No. D-7142, Molecular Probes®, Life Technologies, Carlsbad, CA, USA) was dissolved in deionized water and carefully applied to the silicon probe shanks with a small brush before surgery. After surgery, the mouse was deeply anesthetized via an i.p. injection of ketamine (100 mg/kg body weight) and xylazine (20 mg/kg body weight) and heart perfusion was performed with 5 ml Ringer solution (Fresenius Kabi Deutschland GmbH, Bad Homburg, Germany) at a rate of 2 ml/min, while the abdominal aorta was clamped. The brain was removed and stored for 4 days at 4 °C in a fixation solution containing 4 % methanol-stabilized formalin (Cat. No. F1635, Sigma-Aldrich, St. Louis, MO, USA), dissolved in phosphate buffered saline (PBS, Cat. No. L 182-10, Biochrom AG, Berlin, Germany). Fifty μm thick coronal slices were cut with a vibratome (VT1000S, Leica Microsystems GmbH, Wetzlar, Germany) in ice-cold PBS solution and subsequently stained with a streptavidin conjugated green fluorescent dye (Alexa Fluor® 488 Streptavidin, Molecular Probes®, Life Technologies, Carlsbad, CA, USA), diluted 1:500. The track and tip position of the silicon probe shanks were identified and used for electrode position reconstruction, corrected for 5 % estimated tissue shrinkage. Data from electrodes, whose position could not be determined unambiguously, were excluded from further analysis.

2.4. Pharmacology

For systemic i.p. injections of atropine, we used atropine sulfate monohydrate (Cat. No. A0257, Sigma-Aldrich, St. Louis, MO, USA) at a concentration of 50 mg/kg body weight. Atropine sulfate monohydrate was dissolved in sterile 0.9 % sodium chloride solution at 5 mg/ml to inject a volume of 100 μl per 10 g body weight. For focal injections of atropine into the MSvDB, we used atropine sulfate monohydrate at a concentration of 7.2 mM, dissolved in artificial cerebrospinal fluid (ACSF, consisting of (in mM): NaCl, 125; KCl, 3.5; NaH_2PO_4, 1.25; $NaHCO_3$, 26; $CaCl_2$, 2; $MgCl_2$, 2; D-glucose, 15; Sigma-Aldrich, St. Louis, MO, USA). A total volume of 300 nl was injected at a rate of 100 nl/min via a microcontroller operated electrical micropump through a 34 g beveled needle (see section 2.2). Data for the condition post MSvDB injection were acquired between 20–60 min after the end of the injection procedure. For focal injections into the hippocampus, we used a blocker cocktail of atropine sulfate monohydrate (7.2 mM), mecamylamine hydrochloride (10 mM, Cat. No. 2843, Tocris, Bristol, UK), and methyllycaconitine citrate (20 μM, Cat. No. 1029, Tocris, Bristol, UK) dissolved in ACSF. Since, in comparison to the more spatially confined MSvDB, the hippocampus is a very large structure, I injected 10 times 200 nl at a rate of 100 nl/min, i.e. a total volume of 2 μl over a time course of one hour,

to allow diffusion of blocker solution over the entire dorsal hippocampus. Data for the post hippocampal injection condition were acquired 10 min after the end of the injection procedure for up to 90 min.

2.5. *In vivo* optical stimulation

For optical stimulation a software-controlled 473 nm continuous wave diode laser (LuxX® 473-80, Omicron Laserprodukte GmbH, Rodgau-Dudenhofen, Germany) was coupled via a FC/PC connection to the light fiber (0.22 NA, 550μm core, BFL22-550, Thorlabs, Newton, NJ, USA) used for implantation. The laser power was adjusted before each experiment to yield a light power of 45 mW exiting the bare light fiber end.

2.6. Immunohistochemistry

Heart perfusion for rapid brain fixation was performed as described for the reconstruction of electrode position. Formalin-fixated brains were stored until slicing in storing solution (PBS with 0.1 % sodium azide (Cat. No. 822335, Merck Millipore, Merck KgaA, Darmstadt, Germany) at 4 °C. Fifty μm thick coronal slices were cut with a vibratome in PBS and stored in storing solution in 24-well plates (Cat. No. 83.3922, Sarstedt AG & Co, Nümbrecht, Germany) at 4 °C until staining. For staining, slices were briefly washed with PBS and submerged for 10 min in 0.25 % Triton X-100 (Sigma-Aldrich, St. Louis, MO, USA), solved in PBS. For the following steps slices were washed three times for 10 min between each solution change. Slices were submerged over night at 4 °C in PBS solution containing the first antibodies and for 2 hours at room temperature (RT) in PBS solution containing the secondary antibodies. For costaining of ChAT and eYFP, goat anti ChAT affinity purified polyclonal antibody (Cat. No. AB 144P, Merck Millipore, Merck KgaA, Darmstadt, Germany), diluted 1:500, and rabbit anti-green fluorescent protein (GFP) affinity purified polyclonal antibody (ab6556, abcam®, Milton, UK), diluted 1:1000, were used as first antibodies. Cy3 conjugated donkey anti goat IgG polyclonal antibody (Cat. No. AP180C, Merck Millipore, Merck KGaA, Darmstadt, Germany), diluted 1:1000, and FITC conjugated donkey anti rabbit IgG polyclonal antibody (Cat. No. 711-096-152, Dianova, Hamburg, Germany), diluted 1:1000, were used as secondary antibodies. For costaining of PV and eYFP, rabbit anti PV serum (PV 25, swant®, Marly, Switzerland), diluted 1:1000, and goat anti-GFP polyclonal antibody (ab5449, abcam®, Milton, UK), diluted 1:1000, were used as first antibodies.Cy3 conjugated donkey anti rabbit IgG polyclonal antibody (711-156-152, Dianova, Hamburg, Germany), diluted 1:1000, and FITC conjugated donkey anti goat IgG polyclonal antibody (705-095-147, Dianova, Hamburg, Germany), diluted 1:1000, were used as secondary antibodies. After the

last washing step slices were mounted onto microscope slides (Superfrost® Plus, Thermoscientific, Gerhard Menzel GmbH, Braunschweig, Germany) in Aqua-Poly/Mount (Polysciences, Inc., Warrington, PA, USA) mounting medium and covered with cover slips (Engelbrecht, Medizin- und Labortechnik GmbH, Edermünde, Germany). Staining of eYFP$^+$ fibers in hippocampal slices was performed according to the same protocol as used for the ChAT and eYFP costaining described above. Z-stacks with 1–2 μm inter-optical plain distances were obtained with a confocal microscope (Model A1/Ti-E, Nikon, Tokyo, Japan) using a 10 x-objective.

2.7. Data analysis

2.7.1. Local field potential analysis

LFP data were digitally downsampled to 1 kHz. Power spectral density analysis was performed using the Matlab software toolbox "FieldTrip" (Oostenveld et al., 2011). Signal preprocessing involved subtraction of the mean of the signal from each signal data point, so that the signal oscillated around zero (demeaning), and 50 Hz line noise removal via a Fourier notch filter. For quantification of stimulation induced theta synchronization, we calculated the corrected theta peak power as follows: Power spectral density was determined for every trial for a 10 s baseline period and a 10 s period beginning and ending 2 s later than the 10 s optogenetic stimulation period, in order to account for the delayed on- and offset of induced theta oscillations. Values for power spectral densities were then averaged across trials for each animal. For calculation of power spectral density the signal was tapered with Slepian sequences and multitaper fast Fourier transform was performed with a spectral smoothing of ± 0.5 Hz. Theta peak power was measured relative to the power of the adjacent frequencies. The power of the adjacent frequencies contributing to the absolute power value at the theta peak frequency was estimated by linear interpolation between the minima surrounding the theta peak. If no theta peak was detectable (as usually in the baseline period), theta peak power was considered to be zero. The optogenetic stimulation effects were then quantified as the difference between the theta peak power during stimulation and the theta peak power during the baseline period, yielding the corrected theta peak power.

For analyzing the time course of the diminishment of stimulation-induced theta oscillations by the incremental hippocampal blocker cocktail injections, power spectral density was determined for the 30 s baseline period and a 10 s period beginning and ending 2 s later than the 10 s optogenetic stimulation period (see above) for each trial in every animal. Z-scores were calculated for the baseline and stimulation-associated period to reflect the change in power spectral density in units of the standard deviation of baseline power spectral density across trials. Since LFP power

increases with time for all frequencies—presumably because of decreasing depth of anesthesia—I performed a baseline correction for every trial, so that baseline corrected z-scores reflect the difference between z-scores of the stimulation-associated period and the z-scores of the baseline period.

To reliably reflect changes in the broader slow gamma range, we quantified slow gamma power binned over the frequency range from 26–48 Hz for 10 s baseline and stimulation epochs. Power spectral density plots often showed sharp peaks at exactly the stimulation frequency and its harmonics. Since I could not exclude the possibility that these peaks reflect artifacts of unspecific stimulation or photoelectric effects, I excluded the stimulation frequencies and their first two harmonics ±0.5 Hz from gamma power analysis. Optogenetic stimulation effects were calculated as the difference between the gamma power during the stimulation period and the baseline period. To assess the effect size of systemic atropine application on changes in baseline corrected theta peak power or baseline corrected slow gamma power, I compared the area under the curve over stimulation frequencies from 3–40 Hz pre versus post application of systemic atropine. Statistical significance was assessed using Wilcoxon signed-rank test or Student's paired t-test.

To analyze the power change over time, time-frequency analysis using the Hanning taper was performed with a 5 s sliding time window sliding over the data in 0.625 s steps. A z-score was assigned to each time bin and frequency bin for each single trial using the full epoch trial length as the baseline for z-score calculation. Z-scores were then averaged across trials and classical pre-stimulus baseline corrections were performed to make the prestimulus z-score values oscillate around zero. This approach has been shown to be more robust against single trial noise compared to classical correction methods (Grandchamp and Delorme, 2011).

For quantification of LFP power changes at the stimulation frequencies during stimulation of PV^+ MSvDB neurons, z-scores were averaged across the 5 s midtime interval of stimulation and across ± 0.2 Hz around the stimulation frequency.

2.7.2. Single unit analysis

For offline spike sorting of unit activity, the wideband signal was digitally high-pass filtered (0.3–3 kHz, second order elliptic filter with 0.1 dB of ripple in the passband, and a stopband 40 dB down from the peak value in the passband). Unsupervised automatic spike detection and sorting, followed by manual adjustment of the clusters, was done with the Matlab (The MathWorks®, Inc., Natick, MA, USA) software toolbox "Wave_clus" (Quiroga et al., 2004). The threshold for spike detection was set to at least 4 times an estimated standard deviation σ of the bandpass-filtered signal x ($\sigma = median\{\frac{|x|}{0.6745}\}$, see Quiroga et al., 2004). Compared to the classical standard deviation, the median based estimated standard deviation is more robust against outliers. Sorted units were classified as single units, multi units, or artifacts based on spike shape, ratio between

spike peak value and noise level, the inter-spike interval distribution of each cluster, and presence of a refractory period (< 3 ms) for the single units. In addition, crosscorrelograms were used to verify the clustering procedure as described by Harris et al. (2000). Putative interneurons and principal cells were classified according to their spike width (time between peak and following minimum) and the mean time of their spike autocorrelogram from 0 ms to 50 ms (Csicsvari et al., 1998). Units with a characteristic "bursty" autocorrelogram (mean time ≤ 26 ms) and a broad waveform (spike width > 0.75 ms) were classified as putative principal cells, and units lacking a "bursty" autocorrelogram (mean time > 26 ms), but possessing a narrow waveform (spike width ≤ 0.75 ms) were classified as putative interneurons. Z-scores reflecting the change of spiking rate relative to baseline were calculated for time bins of 5 s by subtracting the mean firing rate of the pre-stimulus baseline (i.e. the first 30 s of recording) from the trial-averaged firing rates at each time bin and dividing these values by the standard deviation calculated across all time bins of all trials. If the basal spiking rate was zero in each time bin of every trial, but positive during stimulation periods (indicating a very strong modulation effect), the z-score during stimulation would be infinite due to a standard deviation of zero during baseline. To include these units into the analysis, a standard deviation was estimated on the assumption that there was one spike during the whole baseline period. For the quantification of the optogenetic stimulation effect on each unit's spiking rate, the z-scores of the time bins during stimulation (30–40 s and 70–80 s) were averaged. At the single unit level, each cell responded either with a positive or a negative change of spiking rate upon stimulation. To quantify the modulation effect at the population level, we calculated a modulation index as the absolute value of the area hyperbolic sine (arsinh) of the firing rate z-scores during stimulation. Taking the arsinh of the z-scores takes into account that the z-score distribution resembles more a lognormal distribution than a normal one. In contrast to a logarithmic scale, the arsinh is defined for both positive and negative values. Taking the absolute value makes the modulation index insensitive to the sign of the modulation, i.e. a unit with increased spiking during stimulation is evaluated as equally modulated as a unit with decreased spiking during stimulation. Note that, at the population level, an increase of modulation would manifest itself in increasing the positive z-scores, but decreasing the negative z-scores, whereas a decrease in modulation would result in shifting both positive and negative z-scores to zero. To quantify the effect of blocker injection compared to ACSF control injections the difference between the modulation index post and pre injection was calculated for each unit and termed the delta modulation index.

2.7.3. Spike-phase coupling analysis

The LFP signal was recorded from an electrode which lay inside or very close to the CA3 principal cell layer, but from which no units were extracted to prevent contribution of the spike signal

itself to the phase of the LFP signal. For offline spike phase coupling analysis, the LFP signal was downsampled to 2 kHz and the mean of the signal was subtracted from each data point (demeaning) to make the signal oscillate around zero. After band-pass filtering in the theta range of 3–6 Hz with a second order Butterworth filter the left and right tails of the signal, each containing 1% of the total signal length, were multiplied with the rising and falling flanks of a modified Welch window. The instantaneous phase could then be determined via a Hilbert transformation, so that each spike could be assigned to the instantaneous LFP theta phase. Spike phase coupling was analyzed for a 30 s baseline period and the stimulation periods (pooled 10 s periods of 12 and 20 Hz stimulation). To quantify changes in spike-phase coupling during stimulation, the number of significantly theta phase-coupled interneurons and principal cells were determined using Kuiper's test to identify significant phase coupling with the alpha level for type I error set to 0.05. Since the power of Kuiper's test depends on the number of spikes, the number of spikes during the stimulation and baseline periods were equalized by random deletion of spikes from the condition which contained more spikes. To make this process more consistent, Kuiper's test was applied to the mean across 100 repetitions of random spike deletions. To answer the question if theta phase-spike coupling is significantly changed at the population level of interneurons and principal cells, the mean resultant vector length was calculated for each neuron's spike-theta phase distribution for the stimulation and baseline period. Statistical significance between the stimulation and baseline periods was then assessed for interneurons and principal cells at an alpha level of 0.05 using Wilcoxon signed-rank test.

2.8. *In vitro* patch-clamp recordings

Experiments in MSvDB slices were performed at least 2 weeks after the virus injection. For obtaining slices, mice were deeply anesthetized with ketamine (300 mg/kg body weight, WDT, Garbsen, Germany) and xylazine (60 mg/kg body weight, Bayer, Leverkusen, Germany). Brains were removed and transferred into cold sucrose-containing carbogen-saturated ACSF containing (in mM): NaCl, 60; sucrose, 100; KCl, 2.5; NaH_2PO_4, 1.25; $NaHCO_3$, 26; $CaCl_2$, 1; $MgCl_2$, 5; D-glucose, 20; Sigma-Aldrich, St. Louis, MO, USA). Horizontal or coronal slices of the MSvDB (300 μm) were cut using a vibratome (Leica VT 1200 S, Wetzlar, Germany), incubated for 30 minutes at 37°C, and transferred into ASCF containing (in mM): NaCl, 125; KCl, 3; NaH_2PO_4, 1.25; $NaHCO_3$, 26; $CaCl_2$, 2.6; $MgCl_2$, 1.3; glucose, 15; Sigma-Aldrich, St. Louis, MO, USA). For electrophysiology, slices were transferred into a submerged chamber and superfused with carbogen-saturated ACSF (speed of superfusion: 3 ml/min., 35°C). Expression of ChR2-eYFP in MSvDB neurons was verified using an upright fluorescence microscope (Nikon Eclipse FN1, Tokyo, Japan, filter settings (in nm): excitation: 500/24; dichroic: 520; emission: 542/27).

Whole-cell patch-clamp recordings were then achieved from identified fluorescent cells or non-fluorescent cells using infrared differential interference contrast microscopy. Pipettes were made using a horizontal puller (Sutter Instruments, Model P-97, Novato, USA) and borosilicate glass capillaries (GB150F-8P, Science Products, Hofheim, Germany). Electrode resistance in the bath ranged from 3–5 MΩ. The intracellular solution for whole-cell current clamp recordings contained (in mM): K-gluconate, 140; 4-(2-hydroxyethyl)-1-piperazineethanesulfonic acid (HEPES), 5; ethylene glycol tetraacetic acid (EGTA), 0.16; $MgCl_2$, 0.5; sodium phosphocreatine, 5; and 0.3 % biocytin. Voltage and current clamp experiments were carried out with a Multiclamp 700B amplifier (Molecular Devices, Sunnyvale, CA, USA). Data were sampled at 10–50 kHz with a Digidata 1322A interface (Molecular Devices, Sunnyvale, CA, USA) controlled by pClamp Software (Molecular Devices, Sunnyvale, CA, USA) and stored on a hard disk for offline analysis. In the experiments, in which cholinergic axons were stimulated while recording from septal neurons, the neurons were classified based on the properties of genetically identified $ChAT^+$ or PV^+ neurons (see Table 3.1). Classification was done by Dr. Heinz Beck, who was blinded to the results of the optogenetic stimulations. As a parameter for segregating septal cell populations, the action potential half width was used, with cells with narrow action potentials (< 0.7 mV) classified as putative PV^+ neurons. These cells also had large fast afterhyperpolarizations (fAHPs) compared to the putative $ChAT^+$ population (-9.4 ± 1.7 vs. -3.6 ± 1.6 mV, mean $\pm$ SEM, $p = 0.027$, t-test), consistent with the properties of the genetically identified populations (see Table 3.1). Action potential properties were analyzed as follows: Action potential threshold was determined as the voltage where the first derivation of the voltage trace exceeded 8 mV/ms. The half width was determined as the action potential width at an amplitude 50 % between the threshold and peak. The fAHP amplitude was determined as the difference between the threshold and the maximal repolarization observed during the first 20 ms after the action potential onset. For all measurements, action potentials were selected that occurred within the first 50 ms after onset of the current injection. In all cells, the lowest possible current injections displaying such action potentials were selected.

2.9. *In vitro* optogenetic stimulation

Light stimulation of individual neurons in the MSvDB (coronal slices) was carried out via the microscope objective (Nikon NIR Apo 60x, Tokyo, Japan) using a galvanometer based scanning system (UGA-40, DL-473, Rapp Optoelectronics, Hamburg, Germany) coupled to a 473 nm diode-pumped solid state laser (DL-473, Rapp Optoelectronics, Hamburg, Germany). EYFP-expressing neurons in the medial septum were targeted with brief flashes of light (20 ms, up to 2 mW laser power) that caused clear light-evoked responses in patch-clamp recordings. Stimulation frequencies ranged from 5–40 Hz. To assess the effects of stimulation of $ChR2^+$ cholinergic

neurons on other types of septal neurons, we used 5 s stimulus trains at a power of up to 60 mW using a 473 nm continuous wave diode laser (LuxX® 473-80, Omicron Laserprodukte GmbH, Germany) coupled into a customized multimode light fiber (0.22 NA, 550 μm core, BFL22-550, Thorlabs, Newton, NJ, USA), and 40 μM 4-AP (Tocris Bioscience, Bristol, UK) was added to the ACSF for reliable optical stimulation. Additional recordings with longer 10 s stimulus trains were carried out in the absence of 4-AP. In these experiments, neurons were classified based on the properties of genetically identified $ChAT^+$ or PV^+ neurons (see Table 3.1). Classification was done by Dr. Heinz Beck, who was blind to the effects of the optogenetic stimulation. The end of the optical fiber was placed immediately above the brain slice surface to illuminate the MSvDB. Optogenetically induced membrane depolarizations were measured relative to baseline.

3. Results

3.1. *In vivo* optogenetic activation of cholinergic MSvDB neurons induces hippocampal rhythmogenesis

To achieve light-based stimulation of cholinergic MSvDB neurons, I used ChAT-IRES-Cre knockin mice expressing Cre recombinase under control of the choline acetyltransferase promoter (see Materials and Methods). These mice were stereotactically injected with an rAAV S2/1 that allows Cre-dependent expression of ChR2(H134R) fused to eYFP. Robust ChR2-eYFP expression could be observed in most ChAT$^+$ neurons as revealed by immunohistochemistry (see Figure 3.1 and Materials and Methods). To test the functional expression of ChR2-eYFP in ChAT$^+$ MSvDB neurons, we obtained *in vitro* patch-clamp recordings from these neurons, which revealed characteristic slow-firing properties, as described previously (Gorelova and Reiner, 1996; Griffith and Matthews, 1986; Markram and Segal, 1990; Serafin et al., 1996; Sotty et al., 2003). Light-based stimulation at 473 nm with a laser focused onto the neuronal somata reliably elicited action potentials even with long-duration (10 s) stimulus trains in all cells (spiking reliability quantified as probability to elicit action potentials per light stimulus of 1 for frequencies up to 5 Hz, and reliabilities of 0.88 ± 0.35, 0.58 ± 0.46, and 0.12 ± 0.25 for 12, 20 and 30 Hz, respectively, mean $\pm$ SD of n = 8 cells, see Figure 3.2).

After establishing light-based stimulation of cholinergic MSvDB neurons, I turned to *in vivo*

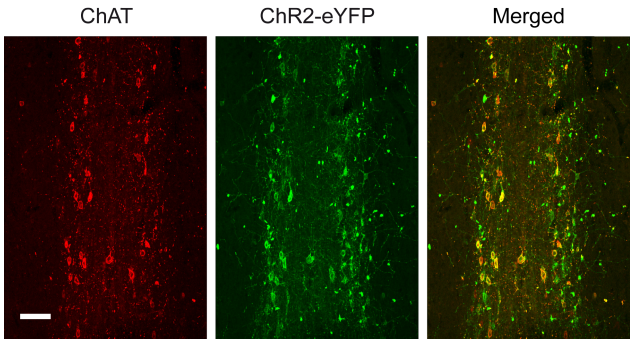

Figure 3.1 – ChR2-eYFP is selectively expressed in ChAT$^+$ MSvDB neurons after virus injection of a Cre-dependent rAAV into the MSvDB of ChAT-Cre mice. Left panel shows fluorescence of Cy3 after immunolabeling of ChAT, middle panel shows fluorescence of FITC after immunolabeling of ChR2-eYFP, and right panel shows the merged signal revealing an overlap of expression patterns. Photographs show the maximum intensity projection of 51 confocal z-stack images across 50 μm. Scale bar is 100 μm.

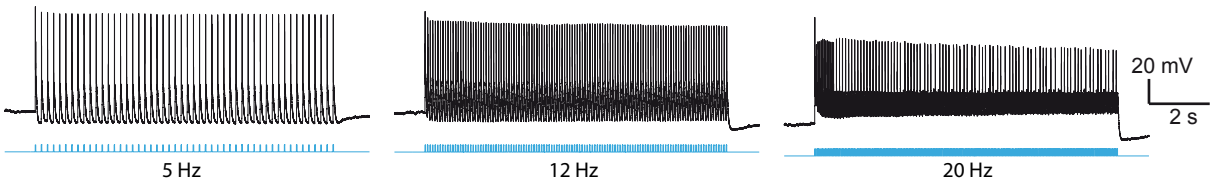

Figure 3.2 – *In vitro* entrainment of a ChAT$^+$-ChR2$^+$ MSvDB neuron evoked by repetitive 473 nm light stimulation of neuronal somata with 20 ms light pulses. Panels show voltage responses to 5 Hz, 12 Hz, and 20 Hz stimulation frequencies of one example MSvDB neuron of an acute *in vitro* slice preparation, which is entrained by light stimulation to reliably elicit action potentials up to a frequency of 12 Hz, but show failures if stimulated at 20 Hz. Patch-clamp recordings performed by Oliver Braganza.

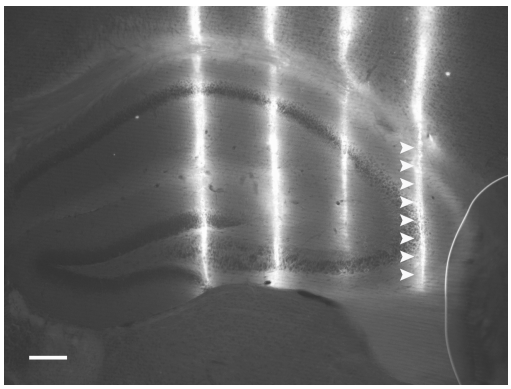

Figure 3.3 – Example reconstruction of electrode positions of one silicon probe. The positions of the four individual shanks of the silicon probe is revealed by fluorescent labeling of dextran-biotin taken up by the cells surrounding the dextran-biotin coated shanks. Extrapolation from the tip position reveals the vertical position of the eight electrodes per shank (see Materials and Methods). Arrowheads mark the reconstructed electrode positions of one shank. Most of these electrodes are placed in hippocampal subfield CA3. Scale bar is 200 μm.

recordings in urethane-anesthetized mice to assess the effects of cholinergic activation on hippocampal rhythmogenesis. I first recorded LFPs from up to 32 channels of a four-shank silicon probe spanning several layers of the dorsal hippocampus (see Figure 3.3) during baseline or light stimulation of cholinergic MSvDB neurons via a light fiber implanted above the MSvDB (see Materials and Methods).

One individual trial lasted 120 s and consisted of a 30 s baseline period, followed by 10 s light stimulation, a 30 s period without stimulation, a second 10 s light stimulation with a different stimulation frequency, and lastly by a 40 s period of recording after cessation of the last stimulation period. Figure 3.4 shows example traces of LFP signals recorded at the eight electrodes of one Silicon probe shank before, during, and after light stimulation at a frequency of 12 Hz.

Optogenetic stimulation of ChR2$^+$ cholinergic MSvDB neurons via a light fiber implanted just above the MSvDB at different stimulation frequencies caused marked changes in hippocampal rhythmicity. To quantify the contribution of different frequency bands to the observed LFP signal, I performed a transformation from the time domain into the frequency domain using the fast fourier transformation (see Materials and Methods). Using a sliding time-window I created time-frequency plots of power spectral density z-scores (see Materials and Methods) to

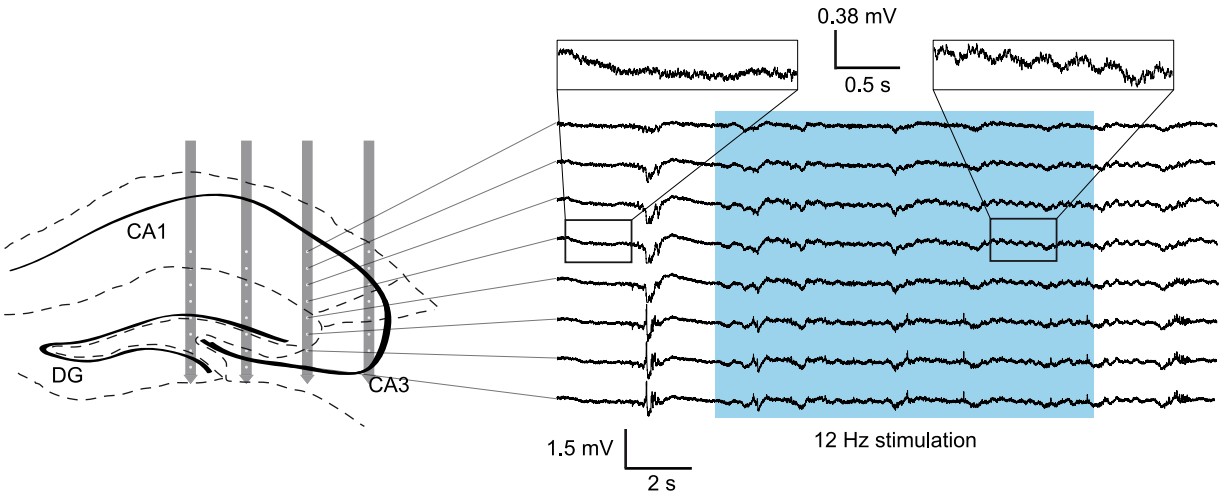

Figure 3.4 – *In vivo* light stimulation of ChR2$^+$ cholinergic MSvDB neurons causes marked changes in hippocampal rhythmicity. Left panel shows a schematic drawing of the four shanks of the silicon probe used for recording. Each shank has eight electrodes with a 100 μm vertical spacing. Right panel shows example traces of LFP signals recorded before, during, and after light stimulation with a 12 Hz train. Blue background indicates the duration of the light stimulation train. Insets show 2 s segments of an example trace before and during light stimulation at a greater magnification. Theta rhythmic activity emerges during light stimulation and persists for some seconds after cessation of the stimulation train.

visualize the change in power spectral density across time. Notably, during stimulation of ChAT$^+$ MSvDB neurons virtually all recordings displayed an increase in theta and slow gamma power (the slow gamma band is defined in this study within the frequency range of 26–48 Hz), which often persisted for some seconds after the cessation of stimulation. This effect was observed in all hippocampal subfields (see Figure 3.5 for example recordings obtained from the CA1, CA3, and DG subfields of one mouse, values represent the mean across five trials).

The most robust effects were observed in the theta range (see insets in Figure 3.5) showing a slow on- and offset in the range of seconds in relation to light stimulation of cholinergic MSvDB neurons. To further quantify the changes in power spectral density evoked by stimulation in comparison to the baseline condition, I compared the power spectra in a 10 s time window shifted for 2 s in relation to the stimulation period in order to account for the delayed on- and offset of stimulation induced theta activity (see Figure 3.6). Notably, increases in synchronization occurred in a narrow frequency range, with a suppression of adjacent frequencies.

The question arises, if the effects on theta synchronization depend on the stimulation frequency. Therefore, I systematically varied the stimulation frequency between 3–40 Hz by using pairs of stimulation frequencies for the two stimulation periods, namely 3 Hz/4 Hz, 6 /8Hz, 5 Hz/10 Hz, 12 Hz/20 Hz, and 30 Hz/40 Hz. Interestingly, the frequency of the observed theta

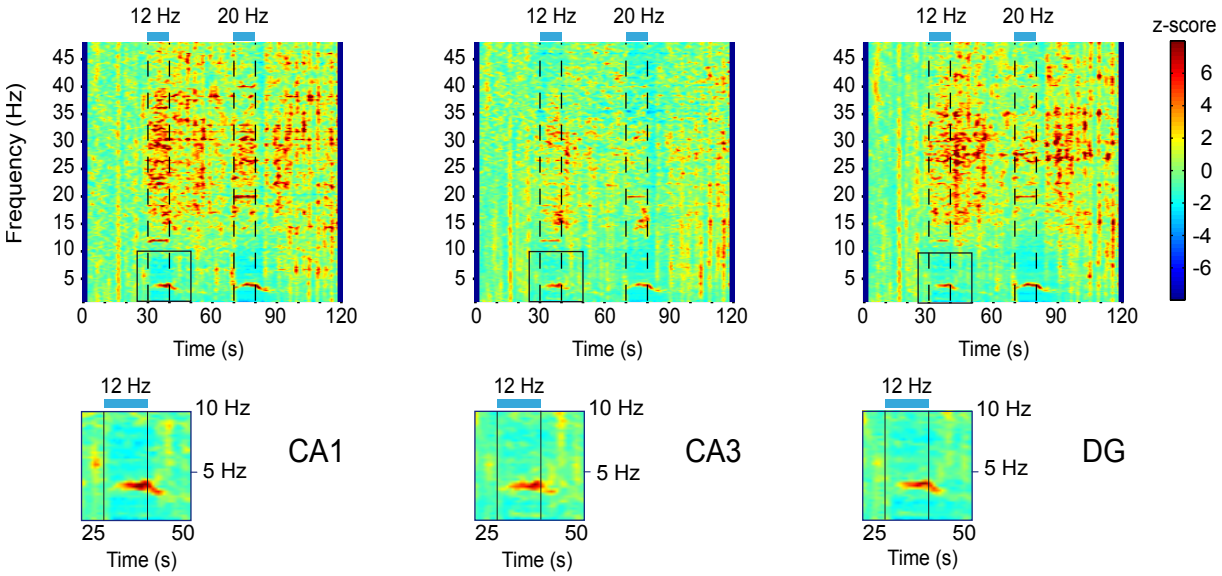

Figure 3.5 – *In vivo* optogenetic stimulation of cholinergic MSvDB neurons controls hippocampal rhythmogenesis. Panels show time-frequency plots of power spectral density z-scores calculated from local field potentials recorded in hippocampal subfields CA1, CA3, and DG of one mouse as a representative example. Baseline activity changes upon light stimulation of ChAT$^+$ MSvDB neurons at 12 Hz or 20 Hz, displaying an increase in theta power, which emerges during approximately the first 2 s of stimulation and decays at a time-scale of seconds after cessation of the stimulation train. In addition, increases in slow gamma power, which persist to some extent after cessation of the stimulus train, are observed. Insets show theta power increase and suppression of adjacent frequency bands during 12 Hz stimulation at a higher magnification. Blue bars on top of the panels indicate duration of stimulation trains. Z-scores are color coded.

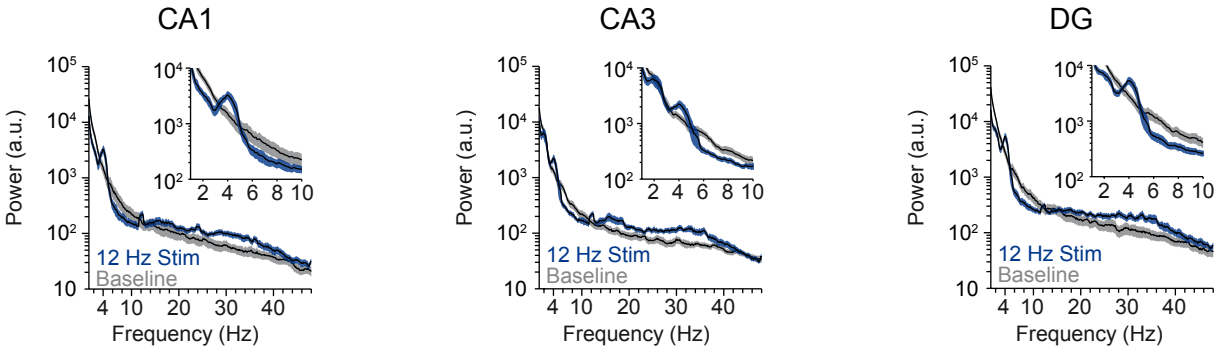

Figure 3.6 – *In vivo* optogenetic stimulation of cholinergic MSvDB neurons induces a power peak at theta and an increase of slow gamma power. Panels show power spectra of 10 s periods shifted 2 s in relation to stimulation to account for the delayed on- and offset of stimulation-induced theta oscillations for hippocampal subfields CA1, CA3, and DG. During 12 Hz stimulation-induced theta activity, theta synchronization occurs in a narrow frequency range with a concomitant suppression of powers at adjacent frequencies. Insets show the theta peak with concomitant suppression of power at adjacent frequencies at a higher magnification.

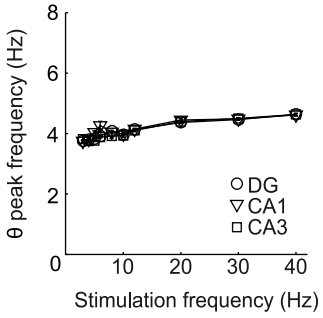

Figure 3.7 – The frequency of stimulation induced theta peak power increases linearly within a narrow frequency range with the frequency of stimulation. This is the case for hippocampal subfields CA1, CA3, and DG. Pearson's correlation coefficient is 0.88 for CA1, 0.97 for CA3, and 0.96 for DG, with p <0.001). Symbols and error bars represent mean ± SEM of six mice with one value missing for CA1 at 40 Hz stimulation.

peak did not vary much with stimulation frequency (from 3.8 to 4.6 Hz). However, inside this narrow frequency range, theta peak frequency was significantly correlated with stimulation frequency (see Figure 3.7, r = 0.88 for CA1, r = 0.97 for CA3, and r = 0.96 for DG, $p < 0.001$; r = Pearson's correlation coefficient, n = 6 mice, 4–6 trials per mouse). To further validate the dependence of theta peak frequency on the stimulation frequency statistically, I performed two-way analysis of variance (ANOVA) with hippocampal subfields CA1, CA3, and DG as one factor, and the different stimulation frequencies as the other factor. This analysis yielded a statistical significant difference between the stimulation frequencies, but not between hippocampal subfields ($F_{Stimulationfrequency(9,149)} = 18.88$, $p < 0.0001$, $F_{Subfield(2,149)} = 1.54$, $p = 0.217$, $F_{Stimulation*Subfield(18,149)} = 0.45$, $p = 0.974$).

Likewise the baseline corrected theta peak power was correlated with stimulation frequency (see Figure 3.8, r = 0.68 for CA1, r = 0.92 for CA3, and r = 0.89 for DG, $p < 0.05$ for CA1, and

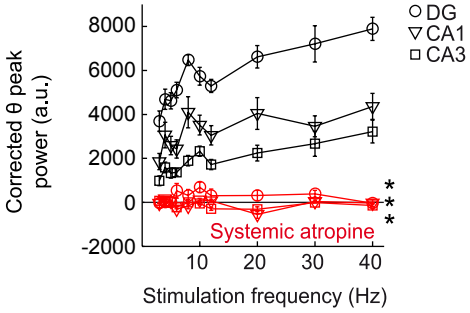

Figure 3.8 – Stimulation induced changes in corrected theta peak power increases linearly with stimulation frequency in hippocampal subfields CA1, CA3, and DG. Pearson's correlation coefficient is 0.68 for CA1, 0.92 for CA3, and 0.89 for DG, with $p < 0.05$ for CA1, and $p < 0.001$ for CA3 and DG. Systemic atropine injections (50 mg/kg body weight, i.p. administration) abolished theta induction in hippocampal subfields CA1, CA3, and DG, * indicates $p < 0.05$, Wilcoxon signed-rank test. Symbols and error bars represent mean ± SEM of six mice.

$p < 0.001$ for CA3 and DG, r = Pearson's correlation coefficient, n = 6 mice). Two-way ANOVA for the stimulation effects on theta power yielded a statistically significant difference between the stimulation frequencies, and between hippocampal subfields ($F_{Stimulationfrequency(9,150)} = 1.98$, $p < 0.05$, $F_{Subfield(2,150)} = 30.39$, $p < 0.0001$, $F_{Stimulationfrequency*Subfield(18,150)} = 0.15$, $p > 0.99$).

These results indicate that MSvDB cholinergic activity levels promote a network state characterized by theta activity. Similarly, slow gamma power was correlated with stimulation frequency in hippocampal subfields CA1, CA3 and DG (see Figure 3.9, $r = 0.72$ for CA1, $r = 0.85$ for CA3, and $r = 0.87$ for DG, $p < 0.05$ for CA1, and $p < 0.01$ for CA3 and DG, n = 6 mice, 4–6 trials per mouse). As for the analysis of theta peak power, two-way ANOVA for the corrected slow gamma power yielded statistically significant differences between stimulation frequencies, and hippocampal subfields ($F_{Stimulationfrequency(9,150)} = 3.32$, $p < 0.001$, $F_{Subfield(2,150)} = 5.05$, $p < 0.01$, $F_{Stimulationfrequency*Subfield(18,150)} = 0.55$, $p = 0.927$). The slow on- and offset of the cholinergic stimulation-induced theta oscillations suggest a G-protein coupled mechanism mediated by activation of muscarinic AChRs. Indeed, systemic application of atropine (50 mg/kg body weight), a competitive antagonist of the muscarinic AChR subtype, completely abolished the induction of theta rhythmic activity in hippocampal subfields CA1, CA3, and DG (see Figure 3.8, $p = 0.031$ for CA1, CA3, and DG, Wilcoxon signed-rank test, n = 6 mice with one value missing for CA1 at 40 Hz stimulation). However, stimulation induced increase in slow gamma power activity was not significantly changed in regions CA1, CA3, or DG (see Figure 3.9, $p = 0.054$, $p = 0.220$, and $p = 0.241$, respectively, paired t-test, n = 6 mice, 4–6 trials per mouse).

3.2. Interneuron and principal cell firing are differentially modulated by cholinergic MSvDB neurons

To assess how activation of cholinergic MSvDB neurons affects the activity of hippocampal neurons *in vivo*, we identified spikes from the high-pass filtered LFP signal and clustered the spikes into single units (see Materials and Methods). Having identified single units, I further aimed

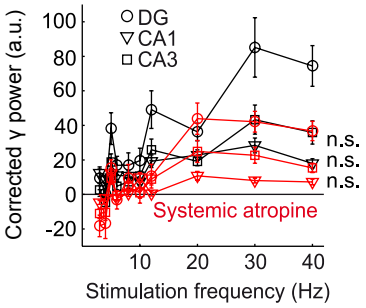

Figure 3.9 – Stimulation induced gamma band (26–48 Hz) power in hippocampal subfields CA1, CA3, and DG for different frequencies of light stimulation before versus after systemic atropine injection. Low gamma band power increases linearly with stimulation frequency (Pearson's correlation coefficient is 0.72 for CA1, 0.85 for CA3, and 0.87 for DG). Systemic administration of atropine (50 mg/kg body weight, i.p. injection) had no statistically significant effects on slow gamma power. n.s. = not significant, Wilcoxon signed-rank test. Symbols and error bars represent mean ± SEM of six mice.

at differentiate between putative interneurons and principal cells. Within the CA3 region, interneurons and principal cells have previously been shown to differ in the waveform properties of their extracellularly recorded spikes as well as in their burst firing behavior, and these two criteria have successfully been used to separate interneurons from principal cells (Csicsvari et al., 1998). The most prominent difference between CA3 interneurons and principal cells with respect to their spike waveform is the spike width, which I defined in this study as the distance in time from the peak of the spike to its first minimum (see left panels of Figure 3.10A, and Materials and Methods). Note, that the second classification parameter, namely the burst firing behavior of neurons, is reflected by a short latency peak in the autocorrelogram. I therefore determined the mean time of the spike autocorrelogram calculated in the range from 0–50 ms as a surrogate parameter for the burstiness of a single unit (see right panels of Figure 3.10A, and Materials and Methods), and plotted this parameter against the spike width of the same unit (see Figure 3.10B).

Using these parameters for classification, most of the recorded single units fell into one of two clearly distinguishable clusters (582/671 units from 42 mice) and hence could be classified as putative interneurons (n = 197 single units from 36 mice) or putative principal cells (n = 385 single units from 39 mice). Most interneurons showed an increased spiking rate during the time period of stimulation (62 % and 64 % for 12 Hz and 20 Hz stimulation, respectively), whereas the majority of principal neurons (73 % and 71 % for 12 Hz and 20 Hz stimulation, respectively) showed decreased spiking rates (see Figure 3.11A for a classified interneuron example (upper panel) and principal cell example (lower panel), and Figure 3.11B for the cumulative distribution function of spiking rate changes for both interneuron and principal cell populations).

Moreover, the mean spiking rate of the population of putative interneurons was significantly increased, whereas the mean spiking rate of the population of putative principal cells was significantly decreased upon stimulation of cholinergic MSvDB neurons (see Figure 3.12A for interneurons and Figure 3.13A for principal cells, $X^2_{(23,4704)} = 101.9$, $p < 0.0001$, and $X^2_{(23,9216)} = 323.7$, $p < 0.0001$, respectively, Kruskal-Wallis test). Accordingly, the mean normalized change of spiking

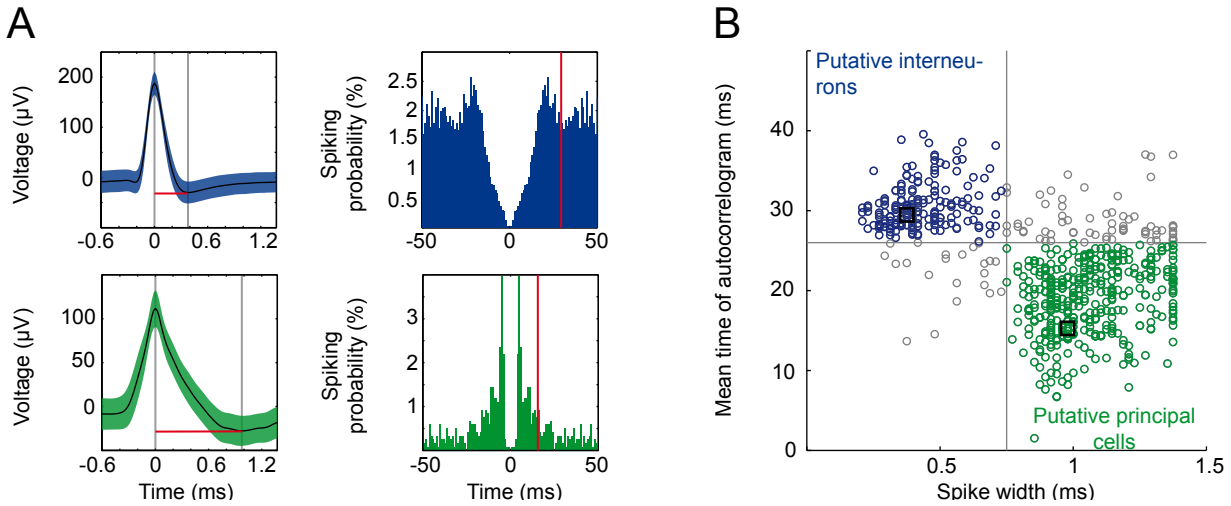

Figure 3.10 – Clustering of single units into putative interneurons and principal cells. A, Waveform (mean ± SD) and spike autocorrelogram of a single unit classified as a putative interneuron (upper panels), and a single unit classified as a putative principal cell (lower panels). Note that the two most distinctive characteristic features are the spike form and the form of the autocorrelogram, which reflects bursting behavior. Red lines in left panels indicate the spike width measured from the peak to the first minimum and red lines in right panels indicate the first moment (mean time) of the autocorrelogram. **B,** Clustering of cells into putative interneurons and principal cells based on the spike width and the mean time of the autocorrelogram, black squares mark the cells in A. Single units were recorded in area CA3 of the dorsal hippocampus from a total of 42 mice: 197 units from 36 mice were classified as putative interneurons, and 385 units from 39 mice were clustered as putative principal cells. 89 units were not assigned to either cell cluster.

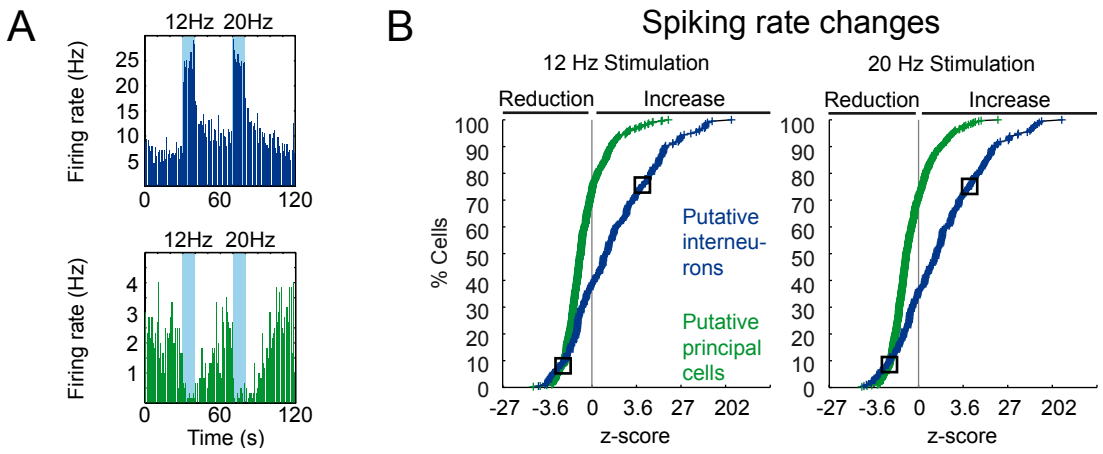

Figure 3.11 – Stimulation of ChAT$^+$ MSvDB neurons changes the firing rates of putative interneurons and principal cells in area CA3 of the dorsal hippocampus. A, Firing rate histograms of the putative interneuron (upper panel) and principal cell (lower panel) as shown in Figure 3.10A. Blue background indicates 10 s time intervals of light stimulation of cholinergic MSvDB neurons at 12 Hz or 20 Hz. **B,** Cumulative cell density plots of firing rate z-scores calculated for the 10 s period of stimulation at 12 Hz (left panel) and 20 Hz (right panel) for the single units classified as putative interneurons or principal cells (see Figure 3.10). Black squares mark cells in A.

rate in relation to baseline activity (measured as z-scores, see Materials and Methods) is increased for putative interneurons, but decreased for putative principal cells (see Figure 3.12B for interneurons and Figure 3.13B for principal cells, $X^2_{(23,4704)} = 128.2$, $p < 0.0001$, and $X^2_{(23,9216)} = 990.3$, $p < 0.0001$, respectively, Kruskal-Wallis test for difference between 0.5 s time bins). To visualize the change in spiking rates on a single cell level, I created false color plots reflecting the absolute spiking rates or the change in spiking rates in units of the standard deviation of the baseline period (z-scores) in 5 s time bins for the population of putative interneurons and principal cells (see Figures 3.12C and D, and Figures 3.13C and D, respectively).

To visualize the change of spiking rates on the population level, I plotted the distribution of spiking rates for the baseline and the cholinergic stimulation condition (see Figure 3.14A) for both putative interneurons and putative principal cells. Interestingly, the spiking rates of putative interneurons and putative principal cells follow a lognormal distribution, as previously described for cortical neurons in vivo (Buzsáki and Mizuseki, 2014). Since on the single cell level, the spiking rate changes induced by 12 Hz and 20 Hz stimulation did not differ much, I decided to average the spiking rate values across both stimulation conditions to finally compare the baseline condition with a condition of increased hippocampal cholinergic tone. The distributions of spiking rates are differentially effected by cholinergic stimulation for interneurons and principal cells. For interneurons, the left tail of the distribution disappears resulting in a decreased variance (on a

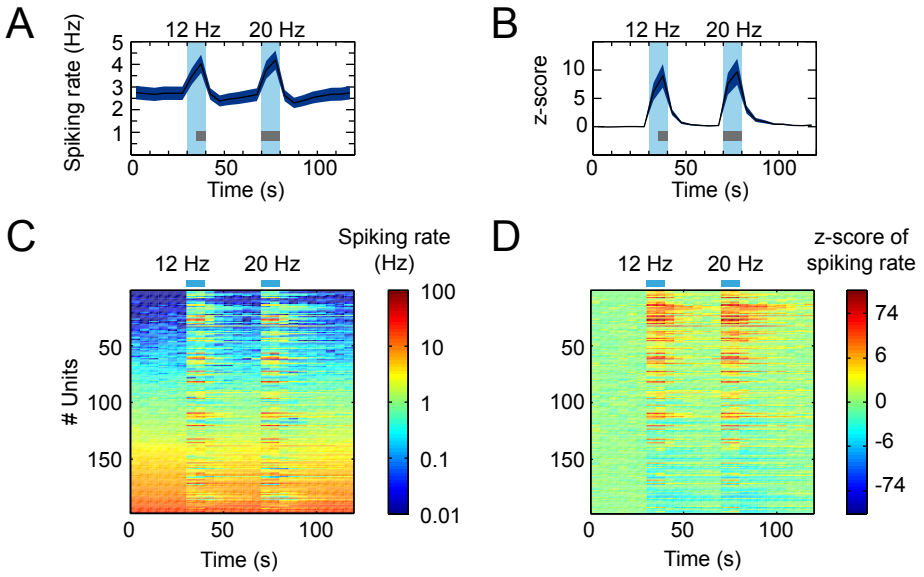

Figure 3.12 – Stimulation of ChAT$^+$ MSvDB neurons results in a net increase of interneuron firing in the hippocampal CA3 subfield. A,B, Mean ± SEM (indicated by blue area) of spiking rate (A) and z-scores of changes in spiking rate (B) for putative interneurons. Data points reflect 5 s time intervals. The mean spiking rate as well as the z-scores of changes in spiking rate increase during the time periods of stimulation at 12 Hz or 20 Hz. Blue backgrounds indicate time intervals of light stimulation, horizontal gray bars indicate $p < 0.05$ for the difference of spiking rate or z-score at the respective 5 s time interval from each value of the 5 s time intervals of the baseline period, Kruskal-Wallis test followed by Tukey-Kramer post hoc test. **C,D,** False color plots of spiking rates (C) and z-scores of changes in spiking rate (D) for each putative interneuron. Same units as in Figure 3.10B. Units are sorted according to their basal spiking rates.

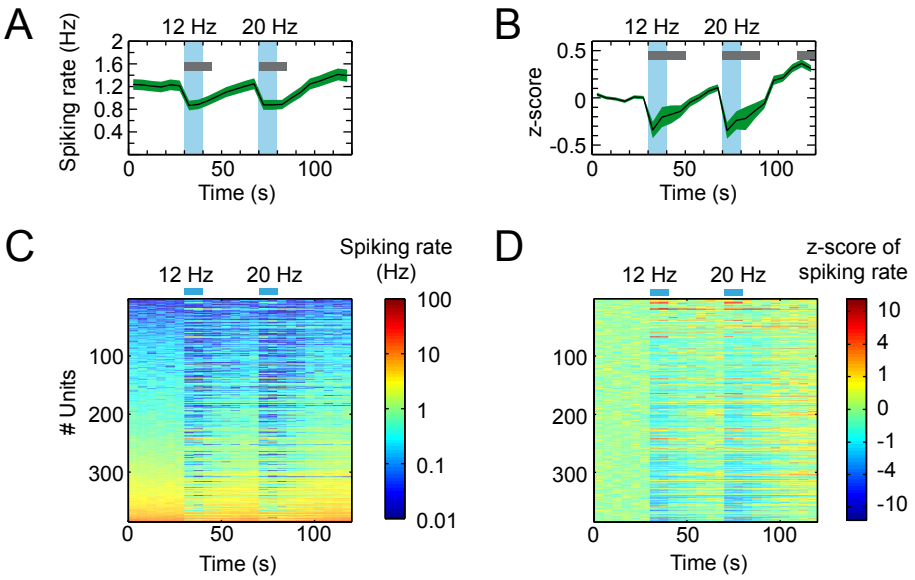

Figure 3.13 – Stimulation of ChAT$^+$ MSvDB neurons results in a net decrease of principal cell firing in the hippocampal CA3 subfield. A,B, Mean $\pm$ SEM (indicated by blue area) of spiking rate (A) and z-scores of changes in spiking rate (B) for putative principal neurons. Data points reflect 5 s time intervals. Putative principal cells show a prolonged decrease of spiking rate as well as z-scores of changes in spiking rate during and after cessation of stimulation at 12 Hz or 20 Hz. Blue backgrounds indicate time intervals of light stimulation, horizontal gray bars indicate $p < 0.05$ for difference of the spiking rate or z-score at the respective 5 s time interval from each value of the 5 s time intervals of the baseline period, Kruskal-Wallis test followed by Tukey-Kramer post hoc test. **C,D,** False color plots of spiking rates (C) and z-scores of changes in spiking rate (D) for each putative interneuron. Same units as in Figure 3.10B. Units are sorted according to their basal spiking rates.

logarithmic scale). For pincipal neurons, the opposite is true. But how are the spiking rates affected on a single cell level? Linear correlation of basal spiking rates with the spiking rates during cholinergic stimulation reveals that, for interneurons, the cells with relatively low basal spiking rates are recruited to the population of highly active cells, whereas the cells, which are already relatively active during the baseline condition, remain highly active during the cholinergic stimulation (Pearson's correlation coefficient is 0.52, $p < 0.0001$). A similar picture emerges for the putative principal cells: The subset of cells which show a relatively high basal spiking activity, remain relatively active during the condition of cholinergic stimulation, whereas the cells with relatively low basal spiking activity are almost completely silent during the condition of high cholinergic tone (Pearson's correlation coefficient is 0.63, $p < 0.0001$).

In a subset of recordings, I systemically applied atropine (50 mg/kg body weight, i.p. injection), which diminished the cholinergic modulation of the spiking rates of putative interneurons, while the spiking rate modulation of putative principal cells was not significantly altered (see Figure 3.15 for false color plots of z-scores reflecting the changes of spiking rate in relation to baseline activity for each unit and Figures 3.16A and B for the net effect on the population and putative interneurons or principal cells, respectively).

3.3. Stimulation induced hippocampal theta requires an intraseptal relay

Cholinergic MSvDB neurons give rise to septo-hippocampal projection fibers as well as intraseptal connections to GABAergic and glutamatergic MSvDB neurons. Both of these neuron types also provide projections to the cortex and hippocampus. Thus, it is conceivable that some effects of activating cholinergic MSvDB neurons might be mediated via an intraseptal relay. We assessed the relevance of such an indirect pathway for theta synchronization. We injected atropine (300 nl, 7.2 mM, see Materials and Methods) focally into the MSvDB while optogenetically stimulating cholinergic MSvDB neurons (see Figure 3.17A, lower panels for one example experiment). We used atropine because muscarinic ACh receptors play a major role in regulating septo-hippocampal GABAergic neurons (Alreja et al., 2000). Control animals were injected with ACSF (see Figure 3.17A, upper panels for one example experiment). Atropine, but not ACSF injection into the MSvDB, caused a complete block of optogenetically induced hippocampal theta oscillations (see Figure 3.17B for mean ± SEM of z-scores during 20 Hz stimulation). This effect was statistically significant for both 12 Hz and 20 Hz stimulation, as revealed by statistical analysis of the differences between the baseline corrected theta peak power values (see Figures 3.18A and B for 12 Hz and 20 Hz stimulation, respectively, * indicates significant difference between pre- and post-application conditions, $p < 0.05$, paired t-test, § indicates significant differences

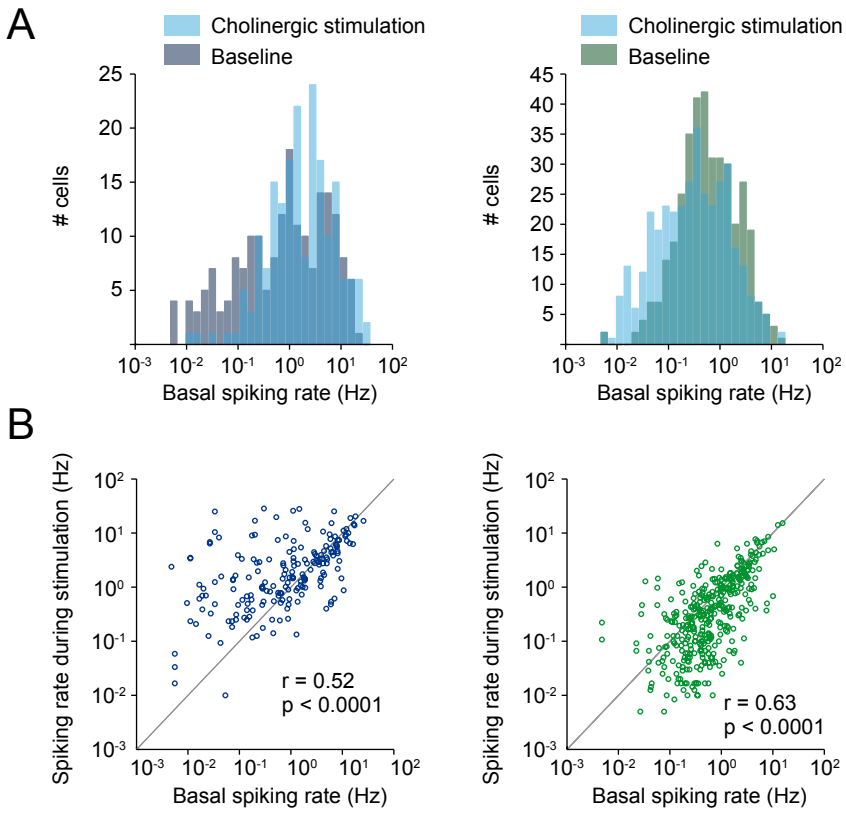

Figure 3.14 – Spiking rates of CA3 interneurons and principal cells follow a lognormal distribution and are correlated between brain states of low and high cholinergic tone. A, Distributions of spiking rates plotted on a logarithmic scale for putative interneurons (left panel) and putative principal cells (right panel) for baseline and cholinergic stimulation conditions (12 Hz and 20 Hz light stimulation conditions pooled). **B,** Correlation of spiking rates between the baseline and the cholinergic stimulation condition for putative interneurons (blue, left panel) and putative principal cells (green, right panel). Note that, during stimulation of cholinergic MSvDB neurons, interneurons with relatively low basal spiking rates are recruited into the subset of highly active interneurons. In contrast, principal neurons with relatively low basal spiking rates are almost completely silenced by the cholinergic stimulation. For both interneurons and principal cells, the cells belonging to the highly active subpopulation during the baseline condition also contribute to the subpopulation, which is highly active during cholinergic stimulation. n = 191 interneurons, and n = 370 principal neurons (units with zero spikes in either the baseline or the stimulation condition excluded for logarithmic scaling, otherwise same units as in Figure 3.10B), r = Pearson's correlation coefficient.

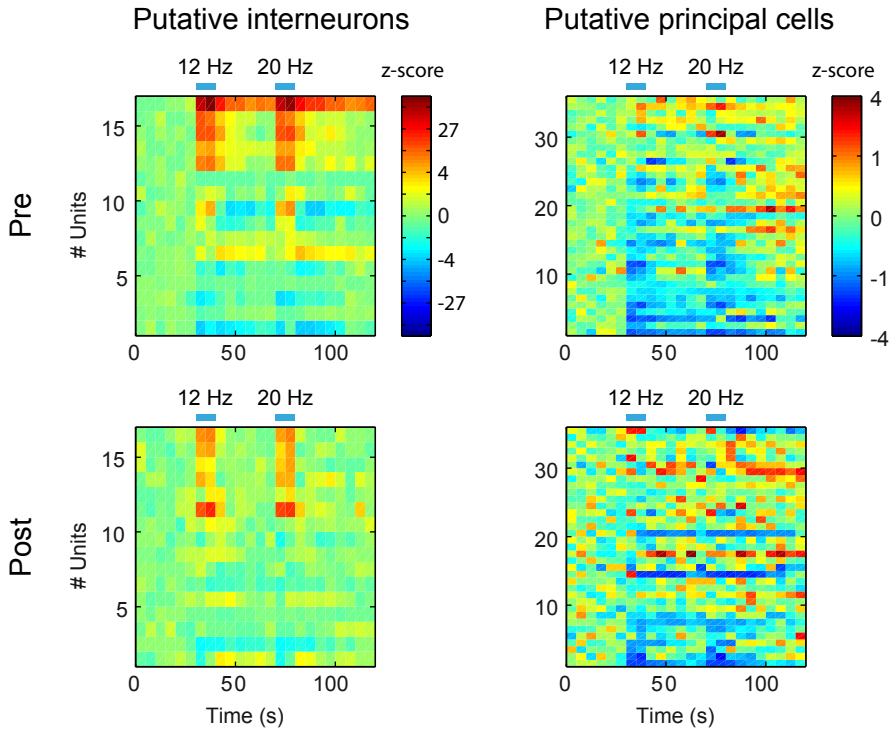

Figure 3.15 – Systemic application of atropine diminishes the cholinergic modulation of spiking rates of putative interneurons in area CA3 of the dorsal hippocampus. Color scale reflects z-scores of changes in spiking rate relative to baseline activity. Blue bars indicate stimulation of cholinergic MSvDB neurons at 12 Hz and 20 Hz. Time resolution is 5 s. Upper and lower panels show spiking rate modulation of cells before and after systemic application of atropine, respectively. Each line represents one cell, with the same line in upper and lower panels representing the same cell. Cells are ordered by the mean effect size across the pre and post drug condition for the time period of stimulation at 12 Hz. Left panels show putative interneurons, right panels show putative principal cells. n = 16 putative interneurons from six mice, and n = 35 putative principal cells from five mice, 3–6 trials per pre and post atropine injection condition and mouse, respectively.

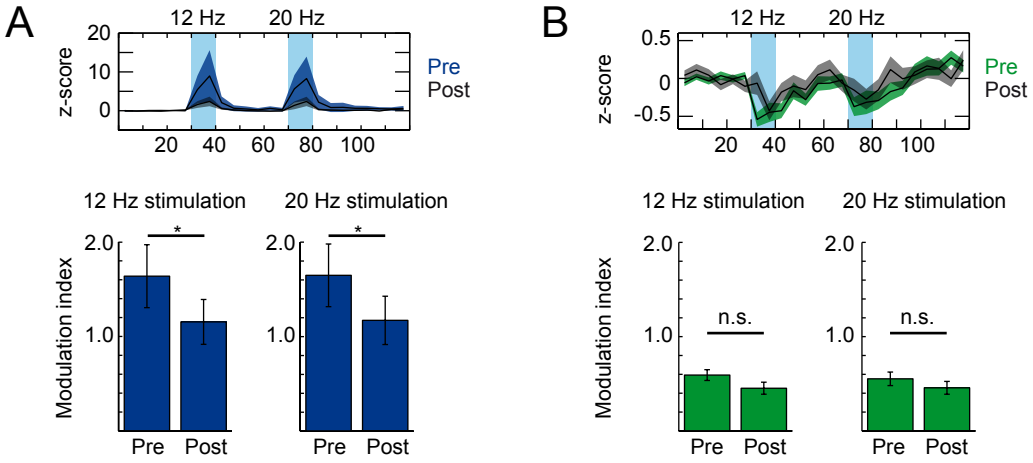

Figure 3.16 – Systemic application of atropine diminishes the net cholinergic modulation of spiking rate of the population of putative interneurons in area CA3 of the dorsal hippocampus. A, Upper panel shows mean ± SEM of z-scores of changes in spiking rate for putative interneurons before and after systemic atropine application (50 mg/kg body weight, i.p. injected). Line with dark blue surrounding area indicates mean ± SEM of z-scores before systemic atropine application, line with gray surrounding area indicates mean ± SEM of z-scores after systemic atropine application. Light blue area indicates time periods of light stimulation at 12 Hz or 20 Hz. Lower panel shows the modulation index pre vs. post systemic atropine application for both 12 Hz and 20 Hz stimulation (left and right panel, respectively). * indicates significant difference between the pre- and post-condition of systemic atropine application, $p < 0.05$, Wilcoxon signed-rank test, $n = 16$ putative interneurons from six mice. **B,** Equivalent to A, but for putative principal cells. n.s. = not significant, $n = 35$ principal neurons from five mice.

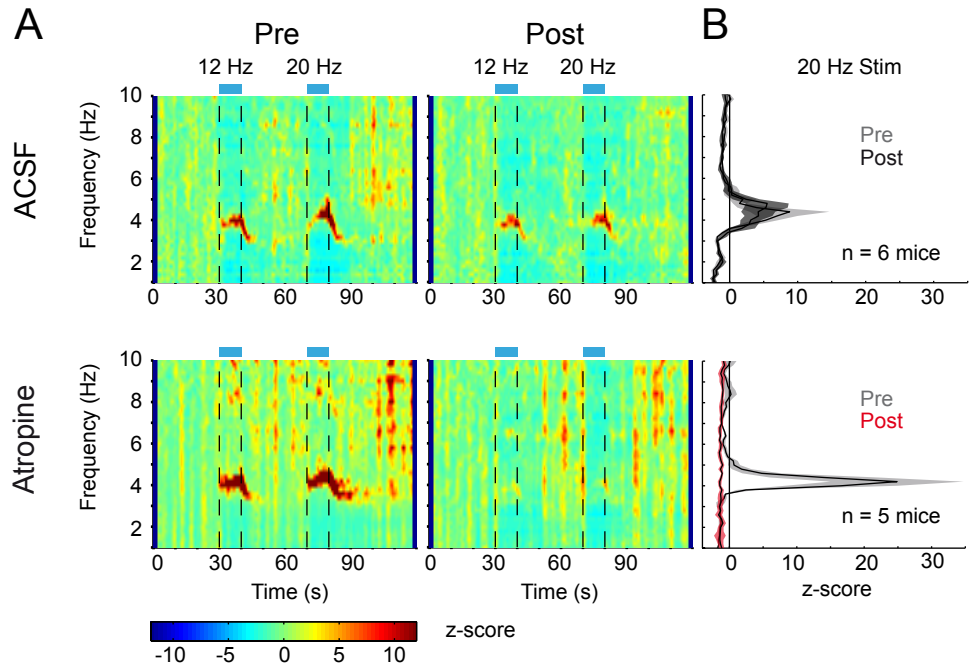

Figure 3.17 – Hippocampal theta rhythm induced by stimulation of MSvDB neurons requires an intraseptal relay. A, Time-frequency plots of power spectral density z-scores from LFPs recorded in hippocampal subfield CA1 during light stimulation of cholinergic MSvDB neurons for 10 s intervals at 12 Hz or 20 Hz stimulation (time intervals of stimulation indicated by blue bars and dashed lines). Upper panels show data for one representative animal for the pre- and post-condition (left and right panel, respectively) of local ACSF injection into the MSvDB. Lower panels show data for the pre- and post-condition (left and right panel, respectively) of local injection of the muscarinic antagonist atropine (7.2 mM) into the MSvDB of a different animal. **B,** Mean ± SEM of power spectral density z-scores averaged across the last 7.5 s of the 10 s time interval at 20 Hz stimulation for the pre- and post-conditions of local injection of ACSF (upper panel) or atropine (lower panel) into the MSvDB. n = 6 mice for ACSF injection, and n = 5 mice for atropine injection. Values for one mouse reflect mean across 3–7 trials.

between ACSF (n = 6 mice, 3–6 trials per condition and mouse) and atropine groups (n = 5mice, 4–7 trials per condition and mouse), $p < 0.05$, t-test). These results indicate that an intraseptal relay is mandatory for the generation of cholinergic theta oscillations in the hippocampus.

But is synaptic acetylcholine release by MSvDB projections to the hippocampus also important for hippocampal theta generation? We focally injected a blocker cocktail of muscarinic and nicotinic acetylcholine receptor antagonists, namely atropine (Atr, 7.2 mM), mecamylamine (Mec, 10 mM), and methyllycaconitine (MLA, 20 μM), Atr-Mec-MLA, see Materials and Methods) into the dorsal hippocampus close to the recording site (see Figure 3.19A for example experiments with ACh receptor blockers and ACSF injection). I chose to block both muscarinic and nicotinic ACh receptors, because in the hippocampus and dentate gyrus, most interneurons show strong

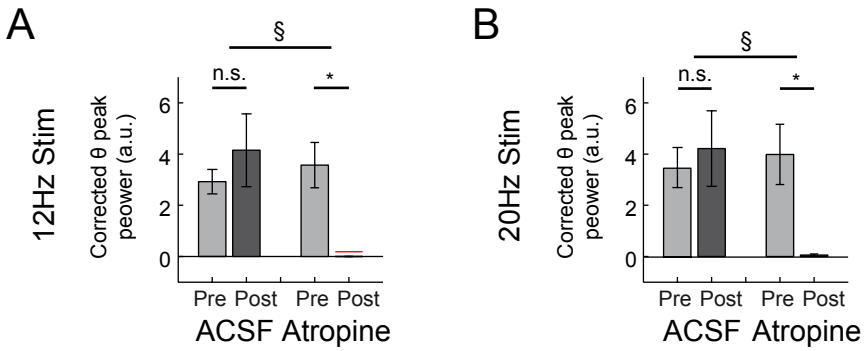

Figure 3.18 – Stimulation-induced theta synchronization is abolished after local atropine injection into the MSvDB. Mean ± SEM of the corrected theta peak power difference for 12 Hz stimulation (A) and 20 Hz stimulation (B) comparing pre- and post-conditions of ACSF- and atropine-injected groups (left- and right-handed, respectively). * indicates $p < 0.05$, paired t-test. § indicates $p < 0.05$, t-test, n.s. = not significant. $n = 6$ mice for ACSF injection, and $n = 5$ mice for atropine injection (same mice as in Figure 3.17), 3–6 and 4–6 trials for pre- and post-ACSF injection condition per mouse, respectively, and 5–7 and 4–5 trials for pre- and post-atropine injection condition per mouse, respectively.

excitation via nicotinic ACh receptors (Frazier et al., 1998, 2003; Ji and Dani, 2000; Jones and Yakel, 1997; McQuiston and Madison, 1999b). In most experiments, theta induction was strongly inhibited after blocker, but not after ACSF injection, as evaluated for hippocampal subfield CA1 (see Figure 3.19B for mean ± SEM of z-scores during 20 Hz stimulation and Figures 3.20A and B for the quantification of corrected theta peak power and the statistical analysis for 12 Hz and 20 Hz stimulation, respectively). However, this inhibition was more reliably observed for the 12 Hz stimulation condition than the 20 Hz stimulation condition, as revealed by significant differences for the 12 Hz stimulation condition, but non-significant effects for the 20 Hz stimulation condition (see Figures 3.20A and B, respectively, * indicates significant difference between pre- and post application conditions, $p < 0.05$, paired t-test, § indicates significant differences between the ACSF ($n = 3$ mice, 6–10 trials per condition and mouse) and Atr-Mec-MLA groups ($n = 5$ mice, 3–10 trials per condition and mouse), $p < 0.05$, t-test). After the start of the injection series for Atr-Mec-MLA, but not for ACSF, average stimulation-evoked theta power showed an incremental reduction. Fitting a sigmoidal curve to the data points revealed that 50 % of the initial effect size was reached after 23.1 min or 26.1 min for 12 Hz or 20 Hz stimulation conditions, respectively (see Figures 3.21A and B for control injections with ACSF and injection of the cholinergic blocker cocktail Atr-Mec-MLA into the dorsal hippocampus, respectively). This is consistent with a local effect of these blockers, although we cannot exclude that blockers may spread to more distant brain regions at later stages.

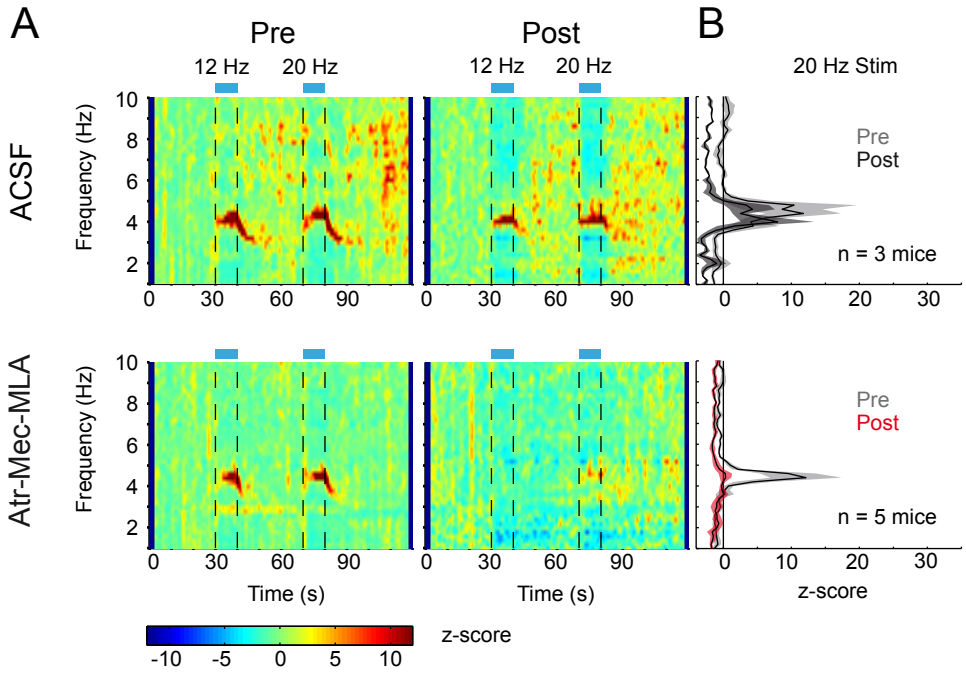

Figure 3.19 – Time-frequency analysis of hippocampal power spectral density before and after focal injections into the dorsal hippocampus. A, Upper panels show data for one representative animal for the pre- and post-condition (left and right panel, respectively) of local ACSF injection into the MSvDB. Lower panels show data for the pre- and post-condition (left and right panel, respectively) of local injection of a cholinergic blocker cocktail containing atropine (Atr, 7.2 mM), mecamylamine (Mec, 10 mM), and methyllycaconitine (MLA, 20 μM) into the dorsal hippocampus of a different animal. **B,** Mean $\pm$ SEM of power spectral density z-scores averaged across the last 7.5 s of the 10 s time interval at 20 Hz stimulation for the pre- and post-conditions of local injection of ACSF (upper panel) or blocker cocktail Atr-Mec-MLA (lower panel) into the dorsal hippocampus. n = 3 mice for ACSF injection, and n = 5 mice for Atr-Mec-MLA injection. Values for one mouse reflect mean across 3–10 trials.

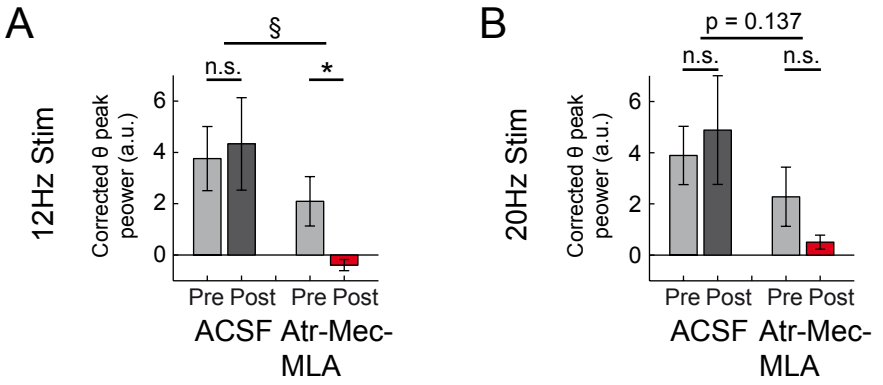

Figure 3.20 – Stimulation-induced theta synchronization is diminished after local injection of nicotinic and muscarinic blockers into the dorsal hippocampus. Mean ± SEM of the corrected theta peak power difference for 12 Hz stimulation (A) and 20 Hz stimulation (B) comparing pre and post conditions of ACSF- and Atr-Mec-MLA blocker cocktail-injected groups (left- and right-handed, respectively, blocker cocktail consists of atropine, 7.2 mM, mecamylamine, 10 mM, and methyllycaconitine, 20 μM. * indicates $p < 0.05$, paired t-test. § indicates $p < 0.05$, t-test, n.s. = not significant. n = 3 mice for ACSF injection, and n = 5 mice for atropine injection (same mice as in Figure 3.19), 6 and 9–10 trials per pre- and post-ACSF injection condition per mouse, respectively, and 3–7 and 5–10 trials per pre- and post-Atr-Mec-MLA injection condition, respectively.

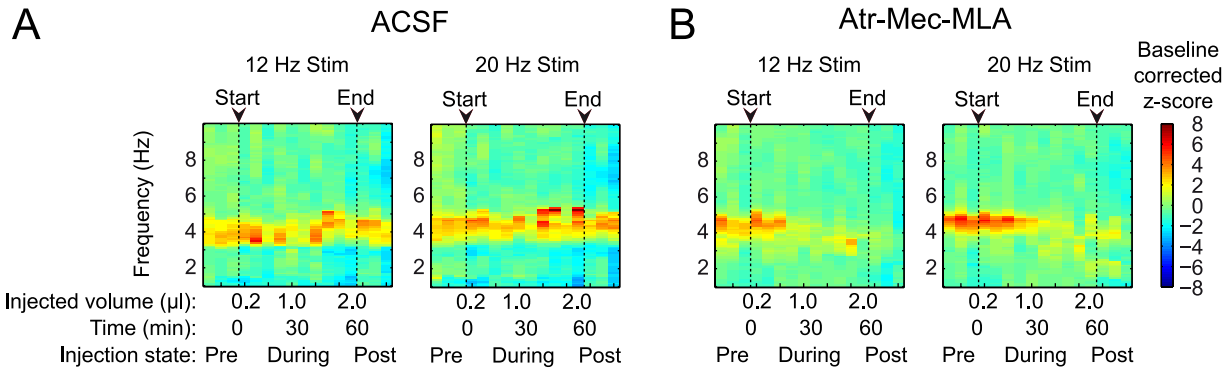

Figure 3.21 – Time course of the reduction of stimulation-induced theta oscillations in hippocampal subfield CA1 during local microinjections of muscarinic and nicotinic AChR antagonists into the dorsal hippocampus. A, ACSF injection has no biologically significant effect on stimulation-induced theta activity both for 12 Hz and 20 Hz stimulation conditions (left and right panel, respectively). **B,** Injection of the cholinergic blocker cocktail Atr-Mec-MLA diminishes stimulation-induced theta oscillations with 50 % reduction after 23.1 min or 26.1 min after start of the injection series for stimulations at 12 Hz or 20 Hz, respectively. Colored tiles represent mean of baseline corrected z-scores of power change per frequency bin (see Materials and Methods) for each trial recorded before, during, and after a series of 10 microinjections, applied every 5–6 min with 0.2 μl injection volume each, into the dorsal hippocampus, n = 3 mice for ACSF injected group, and n = 5 mice for Atr-Mec-MLA injected group. Arrowheads indicate the start and end of the injection series.

Table 3.1 – Electrophysiological characteristics of genetically identified PV^+ and $ChAT^+$ MSvDB neurons

Properties		PV^+	$ChAT^+$	p-value
Passive	V_m (mV)	-79.7 ± 1.7	-83.2 ± 4.6	0.0360
	R_{inp} (MΩ)	194.7 ± 104.9	279.9 ± 188.8	0.2231
	τ_{mem} (ms)	12.7 ± 5.7	18.5 ± 14.4	0.2529
Active	AP_{thr} (mV)	-53.7 ± 8.2	-51.1 ± 4.9	0.4127
	AP_{ampl} (mV)	69.8 ± 11.8	62.3 ± 6.7	0.0923
	$AP_{dV/dt}$ (mV/ms)	318.5 ± 110.3	133.8 ± 63.3	0.0002
	$AP_{Half\text{-}width}$ (ms)	0.31 ± 0.08[1]	0.96 ± 0.23	$7x10^{-7}$
	fAHP (mV)	-16.6 ± 6.0	-10.1 ± 5.8	0.0202

[1]One outlier assessed by applying Chauvenet's criterion excluded.

Comparison of passive and active properties of PV^+ (n = 10) and $ChAT^+$ (n = 11) MSvDB neurons, identified by genetically targeted eYFP expression. V_m = Resting membrane potential, R_{inp} = Input resistance, τ_{mem} = Membrane time constant, AP_{thr} = Action potential threshold, AP_{ampl} = Action potential amplitude, $AP_{dV/dt}$ = Maximal action potential rise slope, $AP_{Half\text{-}width}$ = Action potential width at half maximal amplitude, fAHP = Fast afterhyperpolarization. Values represent mean ± SD. p-values (t-test) indicate statistical difference between PV^+ and $ChAT^+$ neurons.

Our findings demonstrate that both hippocampal and septal ACh is required for proper induction of theta oscillations. In particular, the requirement for intraseptal ACh suggests that intraseptal connectivity is essential for mediating hippocampal theta induction. We therefore examined the effects of cholinergic neuron activation on other types of septal neurons. We first characterized genetically identified $ChAT^+$ and PV^+ GABAergic neurons in the slice preparation (see Materials and Methods), and characterized their passive and active electrophysiological properties (see Table 3.1).

PV^+ neurons were characterized by narrow action potentials with a fast upstroke and prominent fAHPs (see Figure 3.22A). These characteristics set them apart from $ChAT^+$ neurons (see Figure 3.22B).

Subsequently, we activated cholinergic neurons optogenetically in septal slices and recorded from non-ChR2 expressing medial septal neurons. Non-ChR2-expressing neurons were classified into putative PV^+ and other neurons, based on their functional properties. Whereas a single light stimulation pulse elicited only small effects in non-PV^+ neurons, it caused a slow depolarization in putative PV^+ neurons (see Figure 3.23A, upper and lower traces, respectively, for example

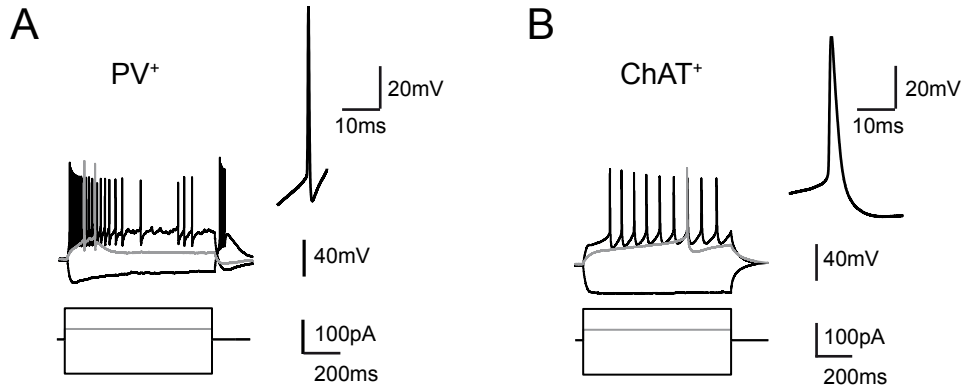

Figure 3.22 – Electrophysiological characterization of genetically identified PV$^+$ and ChAT$^+$ MSvDB neurons. Representative recordings from MSvDB neurons identified by ChR2-eYFP fluorescence in hippocampal slices obtained from PV-Cre (A) or ChAT-Cre (B) transgenic mice virally transduced by stereotactic injection into the MSvDB. Upper and lower traces correspond to voltage recordings and current injections, respectively. Grey traces correspond to threshold current injections. Insets show the first action potential generated within 50 ms of onset of current injection and depict the typical properties of these two cell types (see also Table 3.1). Patch-clamp recordings performed by Milan Pabst.

recordings, Figure 3.23B for mean ± SEM for membrane depolarization in 0.5 s time bins averaged across neurons, and Figure 3.23C for quantification of mean amplitude and area under the curve of the membrane depolarization within 2.5 s after stimulation, */** indicate significant difference, *$p < 0.05$, **$p < 0.01$, t-test, n = 9 and 19 for PV$^+$ and non-PV$^+$ neurons, respectively). Five second stimulus trains reliably elicited longer-lasting slow depolarizations in both neuron types (see Figure 3.24A for example recordings) that were significantly larger in putative PV$^+$ neurons (see Figures 3.24B and C, * indicates significant difference, *$p < 0.05$, t-test, n = 10 and n = 16 for PV$^+$ and non-PV$^+$ neurons, respectively). These results suggest that PV$^+$ septal neurons may be recruited by cholinergic activation, and play a role in driving hippocampal theta rhythms.

We additionally recorded from five putative PV$^+$ neurons using 10 s trains of stimulation at 12 Hz or 20 Hz—the same protocol as used for the *in vivo* experiments—and observed a depolarization in four out of five neurons. One cell showed a mild hyperpolarization in response to light-stimulation. Notably, the observed depolarizations lasted over the full 10 s time interval of the stimulus train (see Figure 3.25, only the four cells showing a depolarization are shown).

Of the 15 putative PV$^+$ neurons, seven were depolarized sufficiently to generate action potentials during light-stimulation, with the time at which action potentials occurred being very variable. These results suggest that PV$^+$ septal neurons may be recruited by cholinergic activation, and play a role in driving hippocampal theta rhythms. Indeed, PV$^+$ MSvDB neurons selectively innervate hippocampal interneurons and have long been suggested to be important for hippocampal theta rhythmicity via disinhibition of principal cells (Freund and Antal, 1988;

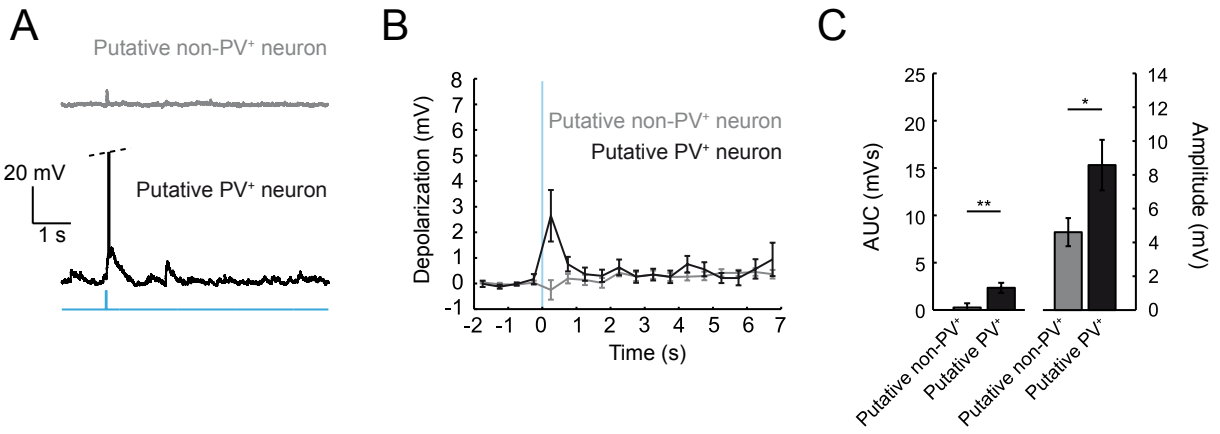

Figure 3.23 – Cholinergic MSvDB neurons activate putative PV$^+$ MSvDB neurons. A, Representative recordings from a putative PV$^+$ and non-PV$^+$ MSvDB neuron in acute coronal slices during optogenetic activation of cholinergic neurons and fibers using a single 20 ms laser pulse. **B,** Quantification of the average depolarization after stimulation. Average voltage in 0.5 s time bins is plotted. Blue line indicates single pulse light stimulation. **C,** The area under the curve (left y-axis) and amplitude (right y-axis) of the light-evoked depolarizations within 2.5 s evoked by single stimulation, data represent mean ± SEM, *p $<$ 0.05, **p $<$ 0.01, t-test, n = 9 and 19 for putative PV$^+$ and non-PV$^+$ neurons, respectively.

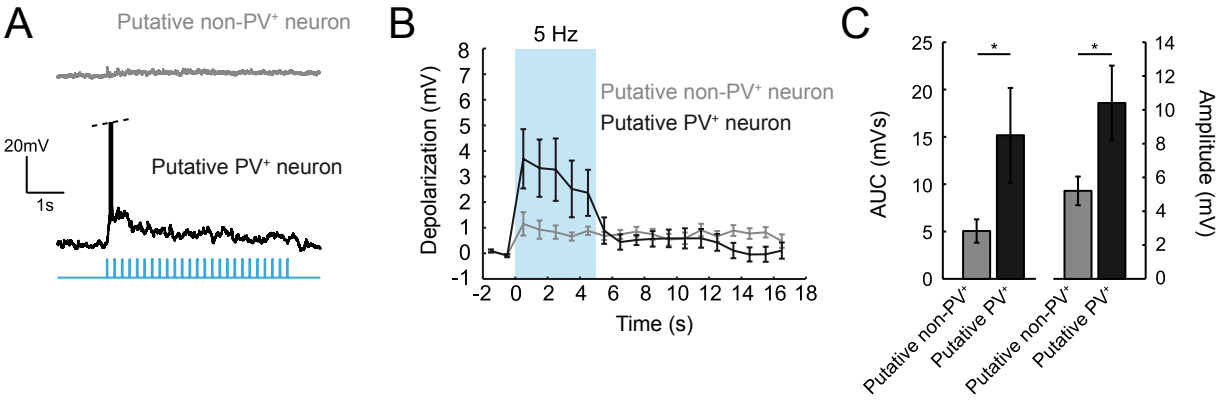

Figure 3.24 – Activity of cholinergic MSvDB neurons depolarizes putative PV$^+$ MSvDB neurons. A Representative recordings from putative PV$^+$ and non-PV$^+$ MSvDB neurons in acute coronal slices during optogenetic activation of cholinergic neurons and fibers using a 5 s stimulus train at 5 Hz. **B,** Quantification of the average depolarization after stimulation. Average voltage in 1 s time bins is plotted. Blue background indicates period of light stimulation train at 5 Hz. **C,** The area under the curve (left y-axis) and amplitude (right y-axis) of the light-evoked depolarizations within 5 s evoked by a 5 Hz stimulus train, data represent mean ± SEM, *p $<$ 0.05, n = 10 and 16 for putative PV$^+$ and non-PV$^+$ neurons, respectively.

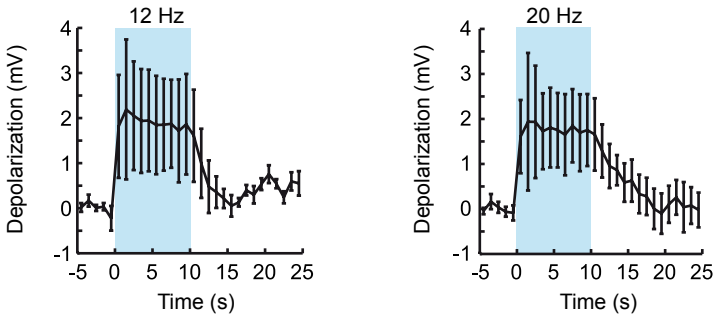

Figure 3.25 – Sustained activity of cholinergic MSvDB neurons results in long-lasting depolarizations of putative PV$^+$ MSvDB neurons. Light-evoked depolarizations lasted over the full 10 s time interval of the same stimulus train used in the *in vivo* experiments, left and right panels show data for stimulus trains at 12 Hz and 20 Hz, respectively. Data are presented as mean ± SEM of four (out of five) recorded cells showing an initial depolarization.

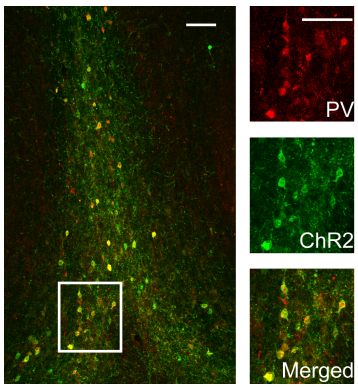

Figure 3.26 – ChR2-eYFP expression in PV$^+$ MSvDB neurons after injection of a Cre-dependent rAAV into the MSvDB of PV-Cre mice. Left panel shows a lower magnification photograph of the transduced MSvDB area. Right panels show the marked area at a higher magnification. Red color indicates Cy3-fluorescence after immunolabeling for PV, green color indicates FITC- and eYFP-fluorescence after immunolabeling for ChR2-eYFP. Merging of colors reveals that expression of ChR2-eYFP is restricted to PV$^+$ neurons. Photographs show the maximum intensity projection of 20 confocal z-stack images across 38 μm. Scale bars are 100 μm.

Hangya et al., 2009; Serafin et al., 1996; Tóth et al., 1997). Following expression of ChR2 in PV$^+$ septal neurons using rAAV-mediated gene transfer (see Figure 3.26), brief light pulses resulted in reliable stimulation of these neurons, even during long stimulus trains of ten seconds (spiking reliability per stimulus pulse of 1 for frequencies up to 20 Hz, and reliabilities of 0.92 ± 0.09 and 0.45 ± 0.43 for 30 Hz and 40 Hz, respectively, mean ± SD of n = 4 cells, see Figure 3.27).

We carried out *in vivo* light stimulation of PV$^+$ GABAergic neurons in the MSvDB and simultaneously recorded with a silicon probe in the hippocampus (n = 5 mice). Optogenetic stimulation of PV$^+$ MSvDB neurons caused a recruitment of hippocampal rhythmicity at precisely the septal stimulation frequency (see Figure 3.28 for raw traces, and Figures 3.29A and B for visualization of stimulation-induced changes of hippocampal oscillations). Remarkably, the spectral power of the oscillatory activity showed a clear frequency dependence (Kruskal-Wallis test, $X^2_{(9,40)} = 36.6$, $p < 0.0001$ for CA1, $X^2_{(9,40)} = 21.6$, $p < 0.05$ for CA3, and $X^2_{(9,40)} = 33.6$, $p < 0.001$ for DG). There was a maximum within all subregions at 10 Hz stimulation frequency, indicating a preferred frequency of the MSvDB-hippocampal network oscillation (see Figure 3.29C).

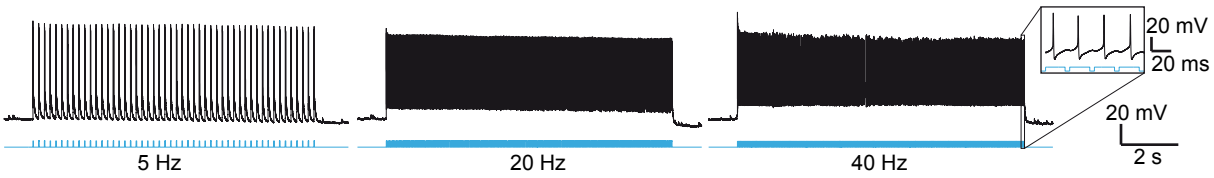

Figure 3.27 – *In vitro* entrainment of a PV$^+$-ChR2$^+$ MSvDB neuron evoked by repetitive 473 nm light stimulation of neuronal somata with 20 ms light pulses. Panels show voltage responses to 5 Hz, 20 Hz, and 40 Hz stimulation frequencies of one example cell, which is entrained by light stimulation to reliably elicit action potentials up to a frequency of 40 Hz. Patch-clamp recordings performed by Oliver Braganza.

The precise pacing of hippocampal rhythmicity by rhythmic light-stimulation of PV$^+$ MSvDB neurons is in sharp contrast to the effect on hippocampal oscillations observed when stimulating ChAT$^+$ MSvDB neurons, which I showed to induce theta and slow gamma oscillations independent from the frequency of septal stimulation (compare power spectral change during 12 Hz stimulation of PV$^+$ MSvDB neurons shown in Figure 3.30 with power spectral change during the same stimulation carried out in ChAT-Cre mice as depicted in Figure 3.6). Furthermore, this recruitment of rhythmic activity—in contrast to cholinergic stimulation-induced theta and slow gamma activity—was also precise in time, i.e. rhythmic activity started without a delay and declined immediately after cessation of light stimulation of PV$^+$ GABAergic MSvDB neurons (see Figure 3.31 for an example recording of one mouse). Stimulation effects on LFP power were very similar in hippocampal subfields CA1, CA3, and DG.

As light stimulation might cause light artifacts at some silicon probes, I addressed the possible impact of light artifacts experimentally by recording LFP signals during light stimulation using the same silicon probe in rAAV-injected wild type, ChAT-Cre, and PV-Cre mice. Light stimulation at 12 Hz or 20 Hz had no effect on LFP signals in the wild type mouse, whereas light stimulation in the ChAT-Cre mouse resulted in the characteristic occurrence of theta oscillations (with concomitant suppression of adjacent frequency bands) and slow gamma oscillations, and light stimulation carried out in the PV-Cre mouse resulted in oscillations at the respective stimulation frequency (see Figure 3.32 for power spectra of LFP signals recorded during baseline or the 10 s time period of light stimulation at 12 Hz).

There is also a peak at the stimulation frequency in the power spectrum of ChAT-Cre mice, which is completely absent in the wild type mouse. However, this peak is of much smaller amplitude than the one recorded in the PV-Cre mouse (note the logarithmic scaling and compare also Figures 3.6 and 3.30 for the mean ± SEM of power spectral density across eleven and five mice, respectively).

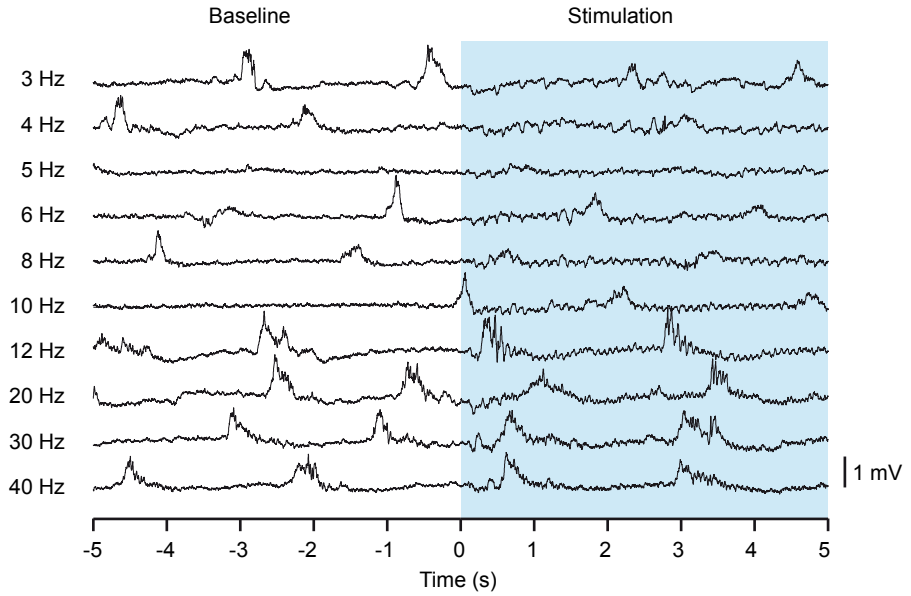

Figure 3.28 – Raw traces of hippocampal field potentials recorded in stratum radiatum of CA1 depicting the oscillatory change upon the onset of light-stimulation of PV$^+$ MSvDB neurons. Each line represents data for one of the different stimulation frequencies ranging from 3–40 Hz. Blue area indicates the time period of stimulation with the zero time point indicating the onset of the stimulation train.

3.4. Modulation of hippocampal neuronal activity by cholinergic MSvDB neurons is mediated by direct septo-hippocampal projections

We next assessed how relevant direct vs. indirect MSvDB projections to the hippocampus are for the observed increase of interneuron activity and concomitant inhibition of principal neuron activity in the CA3 subfield of the dorsal hippocampus. We measured how optogenetic stimulation of ChAT$^+$ MSvDB neurons modulates the firing rate of hippocampal neurons in animals which received either focal injections of atropine into the MSvDB or focal injections of the cholinergic blocker cocktail Atr-Mec-MLA into the hippocampus. As before, ACSF injected animals were used as controls. In a first step, I analyzed the effects of focal application of cholinergic blockers on the basal spiking rates of putative interneurons and principal cells. Injection of cholinergic blockers into the MSvDB did not affect basal firing rates of interneurons or pyramidal neurons (see Figure 3.33A). In contrast, hippocampal injections led to a reduction of basal spiking activity of interneurons and a concomitant increase of basal spiking activity of pyramidal cells (see Figure 3.33B). These changes in basal spiking rates become even more evident, when compared to the ACSF control injections. Importantly, the increase in basal spiking rate of principal neurons

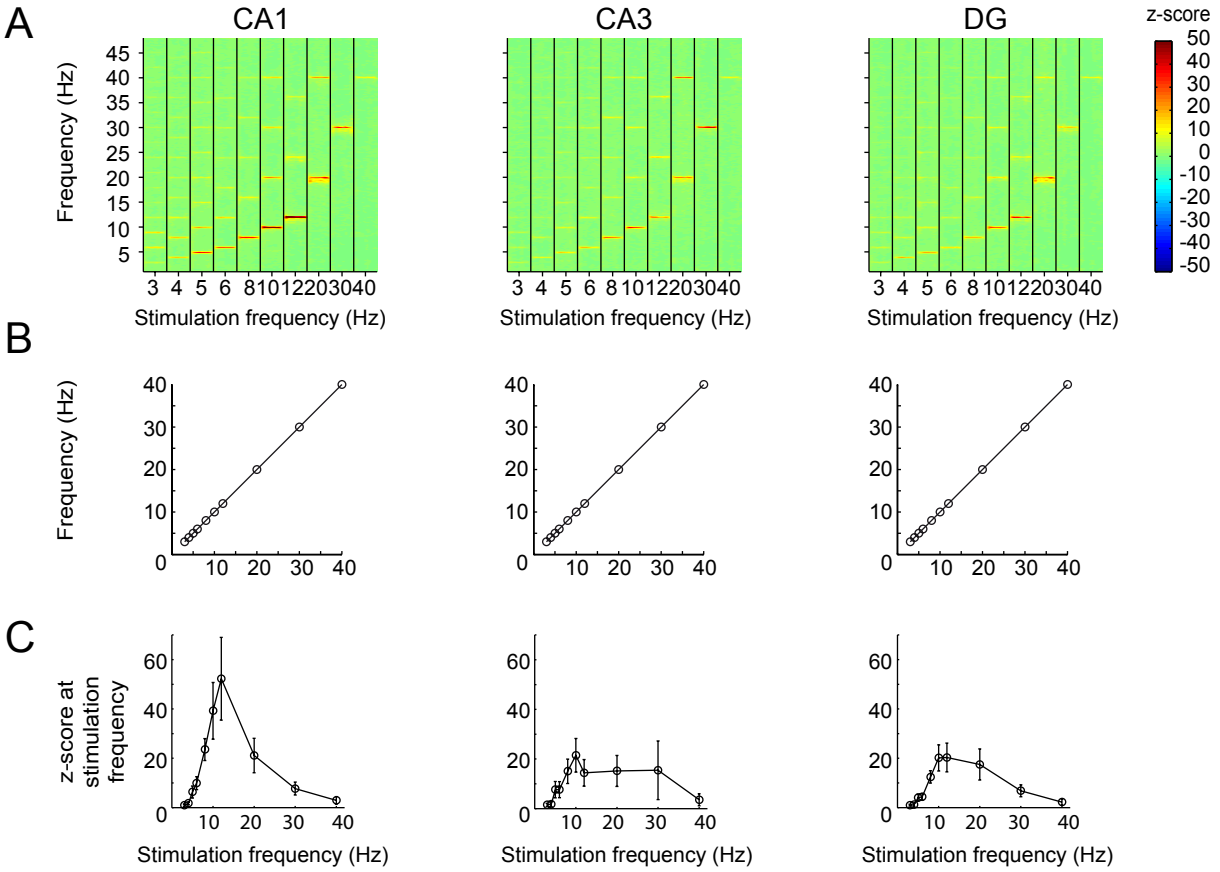

Figure 3.29 – Stimulation of PV$^+$ MSvDB neurons induces hippocampal oscillations at frequencies, which precisely match the septal stimulus frequencies. A, Time frequency plots of power spectral density z-scores of local field potentials recorded *in vivo* during light stimulation of PV$^+$-ChR2$^+$ MSvDB neurons. Columns show 10 s time intervals of different stimulation frequencies in the range of 3–40 Hz. Plots show mean values for hippocampal subfields CA1, CA3, and DG of n = 5 animals with 1–9 trials (median = 6) per mouse and stimulation condition. **B,** Panels show stimulation-induced peak power frequencies for hippocampal subfields CA1, CA3, and DG (from left to right). Data points represent the mean of five animals with zero variance. **C,** Z-scores reflecting the local field potential power change at the frequency of stimulation during the time of stimulation for the different stimulation frequencies. Note that there is a maximum at 10 Hz for hippocampal subfields CA1, CA3, and DG. Data represent mean ± SEM across n = 5 animals.

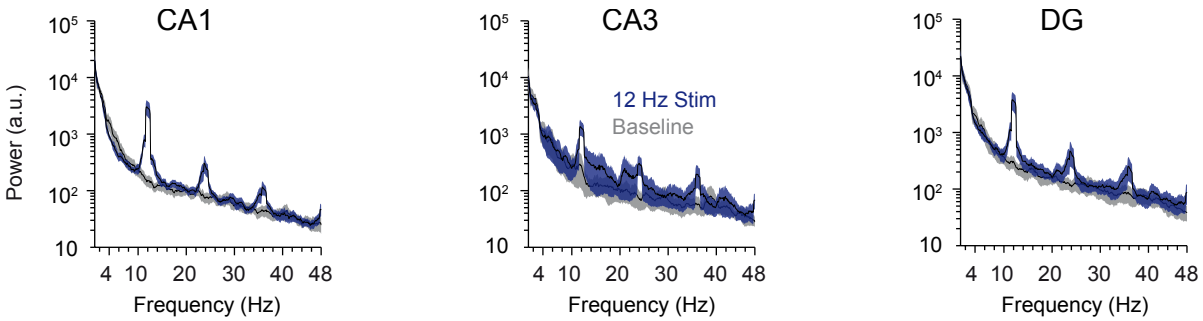

Figure 3.30 – PV$^+$ MSvDB neurons are able to recruit hippocampal ensembles with high temporal precision. Power spectra for hippocampal subfields CA1, CA3, and DG during the 10 s time interval of stimulation at 12 Hz (traces with blue shading) in comparison to a 10 s baseline period (traces with gray shading). Black lines and shading area represent mean ± SEM, respectively, of n = 5 mice, 7–9 trials per mouse.

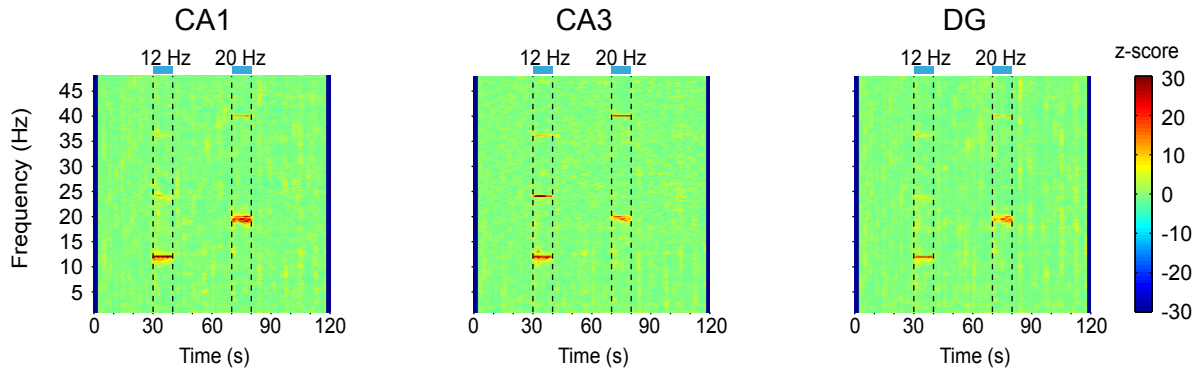

Figure 3.31 – Recruitment of hippocampal rhythmicity by light-stimulation of PV$^+$ MSvDB neurons has a fast on- and offset. Panels show time-frequency plots of power spectral density z-scores from local field potentials recorded in hippocampal subfields CA1, CA3, and DG (from left to right) during light-stimulation for 10 s intervals at 12 Hz or 20 Hz. The clearly visible harmonics indicate that the stimulation-induced hippocampal oscillations differ from a purely sinusoidal waveform.

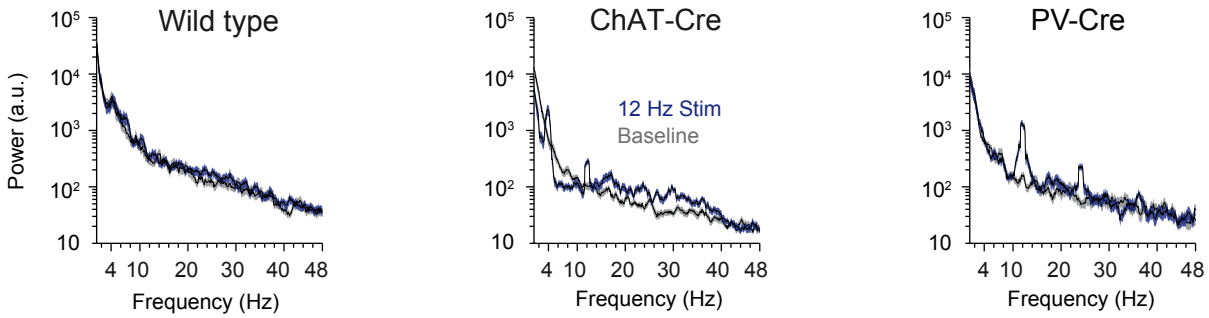

Figure 3.32 – Light artifacts do not contribute to the highly precise synchronization of hippocampal oscillations observed during light stimulation of PV$^+$ GABAergic MSvDB neurons. Power spectral densities of 10 s baseline activity (traces with gray shading) or 10 s light stimulation at 12 Hz (traces with blue shading) are shown for a wild type mouse (left panel), a ChAT-Cre mouse (middle panel), and a PV-cre mouse (right panel). The ChAT-Cre and PV-Cre mice expressed ChR2-eYFP in ChAT$^+$ cholinergic and PV$^+$ GABAergic MSvDB neurons, respectively. Importantly, LFP signals were obtained using the same silicon probe for all three mice. Black lines and colored shading represent mean ± SEM across three trials for the PV-Cre mouse, and across five trials for the ChAT-Cre and WT mice.

observed after focal injection of Atr-Mec-MLA into the dorsal hippocampus was much higher (2.2 fold increase) than the slight increase observed in the ACSF control conditions of both focal hippocampal and MSvDB injections (1.2 and 1.3 fold increase, respectively). Similarly to principal neurons, interneurons of the ACSF control condition for the focal hippocampal injections also showed a slight increase in basal spiking activity. This is in line with a general increase of hippocampal network activity, when the depth of anesthesia decreases gradually.

In a second step, I studied the effects of focal cholinergic blocker injection on the spiking rate modulation of hippocampal neurons (see Figures 3.34 and 3.35 for changes in spiking rate modulation after focal ACSF control injections or focal injections of atropine into the MSvDB, and Figures 3.36 and 3.37 for changes in spiking rate modulation after ACSF control injections or focal injections of Atr-Mec-MLA into the dorsal hippocampus.)

To quantify the effect on population spiking rate, we calculated a modulation index (see Materials and Methods) of single unit spiking rate modulation for each unit (see Figures 3.38A and B for putative CA3 interneurons and principal cells, respectively). This allows quantifying the effect of ACSF control or blocker injection at the population level via calculation of the delta modulation index, i.e. the difference between the modulation indices pre and post injection for each cell (see Figure 3.38C and D for putative CA3 interneurons and principal cells, respectively). Thus, at the population level, a mean delta modulation index of zero means no change in spiking rate modulation, whereas a negative mean delta modulation index indicates a decrease of spiking rate modulation. For statistical analysis of the differences in spiking rate modulation after

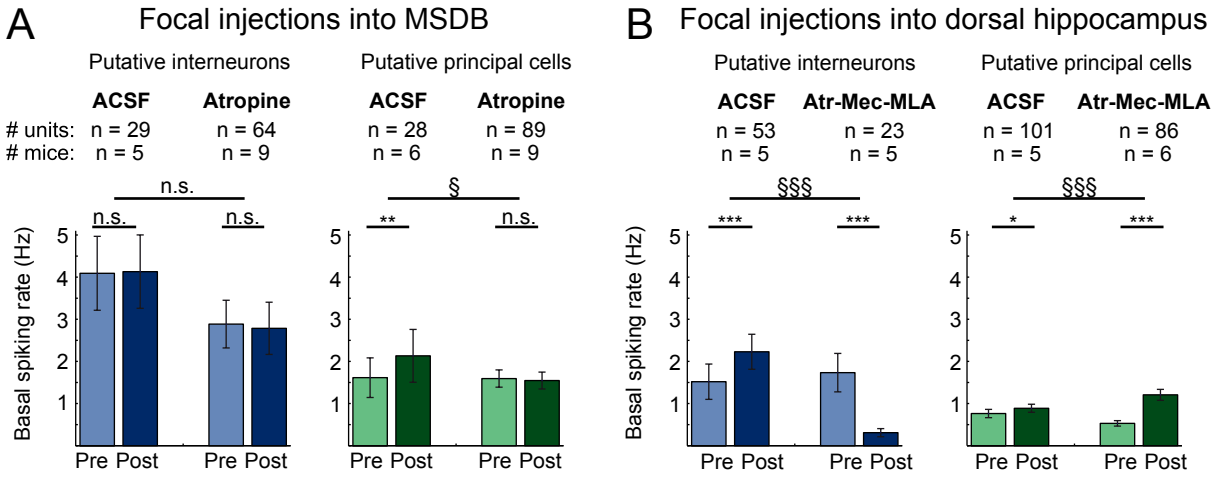

Figure 3.33 – Effects of local cholinergic blocker injections on basal spiking rates of hippocampal CA3 neurons. A, Focal injections of ACSF or atropine into the MSvDB did not affect basal spiking rates of hippocampal putative interneurons (left panel). For putative principal cells (right panel), basal spiking rates were not affected by atropine, and even slightly increased after ACSF injection. **B,** In contrast, focal injections of the cholinergic blocker cocktail Atr-Mec-MLA strongly reduced basal spiking rates of putative interneurons (left panel), but strongly increased basal spiking rates of putative principal cells (right panel). ACSF injections only slightly increased basal spiking rates for both putative interneurons and principal cells. n.s. = not significant, *p < 0.05, **p < 0.01, ***p < 0.001, Wilcoxon signed-rank test for comparison between pre and post application conditions; § p < 0.05, §§§ p < 0.001, Mann-Whitney U test for comparison between groups. See figure panels for numbers of analyzed units and mice, 3–10 trials per condition and mouse.

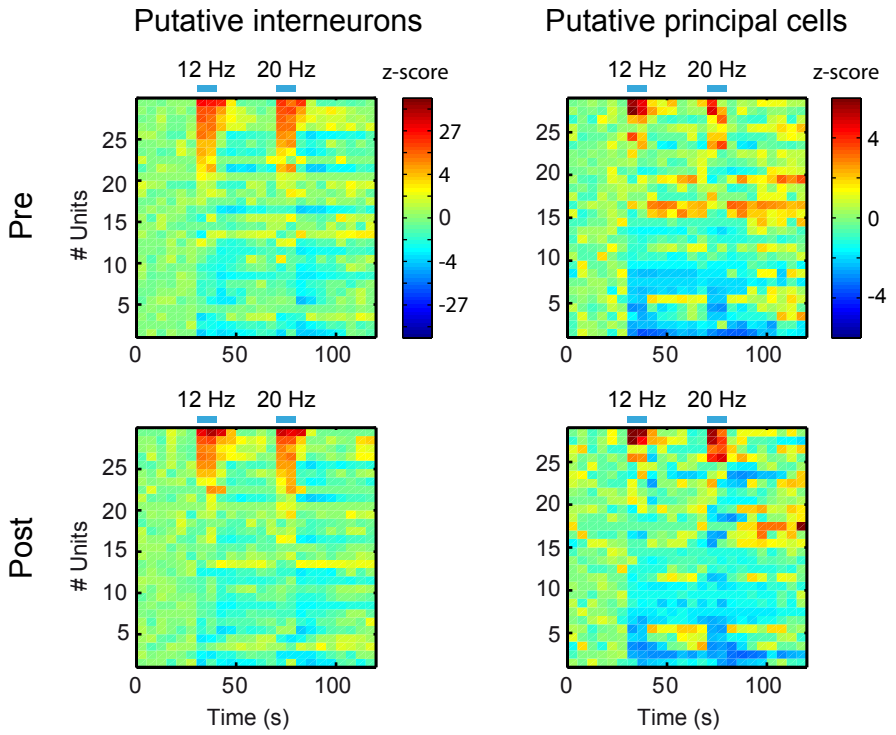

Figure 3.34 – Focal injection of ACSF as a control solution into the MSvDB appears to have no effects on the cholinergic modulation of spiking rates of putative interneurons or principal cells in area CA3 of the dorsal hippocampus. Color scale reflects z-scores of changes in spiking rate relative to baseline activity. Blue bars indicate stimulation of cholinergic MSvDB neurons at 12 Hz and 20 Hz. Time resolution is 5 s. Upper and lower panels show spiking rate modulation of cells before and after focal injection of ACSF, respectively. Each line represents one cell, with the same line in upper and lower panels representing the same cell. Cells are ordered by the mean effect size across the pre and post drug condition for the time period of stimulation at 12 Hz. Left panels show putative interneurons, right panels show putative principal cells. n = 29 putative interneurons from five mice, and n = 28 putative principal cells from six mice.

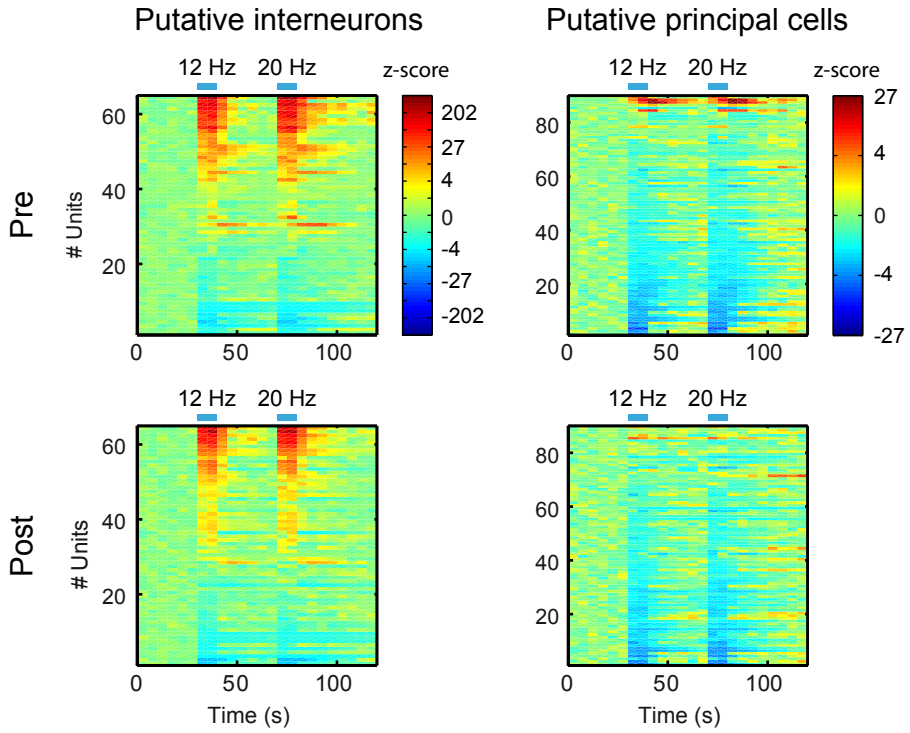

Figure 3.35 – Focal injection of the muscarinic receptor antagonist atropine into the MSvDB has no significant effect on the cholinergic modulation of spiking rates of putative interneurons or principal cells in area CA3 of the dorsal hippocampus. Data are presented as in Figure 3.34. n = 64 putative interneurons from nine mice, and n = 89 putative principal neurons from nine mice.

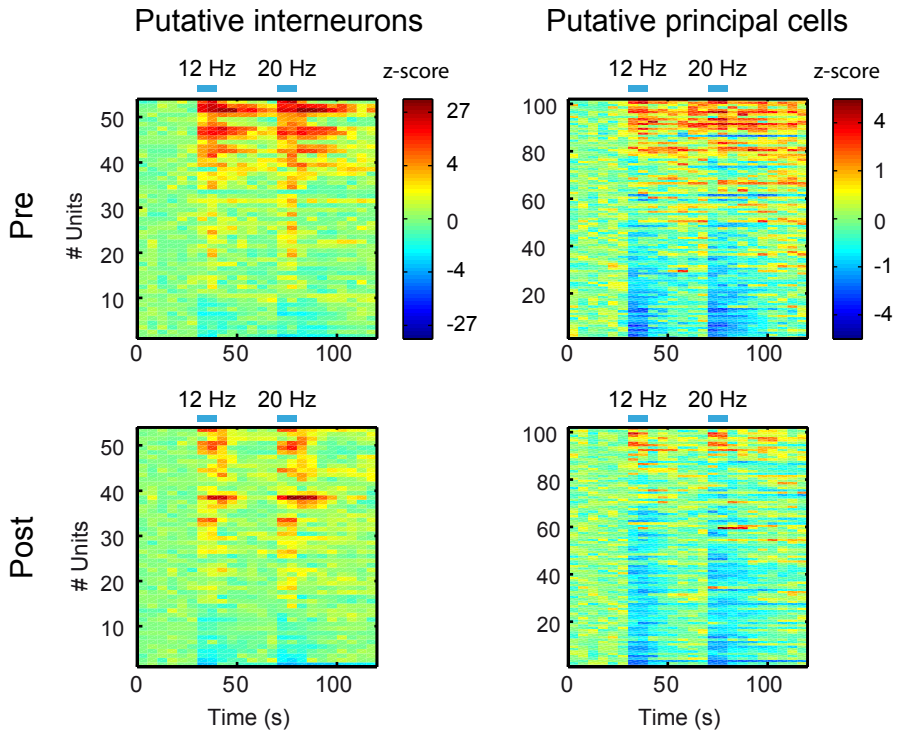

Figure 3.36 – Focal injection of ACSF as a control solution into the dorsal hippocampus has no significant effects on the cholinergic modulation of spiking rates of putative interneurons or principal cells in area CA3. Data are presented as in Figure 3.34. n = 53 putative interneurons from five mice, and n = 101 putative principal neurons from five mice.

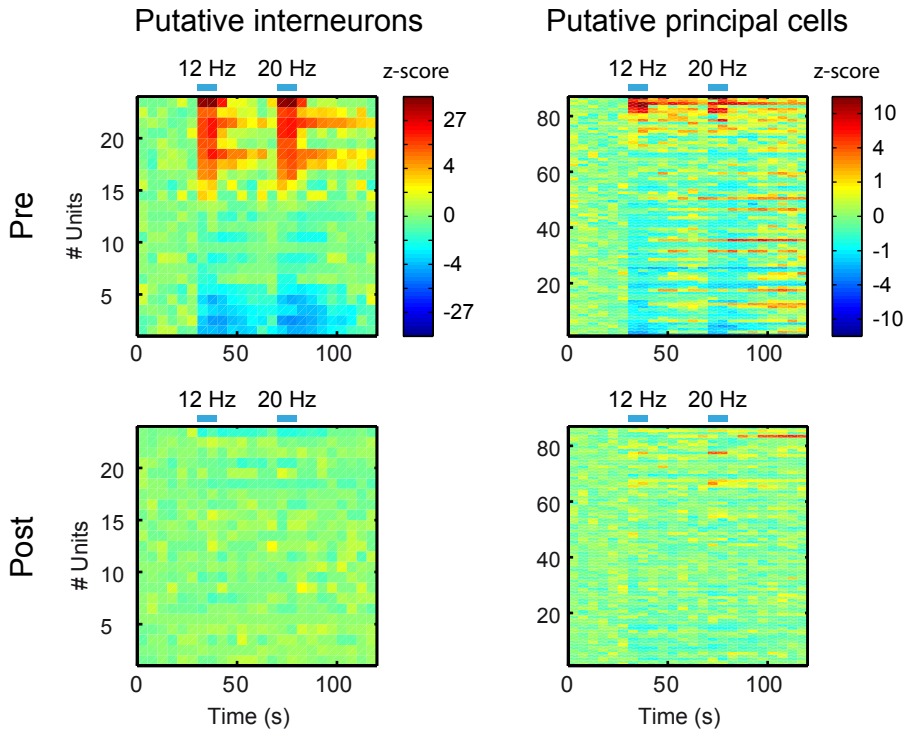

Figure 3.37 – Focal injection of the cholinergic blocker cocktail Atr-Mec-MLA into the dorsal hippocampus abolishes cholinergic modulation of spiking rates of both putative interneurons and principal cells in area CA3. Data are presented as in Figure 3.34. n = 23 putative interneurons from five mice, and n = 86 putative principal neurons from six mice.

focal cholinergic blocker injections into the MSvDB or hippocampus for interneurons and principal cells, I performed two-way ANOVA on the delta modulation indices with the injection site (MSvDB vs. hippocampus) as one and the drug (ACSF vs. blocker) as the other factor. I found a significant main effect of both site and drug for both 12 Hz and 20 Hz stimulation conditions for putative interneurons ($F_{Site(1,165)} = 21.20$, $p < 0.0001$, $F_{Drug(1,165)} = 13.40$, $p = 0.0003$ for 12 Hz stimulation; $F_{Site(1,165)} = 17.03$, $p = 0.0001$, $F_{Drug(1,165)} = 17.96$, $p < 0.0001$ for 20 Hz stimulation) as well as principal cells ($F_{Site(1,300)} = 6.50$, $p = 0.0113$, $F_{Drug(1,300)} = 88.85$, $p = 0.0032$ for 12 Hz stimulation; $F_{Site(1,300)} = 17.46$, $p < 0.0001$, $F_{Drug(1,300)} = 13.81$, $p = 0.0002$ for 20 Hz stimulation). There was a significant interaction between site and drug for interneurons under both stimulation conditions ($F_{Site*Drug(1,165)} = 15.84$, $p = 0.0001$ and $F_{Site*Drug(1,165)} = 11.70$, p=0.0008 for 12 Hz and 20 Hz stimulation, respectively) and for principal cells for the 12 Hz stimulation condition only ($F_{Site*Drug(1,300)} = 6.62$, $p = 0.0106$ and $F_{Site*Drug(1,300)} = 0.44$, $p = 0.5081$ for 12 Hz and 20 Hz stimulation conditions, respectively). Whereas focal atropine injection into the MSvDB had no significant effects on single unit modulation ($p > 0.05$, Tukey-Kramer post hoc test), focal injection of the cholinergic blocker cocktail Atr-Mec-MLA into the hippocampus abolished spiking rate modulation ($p < 0.05$, Tukey-Kramer post hoc test) of putative interneurons for both stimulation conditions (see Figure 3.38C) and strongly reduced spiking rate modulation of putative principal cells, again under both stimulation conditions (see Figure 3.38D). Plotting the modulation indices at 6 minute time bins and fitting a sigmoidal curve

to the data points revealed the time course of the effects of blocker injections into the dorsal hippocampus: Reduction of modulation index showed an onset within the first 10 min after beginning the blocker injections and, for the 12 Hz stimulation condition, reached 50 % of the initial effect size after 15.3 min and 10.5 min for interneurons and principal cells, respectively (see left panels of Figures 3.38E and 3.38F for interneurons and principal cells, respectively). Likewise, for the 20 Hz stimulation condition, 50 % reduction was reached after 14.1 min and 11.7 min for interneurons and principal cells, respectively (see right panels of Figures 3.38E and 3.38F for interneurons and principal cells, respectively). These results suggest that—in contrast to theta generation—modulation of hippocampal unit activity by cholinergic MSvDB neurons requires direct septo-hippocampal projections, but not a septal relay.

3.5. Cholinergic stimulation increases coupling of hippocampal neuronal firing to theta phase

So far, these results show that cholinergic septal neurons induce theta synchronization, but at the same time also cause sparse firing of principal neurons via direct septo-hippocampal projections. We considered the purpose of this dual effect and hypothesized that increasing rhythmic synaptic inputs, while simultaneously hyperpolarizing the target population, would lead to more constrained action potential output that is more strictly related to the phase of ongoing theta activity. I tested this hypothesis by first examining interneuron and principal cell firing with respect to theta phase coupling. I used Kuiper's test to identify units with significant phase coupling (alpha level for type I error set to 0.05) during baseline and stimulation periods (see Figures 3.39A and B for a representative interneuron and pyramidal cell, respectively, with p-values indicated). The number of both principal cells and interneurons with significant theta phase coupling increased during stimulation (see Figures 3.40A and B for CA3 interneurons and principal cells respectively). To further analyze phase coupling at the population level, I determined the length of the mean resultant vector for each unit. This measure revealed significantly increased phase coupling for both the population of putative interneurons (see Figure 3.41A, $p < 0.001$, $n = 120$ from 22 mice, Wilcoxon signed-rank test) and the population of principal cells (see Figure 3.41B, $p < 0.01$, $n = 176$ from 24 mice, Wilcoxon signed-rank test). When considering the phase of the mean resultant vectors only for the phase-coupled units, a preferential phase coupling was observed for interneurons around the descending phase of theta ($77 \pm 56°$, mean ± SD, see Figure 3.42A) and principal cells around the theta trough ($156 \pm 59°$, mean ± SD, see Figure 3.42B).

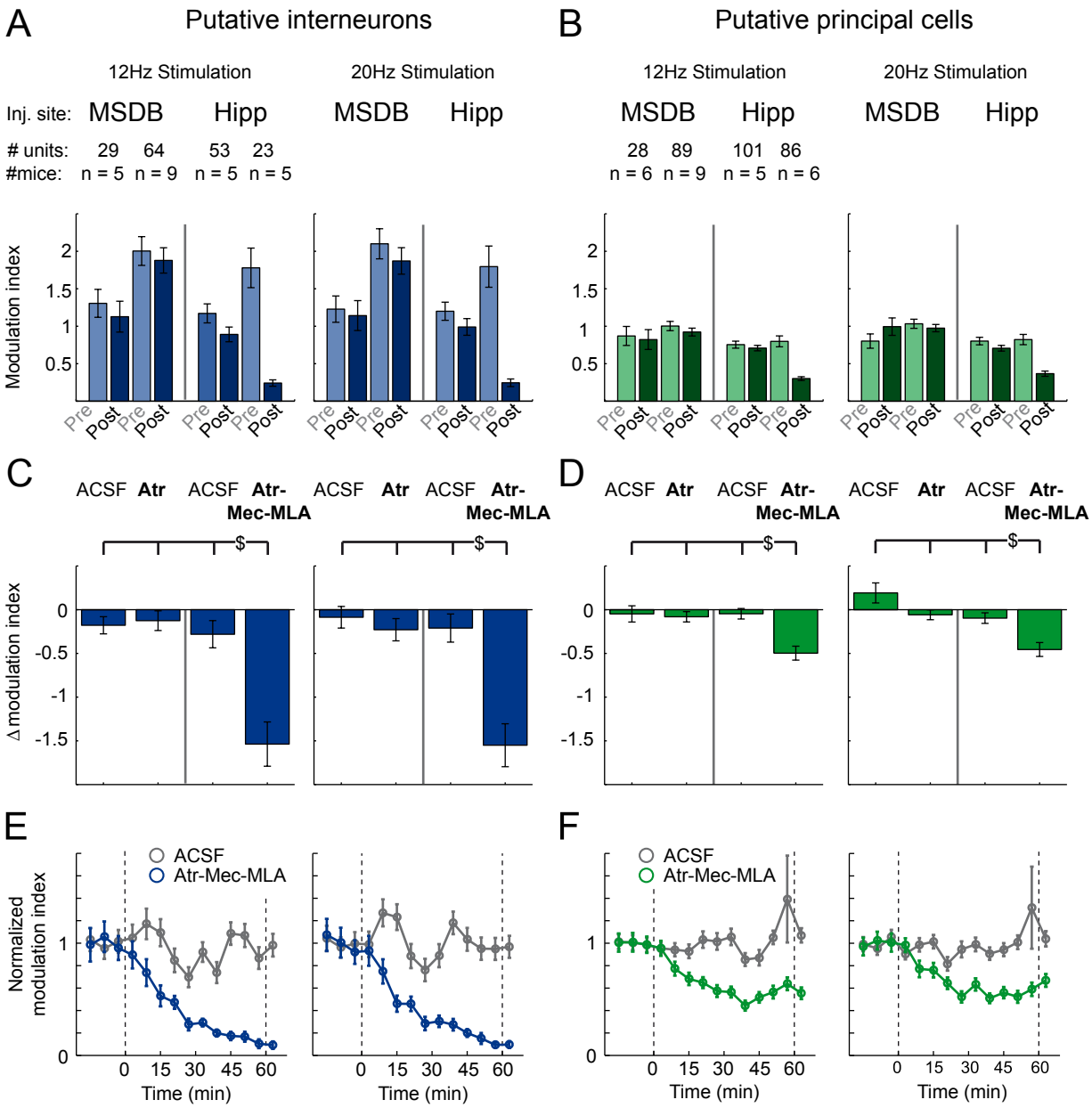

Figure 3.38 – Modulation of neuronal activity in hippocampal area CA3 by cholinergic MSvDB neurons is mediated via direct septo-hippocampal projections. A,B, Focal injections of atropine (Atr, 7.2 mM) into the MSvDB had no effect, whereas focal injections of the cholinergic blocker cocktail Atr-Mec-MLA into the dorsal hippocampus strongly reduced stimulation-induced modulation of interneuron spiking rates (A) and principal cell firing rates (B) for 12 Hz and 20 Hz stimulation (left and right panels, respectively). Bars and error bars represent mean ± SEM of modulation indices of single units pre and post focal injection of either ACSF or blocker into either the MSvDB or the dorsal hippocampus (see panels A and B for number of analyzed units and mice). *Figure legend continued on next page.*

Figure 3.38. – (*Figure legend continued.*) **C,D,** Difference in modulation index for each pre vs. post pair for interneurons and principal cells shown in A and B (post minus pre drug/ACSF injection). Frequency of light stimulation was 12 Hz or 20 Hz (left and right panels, respectively). $ indicates $p < 0.05$ for difference between groups, two-way ANOVA followed by Tukey-Kramer post hoc test. **E,F,** Time course of the effects of blocker injection into the dorsal hippocampus on the modulation indices of interneurons (E) and principal cells (F) for 12 Hz and 20 Hz stimulation (left and right panels, respectively). Modulation index was determined as in panels A and B for 6 minutes time bins. Vertical dashed lines indicate the onset and offset of the blocker injection series. Applying a sigmoidal fit to the data revealed that 50 % of reduction of interneuron modulation was reached after 15.3 min and 14.1 min (12 Hz and 20 Hz stimulation, respectively), and reduction of principal cell modulation was reached after 10.5 min and 11.7 min (12 Hz and 20 Hz stimulation, respectively). Control experiments with ACSF injections are shown in grey, experiments with blocker injections in blue or green. Symbols represent mean ± SEM, same neurons as in A–D.

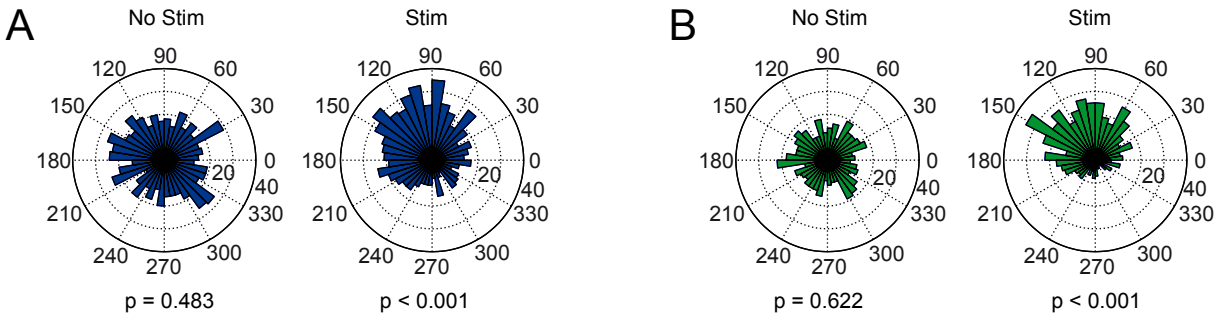

Figure 3.39 – Stimulation of cholinergic MSvDB neurons increased spike-phase coupling of individual neurons in the CA3 subfield of the dorsal hippocampus. Spike phase distribution of a single putative interneuron (A) or principal cell (B) during the baseline (No Stim, left panel) or stimulation (Stim, right panel) period.

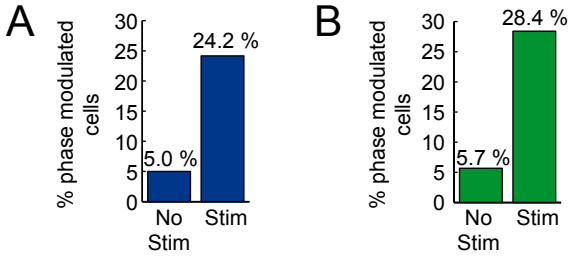

Figure 3.40 – Stimulation of cholinergic MSvDB neurons increased the number of significantly theta-phase modulated neurons in the CA3 subfield. The number of putative interneurons (A) and putative principal cells (B) which fired significantly phase coupled (alpha < 0.05, Kuiper's test) to the local theta rhythm increased during optogenetic stimulation from 6 to 29 (from a total of 120 putative interneurons recorded from 22 mice) and from 10 to 50 (from a total of 176 putative principal cells recorded from 24 mice), respectively. Spike numbers of baseline and stimulation conditions were matched by random spike deletion (see Materials and Methods).

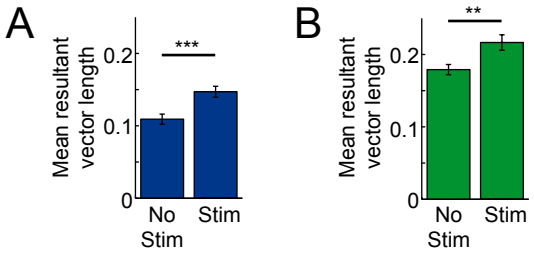

Figure 3.41 – Stimulation of cholinergic MSvDB neurons increased spike-phase coupling of CA3 neurons at the population level. The mean resultant vector lengths averaged across putative interneurons (A) and putative principal cells (B) increased significantly with respect to baseline during the stimulation periods. The same number of spikes were analyzed for the baseline and stimulation conditions. Spike numbers of baseline and stimulation conditions were matched by random spike deletion (see Materials and Methods). Bar graphs show mean ± SEM, **p $<$ 0.01, ***p $<$ 0.001, Wilcoxon signed-rank test.

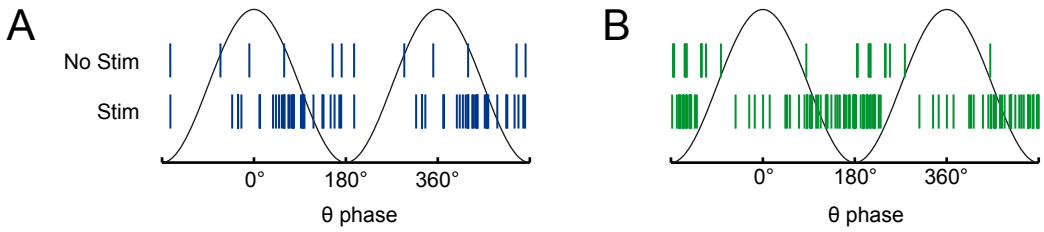

Figure 3.42 – Phase-modulated interneurons and principal cells in CA3 fire at a preferred phase of the hippocampal theta rhythm. A, Mean resultant vector angles of significantly (alpha $<$ 0.05, Kuiper's test) theta-phase coupled putative interneurons, n = 6 and 29 for baseline (No Stim) and cholinergic stimulation (Stim) condition, respectively. **B,** Mean resultant vector angles of significantly (alpha $<$ 0.05, Kuiper's test) theta-phase coupled putative principal cells, n = 10 and 50 for baseline (No Stim) and cholinergic stimulation (Stim) condition, respectively. Note that spiking of putative interneurons clusters around the descending phase ($77 \pm 56°$, mean ± SD), whereas spiking of putative principal cells clusters around the trough ($156 \pm 59°$, mean ± SD) of the local theta rhythm.

4. Discussion

4.1. Main findings

The cholinergic septo-hippocampal system has long been recognized for its vital role in learning and memory by modulating hippocampal network activity. Taking advantage of the recent development of optogenetic tools, I discovered that activity of cholinergic neurons within the MSvDB modulate hippocampal theta oscillations and neuronal spiking via two distinct pathways, namely the direct and the indirect pathway. The direct pathway consists of the septo-hippocampal cholinergic projection fibers, whereas the indirect pathway is based on intraseptal connections to non-cholinergic septo-hippocampal projection neurons. With respect to neuronal spiking activity, this study mainly focused on the CA3 subfield of the hippocampus, because the neurons of this area form an autoassociative network hypothesized to have an essential role for encoding and retrieval processes. I found that the activity of the direct cholinergic pathway mediates an increase of spiking rates in most interneurons, but inhibits the great majority of hippocampal principal cells. In contrast, activity of the indirect pathway is required for hippocampal theta synchronization and mediates a sustained increase in hippocampal theta oscillations. Finally, I show that the synergistic action of both pathways generates reduced, but more precisely theta phase-coupled pyramidal cell firing centered near the trough of the local theta oscillatory phase. My findings thus demonstrate that ACh release from MSvDB neurons has two anatomically and functionally separable effects that act synergistically on the hippocampal network to couple pyramidal neuron spiking more precisely to the theta oscillatory phase (see Figure 4.1 for a schematic diagram of the functional role of the two pathways with respect to CA3 pyramidal neuron spiking patterns). This may be relevant for the separation of encoding and retrieval processes during spatial or episodic memory formation in behaving animals or humans.

4.2. Modulation of hippocampal oscillatory activity by cholinergic MSvDB neurons

My first major finding was that optogenetic stimulation of MSvDB cholinergic neurons induces hippocampal theta oscillations with a relatively delayed on- and offset at a time scale of seconds. The frequency band of these cholinergic stimulation-induced theta oscillations was 3–6 Hz, which

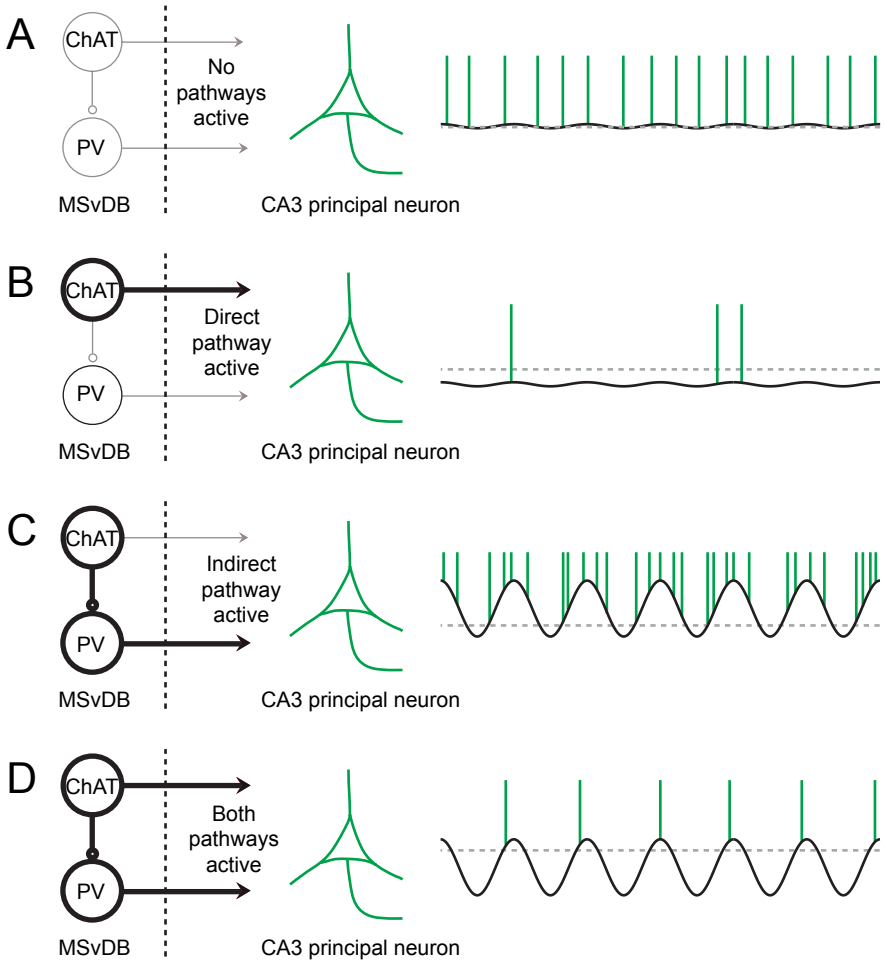

Figure 4.1 – Synergy of the direct and indirect cholinergic pathway structures firing patterns in hippocampal subfield CA3. Schematic drawing depicting how the synergy of direct and indirect cholinergic septo-hippocampal pathways may coordinate firing of principal cells in hippocampal subfield CA3. The solid black line line indicates the membrane potential of a representative CA3 principal cell across time, the gray dotted line indicates the resting membrane potential, when no pathway is active, and the green vertical lines indicate the occurrence of action potentials. **A,** If no pathway is active, the membrane potential of the majority of CA3 principal cells shows only small deviations from the resting membrane potential and a regular spiking activity. **B,** Activation of the direct pathway hyperpolarizes the majority of CA3 principal neurons, which results in a strongly reduced spiking rate. **C,** In contrast, activation of the indirect pathway results in a rhythmic disinhibition of the majority of CA3 principal cells, which results in increased spiking activity. **D,** The synergistic action of both the direct and indirect cholinergic septo-hippocampal pathways results in reduced, but more precisely theta phase-coupled spiking activity.

resembles the frequency range of the atropine-sensitive type of theta as initially described by Kramis et al. (1975) for rats and rabbits under urethane anesthesia or alert immobility, and more recently for urethane-anesthetized mice by Shin et al. (2005), and Barth and Mody (2011). Urethane blocks the atropine-resistant component of theta (Kramis et al., 1975), which is prevalent during movement or REM sleep, and has been suggested to depend primarily on entorhinal cortex inputs to the hippocampus (Buzsáki, 2002). These inputs are one major current generator within the hippocampus. Interestingly, the phase of hippocampal theta oscillations observed in my experiments did not vary much across layers, which is in sharp contrast to a complete phase reversal (180°) from str. pyramidale to the hippocampal fissure observed in drug-free, freely behaving mice (Buzsáki et al., 2003). The absence of a phase reversal indicates the presence of only one major current generator (or multiple current generators with the same laminar profile). Taken together, it appears that entorhinal cortex inputs were strongly suppressed during my experiments and that the observed atropine-sensitive theta was mainly generated by an intrahippocampal circuitry paced by medial septal inputs. This is consistent with the results of a combined independent component and current source density study carried out by Korovaichuk et al. (2010) showing that the contributions of the major excitatory pathways, namely the Schaffer collaterals and the perforant path fibers, to the power of ongoing LFP signals is only ca. 5–7 % under urethane anesthesia in rats. Complementary to this study, Soltesz and Deschenes (1993) carried out simultaneous intra- and extracellular measurements in the hippocampus of rats under ketamine-xylazine anesthesia, demonstrating that the phase and amplitude of theta-rhythmic changes of principal cell membrane voltage depends on the cellular chloride reversal potential as well as the cell membrane potential. Based on these results, Soltesz and Deschenes (1993) hypothesized that rhythmic, high-frequency $GABA_A$ receptor-mediated IPSPs measured in hippocampal pyramidal neurons have an important role in the generation of theta rhythmic activity. The data of this study corroborate this hypothesis by showing that rhythmic inhibition of hippocampal interneurons by GABAergic MSvDB neurons is sufficient for hippocampal theta synchronization in the urethane-anesthetized mouse. In the following part of my discussion I will first focus on the characteristic features of hippocampal theta oscillations induced by activation of cholinergic MSvDB neurons. Later on I will come back to the discussion on the role of hippocampal interneurons for the generation of septally paced rhythmic activity within the hippocampal network.

Although cholinergic stimulation-induced increases of corrected theta peak power and frequency were correlated with the frequency of stimulation, the two effects strongly differed in their magnitude. Whereas corrected theta peak power approximately doubled, when the stimulation frequency was increased from 3 Hz to 40 Hz, I observed only small changes in theta peak frequency (0.8 Hz for the same $>$ 10-fold change in stimulation frequency). This finding suggests that the cholinergic MSvDB neurons have a major role for activating the septal pacemaker

activity, but a minor role in setting the frequency of this pacemaker. Furthermore, cholinergic stimulation-induced theta oscillations have a slow on- and offset. Taken together, this is consistent with a slow second-messenger cascade mediated by G-protein coupled muscarinic AChRs. Indee, hippocampal theta oscillations were abolished in my experiments after local injections of the muscarinic AChR antagonist atropine into the MSvDB.

One major finding reported here with respect to the induction of hippocampal theta oscillatory activity during optogenetic stimulation of cholinergic MSvDB neurons is the suppression of frequency bands adjacent to the theta peak frequency. Similar effects have recently been observed in urethane-anesthetized and freely moving mice by Vandecasteele et al. (2014). In freely moving mice, however, optogenetic stimulation of cholinergic MSvDB neurons did not increase the absolute theta power. Nevertheless, the suppression of adjacent frequency bands increased relative theta prominence in the LFP signal, resulting in an increase of the theta/slow oscillation power ratio. This raises the interesting question whether the relative contributions of functionally separable frequency bands may be more important with respect to network computations than the actual absolute powers. Notably, the suppression of hippocampal slow oscillations between 1–3 Hz observed in my experiments is similar to results obtained from studies on the visual cortex during stimulation of basal forebrain cholinergic neurons (Pinto et al., 2013). The authors reported that light activation of cholinergic neurons of the basal forebrain (including the nucleus basalis, substantia innominata, and the horizontal limb of the diagonal band of Broca) suppressed slow oscillations in area V1 of the visual cortex in awake head-restrained mice, modulated neuronal firing, and improved performance of a visual discrimination task. Thus, cholinergic modulation may be a general mechanism for enhancing sensory perception and attention, and for temporal organization of neuronal spiking activity.

In addition to the induction of theta oscillatory activity, stimulation of cholinergic MSvDB neurons induced increases of hippocampal oscillatory power in a broad range between 15–50 Hz (see Figure 3.6). This resembles an increase of slow gamma activity, which I quantified within the frequency range of 26–48 Hz (see Figure 3.9). In contrast to theta oscillatory power, stimulation-induced changes in gamma power had a faster onset and were long-lasting over tens of seconds. However, effects on slow gamma power were very variable across time, trials, and animals, and I will therefore not further discuss these effects.

4.3. Intraseptal connectivity

The experiments with local atropine injections into the MSvDB performed in this thesis show that pacing hippocampal theta rhythmic activity requires an intraseptal relay. These results are consistent with the inhibition of the so-called atropine sensitive theta oscillations by focal atropine injection into the medial septal region of rats and rabbits as initially shown by Kramis et al.

(1975). Conversely, activating MSvDB neurons by intraseptal infusion of muscarinic agonists in behaving rats causes continuous theta field activity, confirming that intraseptal cholinergic stimulation is not only necessary, but also sufficient for the induction of hippocampal theta oscillations (Lawson and Bland, 1993). Importantly, bath application of cholinergic agonists to hippocampal slices *in vitro* has been reported to elicit theta-like oscillations (Konopacki et al., 1987, see Kowalczyk et al., 2013, for a review), indicating that the hippocampus' internal connectivity per se is sufficient to generate theta rhythmicity. However, one should be aware that a substantial proportion of neuronal processes are cut during the slicing procedure for obtaining acute hippocampal slices, which probably results in an altered excitation-inhibition balance compared to the *in vivo* situation. In addition, Colom et al. (1991) showed for urethane-anesthetized rats *in vivo* that under conditions of pharmacological inactivation of the MSvDB achieved by local procaine injection theta-like oscillations could only be induced by the combination of intrahippocampal microinfusions of the muscarinic AChR agonist carbachol and the $GABA_A$ receptor antagonist bicuculline. Hence, it appears that the activation of muscarinic AChRs alone is not sufficient to induce theta-like oscillations in an intact network *in vivo*, and that impairments of inhibition may also be involved in generating these oscillations. Note that the activation of PV^+ MSvDB projection neurons provide rhythmic hippocampal disinhibition. In line with the results from Colom et al. (1991), Brandon et al. (2014) show that local injection of the $GABA_A$ receptor agonist muscimol into the MSvDB in freely moving rats diminishes the power of hippocampal theta oscillations below 20 % compared to baseline. In summary, under physiological *in vivo* conditions, it appears that the MSvDB is necessary for a major amplification and the pacing of hippocampal theta oscillations.

My *in vitro* experiments in acute slices of the MSvDB showed a long-lasting depolarizing effect of cholinergic MSvDB neuron activation on putative PV^+ GABAergic MSvDB neurons, which was significantly larger than the depolarizing effects on neurons classified as non-PV^+ neurons (see Figures 3.23, 3.24, and 3.25). These results are consistent with anatomical data showing that non-cholinergic MSvDB neurons are contacted by cholinergic terminals (Bialowas and Frotscher, 1987; Léránth and Frotscher, 1989). Likewise, Wu et al. (2000) showed in acute slices of rats that application of muscarine resulted in a hyperpolarization of 1–10 mV in 62 % of MSvDB neurons identified by fluorescent immunolabeling as cholinergic. The remaining 38 % of cholinergic neurons received neither excitation nor inhibition. In contrast, 87.5 % of putative PV^+ GABAergic MSvDB neurons responded with a striking increase in firing rate, similar to what we observed in seven out of fifteen cells in our *in vitro* experiments using optogenetic stimulation-induced synaptic ACh release in slices obtained from mice. In a follow-up study, the same authors identified the M3 type of muscarinic receptors as the main mediator of cholinergic activation of GABAergic neurons within the MSvDB (Alreja et al., 2000). Taken together, these data support our hypothesis of the existence of an intraseptal relay with a strong contribution

of PV^+ GABAergic neurons. However, this does not exclude a contribution of the more recently discovered glutamatergic MSvDB neurons (Colom et al., 2005; Sotty et al., 2003), which—as I described in the introduction—make synaptic contacts with other $VGLUT^+$ glutamatergic, as well as PV^+ GABAergic and $ChAT^+$ cholinergic MSvDB neurons. From a computational perspective, the glutamatergic subpopulation within the MSvDB is thus in a strategic position to provide, maintain, or amplify a general activation signal within the MSvDB network. It remains an important question for future studies, to what extent the glutamatergic MSvDB neurons contribute to the septal relay mediating rhythmic hippocampal synchronization. In my experiments, the local application of atropine to the MSvDB was sufficient to abolish hippocampal theta oscillations, indicating that nicotinic receptors within the MSvDB network are not necessary for pacing hippocampal theta activity. But note that the application of nicotine to rat MSvDB slices *in vitro* has been shown to excite putative GABAergic MSvDB neurons via an indirect mechanism: Glutamatergic MSvDB neurons were activated via nicotinic receptors of the $\alpha 4\beta 2$ type and subsequently excited putative GABAergic MSvDB neurons via type 1 metabotropic glutamate receptors (Wu et al., 2003a). To what extent nicotinic receptors contribute to MSvDB network activity *in vivo*, however, remains to be clarified.

4.4. Modulation of CA3 neuronal activity by direct cholinergic septo-hippocampal projection fibers

The second major finding of this study is that the activity of most CA3 principal neurons is strongly inhibited by activation of MSvDB cholinergic neurons, while the majority of interneurons is activated. In contrast to the effects of cholinergic MSvDB neuron stimulation on hippocampal theta rhythmic activity, the modulation of hippocampal spiking activity did not depend on an intraseptal relay, as shown by the persistence of the modulation effect after local atropine injection into the MSvDB. However, local injection of a cholinergic blocker cocktail into the hippocampus abolished the spiking rate modulation induced by stimulation of cholinergic MSvDB neurons. One can conclude from these results that the observed spiking rate modulation is mediated via cholinergic septo-hippocampal projection fibers, which terminate on both hippocampal interneurons and principal cells. High acetylcholine levels within the hippocampal formation have been hypothesized to set circuit dynamics for attention and encoding, whereas low acetylcholine levels are thought to set dynamics for consolidation (Hasselmo, 2006). Consistent with this idea, the septo-hippocampal cholinergic system is required for the remapping of hippocampal place cell activity after exposure to a novel environment (Ikonen et al., 2002). Moreover, selectively blocking ACh receptors in the CA region via focal scopolamine injection disrupts encoding of spatial information while sparing retrieval. Conversely, enhancing ACh levels in CA3 or CA1 by focal

injections of physostigmine disrupts retrieval, but spares encoding (Rogers and Kesner, 2003). Hence, the reported changes in firing rate of both CA3 interneurons and principal cells during activation of cholinergic MSvDB neurons very likely contributes to switching the cortical network into an encoding state accompanied by theta oscillations.

High oscillatory power has long been known to occlude the occurrence of sharp wave ripple activity and vice versa. Sharp wave ripples are observed during behavioral phases of rest or slow wave sleep and have been proposed to play a prominent role for consolidation of previously learned experiences (Ego-Stengel and Wilson, 2010; Girardeau et al., 2009) as well as for retrieval of information for memory-guided decision-making in awake animals (Jadhav et al., 2012). Strikingly, the corresponding brain states for rest and slow wave sleep are associated with low acetylcholine levels (Marrosu et al., 1995). Furthermore, Vandecasteele et al. (2014) recently described that the incidence of CA3 sharp wave ripple oscillations is strongly reduced in response to optogenetic stimulation of cholinergic MSvDB neurons in urethane-anesthetized as well as freely moving mice. Note that sharp wave ripples are generated in area CA3 of the hippocampus as highly synchronous spiking activity of a large proportion of principal cells (Csicsvari et al., 2000). Thus, the finding from Vandecasteele et al. (2014) is in agreement with my finding of an increase of interneuron activity with a concomitant decrease of principal cell firing during activation of cholinergic MSvDB neurons. However, the detailed mechanisms how synaptically released acetylcholine modulates hippocampal spiking rates remains to be investigated in future studies. McQuiston (2014) has recently proposed an interesting model for hippocampal area CA1, in which high acetylcholine levels cause subsets of interneurons to be depolarized by muscarinic receptor activation resulting in suppression of pyramidal neurons. My results suggest a similar mechanism for area CA3 of the hippocampus. Further possible mechanisms for the cholinergic modulation of hippocampal spiking rates are effects on synaptic transmission efficacy, changes in dendritic excitability, or effects on astrocytes (Araque et al., 2002). Furthermore, Martinello et al. (2015) recently described a lowering of the action potential threshold in dentate gyrus granule cells during electrical stimulation of cholinergic fibers in mouse hippocampal slices. Importantly, all these mechanisms may act in concert and result in complex network effects.

So far, I have discussed the effect of hippocampal acetylcholine on the spiking rates of an average putative interneuron and principal cell in CA3. If high and low levels of hippocampal acetylcholine change network dynamics, e.g. to favor encoding or consolidation, the question arises, if different subsets of neurons are preferentially active during these two network states. Note that the spiking rates of CA3 principal cells and interneurons follow a lognormal distribution (see Figure 3.14A). Such lognormal distributions have been previously described for the spiking rates of principal cells of the hippocampus and entorhinal cortex (Mizuseki and Buzsáki, 2013),

and also for other functional and anatomical brain parameters[1]. Based on this finding, the authors of that study concluded that there is a preconfigured minority of a highly active subset of neurons that dominates information processing in cortical networks (Mizuseki and Buzsáki, 2013). In my experiments, the spiking rates of neurons were correlated between the baseline and cholinergic stimulation conditions (see Figure 3.14B for both interneurons and principal cells). This is mainly due to the fact that the neurons that are highly active under the baseline condition also constitute a large part of the subset of neurons highly active during cholinergic stimulation. This finding is consistent with the results of a study by Mizuseki and Buzsáki (2013), in which the authors correlated the firing rates of single principal neurons of the hippocampus and entorhinal cortex between different behavioral states in rats, namely slow wave sleep vs. REM sleep, slow wave sleep vs. running, and running in a familiar maze vs. running in a novel environment. The authors of that study suggested that the firing rates of principal neurons are preserved across brain states associated with a low or high cholinergic tone. My findings corroborate this conclusion.

4.5. Modulation of CA3 network activity by GABAergic MSvDB neurons

Next, I examined the neuronal circuits underlying the induction of hippocampal theta rhythmic activity on the one hand, and inhibition of the majority of CA3 pyramidal cells on the other hand. As noted earlier, I found that blocking MSvDB muscarinic ACh receptors by local atropine application abolished stimulation-induced hippocampal theta oscillations, indicating the necessity of a septal relay for theta induction. Notably, local application of muscarinic and nicotinic blockers to the hippocampus also diminished stimulation-induced hippocampal theta oscillations indicating that ambient acetylcholine is necessary for the hippocampal network to be responsive to a pacemaker signal from the MSvDB. Strikingly, basal spiking rates of interneurons strongly decrease after local cholinergic blocker injection into the hippocampus, pointing to a prominent role of interneurons for this responsive network state and rhythmic activity. In principle, different types of hippocampal interneurons appear to be recruited by ACh release from cholinergic axons, both *in vitro* (Cea-del Rio et al., 2010; Lawrence et al., 2006b; Nagode et al., 2011, 2014; Widmer et al., 2006) and *in vivo* (Lovett-Barron et al., 2014). Interestingly, Stark et al. (2013) showed that theta-rhythmic optogenetic activation of PV^+ hippocampal interneurons induced postinhibitory resonant spiking activity in area CA1 in freely moving mice. Furthermore, inhibition-induced theta resonance in CA1 pyramidal cells was abolished by local pharmacological blocking of I_h currents indicating a role of cell-intrinsic resonant mechanisms

[1] For the interested reader I refer to Buzsáki and Mizuseki (2014) for a detailed review on how skewed distributions of brain parameters can affect network operations.

entrained by rhythmic inhibition. PV^+ MSvDB neurons selectively innervate hippocampal interneurons and have long been suggested to pace hippocampal theta rhythmicity via disinhibition of principal cells (Freund and Antal, 1988; Serafin et al., 1996; Tóth et al., 1997). Furthermore, rhythmic activity of PV^+ MSvDB neurons have been shown to lead the activity of hippocampal interneurons and hippocampal theta activity (Hangya et al., 2009). In my experiments, I show a causal relationship between the rhythmic activation of PV^+ MSvDB neurons and hippocampal rhythmic field potential signals: Light-stimulation of PV^+ MSvDB neurons induces hippocampal rhythmic activity precisely at the stimulation frequency. Hence, PV^+ GABAergic MSvDB neurons are capable of precise synchronization of hippocampal networks *in vivo*. Unfortunately, the specific interneuron types that mediate cholinergic inhibition in the CA3 region can currently not be identified on the basis of single unit recordings. $VGLUT2^+$ glutamatergic neurons within the MSvDB may additionally contribute to the oscillatory state of the hippocampus and the observed modulation of hippocampal neurons' spiking rates. In favor of such a contribution, Huh et al. (2010) found fast, α-amino-3-hydroxy-5-methyl-4-isoxazolepropionic acid (AMPA) receptor mediated glutamatergic responses in CA3 pyramidal cells after chemical activation of the MSvDB in an *in vitro* septohippocampal preparation. However, the *in vivo* function of this connection remains to be investigated. Furthermore, evidence for functional synaptic input of glutamatergic MSvDB neurons onto hippocampal interneurons is missing so far. Collectively, the presented data suggest that cholinergic MSvDB neurons recruit PV^+ and possibly other neurons within the MSvDB, which then mediate hippocampal theta synchronization.

It is still an unresolved question, if different interneuron types within the dentate gyrus and hippocampus are differentially targeted by different subpopulations of PV^+ GABAergic MSvDB projection neurons. Based on this idea, Borhegyi et al. (2004) suggested a model in which PV^+ GABAergic MSvDB neurons, which fired either at the trough or the peak of hippocampal theta oscillations recorded in urethane-anesthetized rats, differentially target O-LM cells or basket cells, respectively, thereby providing phase-dependent compartment-specific inhibition of hippocampal pyramidal neurons. They do not provide any evidence, however, that different subsets of PV^+ MSvDB neurons differentially innervate different hippocampal interneuron types.

The different hippocampal interneuron types not only target different somatic or dendritic domains, but also fire at other phases of ongoing theta oscillations. This provides varying temporal windows for computations at several cellular compartments and might be important for creating theta resonance within the hippocampal formation (see Klausberger and Somogyi, 2008, for a review). Indeed, Mizuseki et al. (2009) observed that theta oscillations provide a temporal window of 70–80 ms for local circuit operations in the entorhinal-hippocampal network, which is much longer than it would be expected based on axonal conduction times, synaptic delays, and passive synaptic integration between entorhinal cortex input and hippocampal output activity. Furthermore, a recent computational study showed that theta modulated inhibition can account

for such a long temporal window (Cutsuridis and Poirazi, 2015).

Importantly, the spiking rate modulation of hippocampal neurons appeared to be only very mildly affected, if at all, by cholinergic antagonists injected into the MSvDB, hence indicating that spiking rate modulation does not require a septal relay. Thus, anatomically separable pathways are responsible for inducing theta oscillations on the one hand, and for causing reduced (but temporally more precise) spiking activity of CA3 neurons on the other hand.

4.6. Synergy of direct and indirect cholinergic septo-hippocampal pathways for coordination of spiking activity in area CA3 of the hippocampus

What could be the functional purpose for implementing theta resonance simultaneous with sparser firing in CA3 pyramidal neurons? The inhibition of CA3 firing, mediated by the direct cholinergic septo-hippocampal pathway, confirms a prediction made by an influential model for hippocampal encoding and retrieval initially proposed by M.E. Hasselmo (Hasselmo, 1999; Hasselmo et al., 2002). In this model, high levels of acetylcholine present during active waking set the appropriate dynamics for encoding new information in the hippocampus by suppressing recurrent excitatory feedback connections and thereby facilitating encoding without interference from previously stored information. I will present a brief synopsis of the major studies supporting this model: Giocomo and Hasselmo (2005) showed *in vitro* for area CA3 of the hippocampus that nicotinic modulation enhances excitatory transmission in str. lacunosum moleculare, the input zone of entorhinal cortex fibers, but not in str. radiatum, which is the input zone for recurrent excitatory transmission. Interestingly, this effect appears to depend on inhibitory interneurons, since it was blocked by the application of the $GABA_A$ antagonist picrotoxin. Conversely, application of the muscarinic AChR agonist carbachol to hippocampal slices produced a significantly stronger suppression of electrical stimulus-evoked EPSPs in str. radiatum than in str. lacunosum-moleculare (Hasselmo and Schnell, 1994). Likewise, carbachol application *in vitro* increased the failure rate of functional synapses more than the one of silent[1] synapses in hippocampal CA1 pyramidal neurons (Fernández de Sevilla et al., 2002). Continuing the studies from Hasselmo and Schnell (1994), Kremin and Hasselmo (2007) showed that the laminar specific cholinergic suppression of glutamatergic synaptic transmission holds true also for area CA3 of the hippocampus. In addition, Kremin and Hasselmo (2007) suggested a presynaptic mechanism mediated by muscarinic AChRs. Both my results as well as the inhibition of CA3 sharp wave-ripple complexes (as shown

[1] Silent synapses are excitatory synapses lacking functional AMPA receptors in the postsynaptic membrane. Hence, they respond only to stimulation if the postsynaptic cell is depolarized above its resting membrane potential (Isaac et al., 1995).

by Vandecasteele et al., 2014) provide further support for the Hasselmo-model by demonstrating that the autoassociative CA3 network is inhibited during stimulation of cholinergic MSvDB neurons.

But how does the increase in theta oscillatory power contribute to a network state favoring the encoding of information? Theta oscillations which require a septal relay are associated with membrane potential fluctuations in CA1 and CA3 interneurons and principal cells (Fox, 1989; Fujita and Sato, 1964; Kamondi et al., 1998). I reasoned that such an effect, coupled with a simultaneous hyperpolarization of CA3 pyramidal cells, would render the principal neurons more likely to fire in a theta-coupled manner.

The model depicted in Figure 4.1 illustrates how rhythmic membrane oscillations of a hyperpolarized and hence sparsely firing CA3 pyramidal neuron leads to theta resonant firing behavior. Indeed, we found a ca. five fold increase in the number of significantly theta phase-coupled interneurons and principal cells (see Figure 3.40) and an increase of the average across the neurons' mean resultant vector lengths (see Figure 3.41), indicating a significantly stronger theta phase-coupling of CA3 interneuron and pyramidal cell firing during optogenetic stimulation of cholinergic MSvDB neurons. This conclusion holds true also at the single cell level for both interneurons and principal cells, as evident by the significant result of the paired non-parametric testing applied to test the difference between the neurons' mean resultant vector lengths during baseline and cholinergic stimulation. Note that the enhancement of theta oscillatory power per se may contribute to this increase in theta phase coupled spiking activity, because theta phase is less likely to be distorted by oscillatory activity at other frequency bands. Nevertheless, more precise timing of CA3 neuron firing with respect to the theta phase may promote plasticity in either the autoassociative CA3 network or in CA3-CA1 projections (Hölscher et al., 1997; Hyman et al., 2003; Orr et al., 2001; Pavlides et al., 1988). Moreover, my findings support an extension of the already introduced model proposed by M.E. Hasselmo, in which the peak and trough of theta oscillations are hypothesized to provide temporal windows for the encoding and retrieval of episodic or spatial memories (*s*eparate *p*hases of *e*ncoding *a*nd *r*etrieval (SPEAR) model, see Hasselmo et al., 2002). According to the SPEAR model these different temporal windows for encoding and retrieval are given by the peak and trough of the ongoing theta oscillation recorded in str. pyramidale, respectively. By introducing different temporal windows to separate encoding from retrieval processes within one theta cycle, the SPEAR model provides a hypothetical solution for the so-called interference problem. The interference problem occurs when context-relevant information from previously stored memories is recalled at the same time at which novel information is encoded. This is problematic, because an old memory trace might be encoded as part of a newly formed memory trace. In my experiments with optogenetic stimulation of cholinergic MSvDB neurons, CA3 pyramidal neurons spiked preferentially near the trough of the

theta rhythm recorded in str. pyramidale. Thus, retrieval associated activity of the CA3 autoassociative network coincides with the phase of theta, in which LTD is favored (Huerta and Lisman, 1995) and entorhinal cortex input is weakest (Kamondi et al., 1998), hence termed the retrieval phase in the SPEAR model. In addition to the overall reduction of CA3 principal cell spiking during cholinergic stimulation, increasing the phase locking of CA3 principal cell spiking to the trough of the local theta oscillation may further prevent forming wrong associations between retrieval associated spiking activity and encoding associated synaptic inputs. My findings may therefore be relevant to explain the increased phase locking of neuronal firing to theta oscillations observed during memory encoding. Such an effect has been observed in the human medial temporal lobe, and is predictive of subsequent memory performance (Rutishauser et al., 2010). In monkeys, phase locking of single unit activity was observed in the cortex during working memory tasks, and this is likewise predictive of memory performance (Liebe et al., 2012). It should be noted, however, that these conclusions are based on data obtained in anesthetized animals, in which principal and interneuron discharge rates are likely modulated by the anesthetic agent. Particularly, urethane anesthesia has been shown to decrease the firing rates of hippocampal interneurons up to 50 % in rats (Buzsáki et al., 1983). However, the phase relation of spikes in relation to the ongoing theta oscillations was retained in those experiments. Furthermore, theta phase-coupling of PV^+ basket cells and ivy cells recorded in freely moving rats (Lapray et al., 2012) is very similar to the one observed under combined urethane-ketamine-xylazine anesthesia (see Klausberger et al., 2003, for recordings of PV^+ basket cells, and Fuentealba et al., 2008, for recordings of ivy cells), suggesting preserved theta phase relations of spiking activity under anesthesia. Nevertheless, experiments in behaving animals would be required to determine how the indirect and direct pathways are recruited in behaviorally relevant situations. In order to prove a causal role of theta phase-coupled spiking of CA3 pyramidal neurons for memory processes, it would be necessary to inhibit CA3 pyramidal cell spiking activity selectively at different phases of the underlying hippocampal theta rhythm during a memory task.

In summary, the data presented in this thesis reveal two cholinergic network motifs, a direct and an indirect pathway, that act synergistically to organize firing of hippocampal neurons. These circuits may be relevant for information encoding, when cholinergic tone is increased during exploratory behavior or novelty experience (Aloisi et al., 1997; Bianchi et al., 2003).

A. Abbreviations

4-AP	4-aminopyridine
AAV	adeno-associated virus
Aβ	amyloid β
ACh	acetylcholine
AChE	acetylcholinesterase
AChR	acetylcholine receptor
ACSF	artificial cerebrospinal fluid
AD	Alzheimer's disease
ADP	afterdepolarization
AHP	afterhyperpolarization
AMPA	α-amino-3-hydroxy-5-methyl-4-isoxazolepropionic acid
ANOVA	analysis of variance
Atr	atropine
bp	base pair
CA	cornu ammonis (*latin* ammon's horn)
cAMP	cyclic adenosine monophosphate
CCK	cholecystokinin
ChAT	choline acetyltransferase
ChR2	channelrhodopsin 2
Cy3	cyanine dye 3
dd	double distilled
DG	dentate gyrus
dNTP	deoxynucleoside triphosphate
EF-1α	elongation factor-1α

EGTA	ethylene glycol tetraacetic acid
EPSP	excitatory postsynaptic potential
eYFP	enhanced yellow fluorescent protein
fAHP	fast afterhyperpolarization
FITC	fluorescein isothiocyanate
GABA	γ-aminobutyric acid
GAD	glutamic acid decarboxylase
GFP	green fluorescent protein
HEPES	4-(2-hydroxyethyl)-1-piperazineethansulfonic acid
HICAP cell	hilar neuron with its axon distributed in the commissural/associational pathway termination zone
HIPP cell	hilar perforant path-associated cell
i.e.	id est (*latin* that is)
I_h	hyperpolarization-activated inward current
i.p.	intraperitoneal
IP3	inositol trisphosphate
IPSC	inhibitory postsynaptic currents
IPSP	inhibitory postsynaptic potential
IRES	internal ribosome entry site
IS cell	interneuron-specific cell
LFP	local field potential
LTD	long term depression
LTP	long term potentiation
mAChR	muscarinic type of the acetylcholine receptor
Mec	mecamylamine
mEPSC	miniature excitatory postsynaptic currents
mIPSC	miniature inhibitory postsynaptic currents
MLA	methyllycaconitine
MOPP cell	molecular layer perforant path-associated cell
MS	medial septum

MSvDB	medial septum/vertical diagonal band of Broca complex
NA	numerical aperture
nAChR	nicotinic type of the acetylcholine receptor
NMDA	N-methyl-D-aspartate
O-LM cell	oriens lacunosum-moleculare associated cell
PV	parvalbumin
PCR	polymerase chain reaction
PBS	phosphate buffered saline
rAAV	recombinant adeno-associated virus
REM	rapid eye movement
RT	room temperature
S2/1	hybrid serotype of variants 2 and 1
SD	standard deviation
SEM	standard error of the mean
SK channel	small conductance calcium activated potassium channel
SST	somatostatin
str.	stratum
vDB	vertical diagonal band of Broca
VGLUT	vesicular glutamate transporter
WPRE	woodchuck hepatitis virus posttranscriptional regulatory element

B. Bibliography

Albuquerque, E. X., Pereira, E. F. R., Alkondon, M., and Rogers, S. W. (2009). Mammalian nicotinic acetylcholine receptors: From structure to function. *Physiological Reviews*, 89(1):73–120.

Alkondon, M. and Albuquerque, E. X. (2004). The nicotinic acetylcholine receptor subtypes and their function in the hippocampus and cerebral cortex. *Progress in Brain Research*, 145:109–120.

Alkondon, M., Pereira, E. F. R., Eisenberg, H. M., and Albuquerque, E. X. (1999). Choline and selective antagonists identify two subtypes of nicotinic acetylcholine receptors that modulate GABA release from CA1 interneurons in rat hippocampal slices. *The Journal of Neuroscience*, 19(7):2693–2705.

Aloisi, A. M., Casamenti, F., Scali, C., Pepeu, G., and Carli, G. (1997). Effects of novelty, pain and stress on hippocampal extracellular acetylcholine levels in male rats. *Brain research*, 748(1-2):219–226.

Alreja, M., Wu, M., Liu, W., Atkins, J. B., Leranth, C., and Shanabrough, M. (2000). Muscarinic tone sustains impulse flow in the septohippocampal GABA but not cholinergic pathway: implications for learning and memory. *The Journal of Neuroscience*, 20(21):8103–8110.

Amaral, D. and Lavenex, P. (2006). Hippocampal Neuroanatomy. In Andersen, P., Morris, R., Amaral, D., Bliss, T., and O'Keefe, J., editors, *The Hippocampus Book*. Oxford Univ. Pr., Oxford; New York, 1st edition.

Amaral, D. G. and Kurz, J. (1985). An analysis of the origins of the cholinergic and noncholinergic septal projections to the hippocampal formation of the rat. *The Journal of Comparative Neurology*, 240(1):37–59.

Andersen, P., Bland, H. B., Myhrer, T., and Schwartzkroin, P. A. (1979). Septo-hippocampal pathway necessary for dentate theta production. *Brain Research*, 165(1):13–22.

Apartis, E., Poindessous-Jazat, F., Epelbaum, J., and Bassant, M. H. (2000). Age-related changes in rhythmically bursting activity in the medial septum of rats. *Brain Research*, 876(1-2):37–47.

Araque, A., Martín, E. D., Perea, G., Arellano, J. I., and Buño, W. (2002). Synaptically released acetylcholine evokes Ca_{2+} elevations in astrocytes in hippocampal slices. *The Journal of Neuroscience*, 22(7):2443–2450.

Atri, A., Sherman, S., Norman, K. A., Kirchhoff, B. A., Nicolas, M. M., Greicius, M. D., Cramer, S. C., Breiter, H. C., Hasselmo, M. E., and Stern, C. E. (2004). Blockade of central cholinergic receptors impairs new learning and increases proactive interference in a word paired-associate memory task. *Behavioral Neuroscience*, 118(1):223–236.

Axmacher, N., Henseler, M. M., Jensen, O., Weinreich, I., Elger, C. E., and Fell, J. (2010). Cross-frequency coupling supports multi-item working memory in the human hippocampus. *Proc Natl Acad Sci U S A*, 107(7):3228–3233.

Barth, A. M. I. and Mody, I. (2011). Changes in hippocampal neuronal activity during and after unilateral selective hippocampal ischemia *in vivo*. *The Journal of Neuroscience*, 31(3):851–860.

Bell, K. A., Shim, H., Chen, C.-K., and McQuiston, A. R. (2011). Nicotinic excitatory postsynaptic potentials in hippocampal CA1 interneurons are predominantly mediated by nicotinic receptors that contain alpha4 and beta2 subunits. *Neuropharmacology*, 61(8):1379–1388.

Bell, L. A., Bell, K. A., and McQuiston, A. R. (2013). Synaptic muscarinic response types in hippocampal CA1 interneurons depend on different levels of presynaptic activity and different muscarinic receptor subtypes. *Neuropharmacology*, 73:160–173.

Bell, L. A., Bell, K. A., and McQuiston, A. R. (2014). Muscarinic receptor activation by optogenetically released acetylcholine in hippocampal CA1 depolarizes VIP-expressing but has varying effects on PV-expressing perisomatic interneurons. *The Journal of Physiology*.

Belluscio, M. A., Mizuseki, K., Schmidt, R., Kempter, R., and Buzsáki, G. (2012). Cross-frequency phase-phase coupling between theta and gamma oscillations in the hippocampus. *The Journal of Neuroscience*, 32(2):423–435.

Benchenane, K., Peyrache, A., Khamassi, M., Tierney, P. L., Gioanni, Y., Battaglia, F. P., and Wiener, S. I. (2010). Coherent theta oscillations and reorganization of spike timing in the hippocampal-prefrontal network upon learning. *Neuron*, 66(6):921–936.

Berry, S. D. and Thompson, R. F. (1978). Prediction of learning rate from the hippocampal electroencephalogram. *Science (New York, N.Y.)*, 200(4347):1298–1300.

Bialowas, J. and Frotscher, M. (1987). Choline acetyltransferase-immunoreactive neurons and terminals in the rat septal complex: a combined light and electron microscopic study. *The Journal of Comparative Neurology*, 259(2):298–307.

Bianchi, L., Ballini, C., Colivicchi, M. A., Della Corte, L., Giovannini, M. G., and Pepeu, G. (2003). Investigation on acetylcholine, aspartate, glutamate and GABA extracellular levels from ventral hippocampus during repeated exploratory activity in the rat. *Neurochemical Research*, 28(3-4):565–573.

Blokland, A., Honig, W., and Raaijmakers, W. G. (1992). Effects of intra-hippocampal scopolamine injections in a repeated spatial acquisition task in the rat. *Psychopharmacology*, 109(3):373–376.

Boccara, C. N., Sargolini, F., Thoresen, V. H., Solstad, T., Witter, M. P., Moser, E. I., and Moser, M.-B. (2010). Grid cells in pre- and parasubiculum. *Nature Neuroscience*, 13(8):987–994.

Borhegyi, Z., Maglóczky, Z., Acsády, L., and Freund, T. F. (1998). The supramammillary nucleus innervates cholinergic and GABAergic neurons in the medial septum-diagonal band of Broca complex. *Neuroscience*, 82(4):1053–1065.

Borhegyi, Z., Varga, V., Szilágyi, N., Fabo, D., and Freund, T. F. (2004). Phase segregation of medial septal GABAergic neurons during hippocampal theta activity. *The Journal of Neuroscience*, 24(39):8470–8479.

Braak, H. and Braak, E. (1991). Neuropathological stageing of Alzheimer-related changes. *Acta Neuropathologica*, 82(4):239–259.

Bragin, A., Jandó, G., Nádasdy, Z., Hetke, J., Wise, K., and Buzsáki, G. (1995). Gamma (40-100 Hz) oscillation in the hippocampus of the behaving rat. *The Journal of Neuroscience*, 15(1 Pt 1):47–60.

Brandon, M. P., Koenig, J., Leutgeb, J. K., and Leutgeb, S. (2014). New and distinct hippocampal place codes are generated in a new environment during septal inactivation. *Neuron*, 82(4):789–796.

Brankack, J., Stewart, M., and Fox, S. E. (1993). Current source density analysis of the hippocampal theta rhythm: associated sustained potentials and candidate synaptic generators. *Brain research*, 615(2):310–327.

Buchanan, K. A., Petrovic, M. M., Chamberlain, S. E. L., Marrion, N. V., and Mellor, J. R. (2010). Facilitation of long-term potentiation by muscarinic M(1) receptors is mediated by inhibition of SK channels. *Neuron*, 68(5):948–963.

Burmeister, J. J., Pomerleau, F., Huettl, P., Gash, C. R., Werner, C. E., Bruno, J. P., and Gerhardt, G. A. (2008). Ceramic-based multisite microelectrode arrays for simultaneous measures of choline and acetylcholine in CNS. *Biosensors & Bioelectronics*, 23(9):1382–1389.

Buzsáki, G. (2002). Theta oscillations in the hippocampus. *Neuron*, 33(3):325–340.

Buzsáki, G. (2011). *Rhythms of the Brain*. Oxford University Press, U.S.A., Oxford ; New York, 1st edition.

Buzsáki, G., Buhl, D. L., Harris, K. D., Csicsvari, J., Czéh, B., and Morozov, A. (2003). Hippocampal network patterns of activity in the mouse. *Neuroscience*, 116(1):201–211.

Buzsáki, G., Leung, L. W., and Vanderwolf, C. H. (1983). Cellular bases of hippocampal EEG in the behaving rat. *Brain research*, 287(2):139–171.

Buzsáki, G. and Mizuseki, K. (2014). The log-dynamic brain: how skewed distributions affect network operations. *Nature Reviews. Neuroscience*, 15(4):264–278.

Cea-del Rio, C. A., Lawrence, J. J., Erdelyi, F., Szabo, G., and McBain, C. J. (2011). Cholinergic modulation amplifies the intrinsic oscillatory properties of CA1 hippocampal cholecystokinin-positive interneurons. *The Journal of Physiology*, 589(Pt 3):609–627.

Cea-del Rio, C. A., Lawrence, J. J., Tricoire, L., Erdelyi, F., Szabo, G., and McBain, C. J. (2010). M3 muscarinic acetylcholine receptor expression confers differential cholinergic modulation to neurochemically distinct hippocampal basket cell subtypes. *The Journal of Neuroscience*, 30(17):6011–6024.

Changeux, J. P., Bertrand, D., Corringer, P. J., Dehaene, S., Edelstein, S., Léna, C., Le Novère, N., Marubio, L., Picciotto, M., and Zoli, M. (1998). Brain nicotinic receptors: structure and regulation, role in learning and reinforcement. *Brain Research. Brain Research Reviews*, 26(2-3):198–216.

Chauvière, L., Rafrafi, N., Thinus-Blanc, C., Bartolomei, F., Esclapez, M., and Bernard, C. (2009). Early deficits in spatial memory and theta rhythm in experimental temporal lobe epilepsy. *The Journal of Neuroscience*, 29(17):5402–5410.

Chen, L. L., Lin, L. H., Green, E. J., Barnes, C. A., and McNaughton, B. L. (1994). Head-direction cells in the rat posterior cortex. I. Anatomical distribution and behavioral modulation. *Experimental Brain Research*, 101(1):8–23.

Cheng, Q. and Yakel, J. L. (2014). Presynaptic alpha7 nicotinic acetylcholine receptors enhance hippocampal mossy fiber glutamatergic transmission via PKA activation. *The Journal of Neuroscience*, 34(1):124–133.

Chrobak, J. J., Stackman, R. W., and Walsh, T. J. (1989). Intraseptal administration of muscimol produces dose-dependent memory impairments in the rat. *Behavioral and Neural Biology*, 52(3):357–369.

Claiborne, B. J., Amaral, D. G., and Cowan, W. M. (1990). Quantitative, three-dimensional analysis of granule cell dendrites in the rat dentate gyrus. *The Journal of Comparative Neurology*, 302(2):206–219.

Cobb, S. R. and Davies, C. H. (2005). Cholinergic modulation of hippocampal cells and circuits. *The Journal of Physiology*, 562(1):81–88.

Colgin, L. L., Denninger, T., Fyhn, M., Hafting, T., Bonnevie, T., Jensen, O., Moser, M.-B., and Moser, E. I. (2009). Frequency of gamma oscillations routes flow of information in the hippocampus. *Nature*, 462(7271):353–357.

Colom, L. V., Castaneda, M. T., Reyna, T., Hernandez, S., and Garrido-sanabria, E. (2005). Characterization of medial septal glutamatergic neurons and their projection to the hippocampus. *Synapse*, 58(3):151–164.

Colom, L. V., Nassif-Caudarella, S., Dickson, C. T., Smythe, J. W., and Bland, B. H. (1991). *In vivo* intrahippocampal microinfusion of carbachol and bicuculline induces theta-like oscillations in the septally deafferented hippocampus. *Hippocampus*, 1(4):381–390.

Csicsvari, J., Hirase, H., Czurko, A., and Buzsáki, G. (1998). Reliability and state dependence of pyramidal cell-interneuron synapses in the hippocampus: an ensemble approach in the behaving rat. *Neuron*, 21(1):179–189.

Csicsvari, J., Hirase, H., Mamiya, A., and Buzsáki, G. (2000). Ensemble patterns of hippocampal CA3-CA1 neurons during sharp wave-associated population events. *Neuron*, 28(2):585–594.

Cutsuridis, V. and Poirazi, P. (2015). A computational study on how theta modulated inhibition can account for the long temporal windows in the entorhinal-hippocampal loop. *Neurobiology of Learning and Memory*.

Dasari, S. and Gulledge, A. T. (2011). M1 and M4 receptors modulate hippocampal pyramidal neurons. *Journal of Neurophysiology*, 105(2):779–792.

Davies, P. (1979). Neurotransmitter-related enzymes in senile dementia of the Alzheimer type. *Brain Research*, 171(2):319–327.

Donovick, P. J. (1968). Effects of localized septal lesions on hippocampal EEG activity and behavior in rats. *Journal of Comparative and Physiological Psychology*, 66(3):569–578.

Ego-Stengel, V. and Wilson, M. A. (2010). Disruption of ripple-associated hippocampal activity during rest impairs spatial learning in the rat. *Hippocampus*, 20(1):1–10.

Egorov, A. V., Hamam, B. N., Fransén, E., Hasselmo, M. E., and Alonso, A. A. (2002). Graded persistent activity in entorhinal cortex neurons. *Nature*, 420(6912):173–178.

Ekstrom, A. D., Caplan, J. B., Ho, E., Shattuck, K., Fried, I., and Kahana, M. J. (2005). Human hippocampal theta activity during virtual navigation. *Hippocampus*, 15(7):881–889.

Ferencz, I., Leanza, G., Nanobashvili, A., Kokaia, Z., Kokaia, M., and Lindvall, O. (2001). Septal cholinergic neurons suppress seizure development in hippocampal kindling in rats: comparison with noradrenergic neurons. *Neuroscience*, 102(4):819–832.

Fernández de Sevilla, D., Cabezas, C., de Prada, A. N. O., Sánchez-Jiménez, A., and Buño, W. (2002). Selective muscarinic regulation of functional glutamatergic Schaffer collateral synapses in rat CA1 pyramidal neurons. *The Journal of Physiology*, 545(Pt 1):51–63.

Fisher, R. S., van Emde Boas, W., Blume, W., Elger, C., Genton, P., Lee, P., and Engel, J. (2005). Epileptic seizures and epilepsy: definitions proposed by the International League Against Epilepsy (ILAE) and the International Bureau for Epilepsy (IBE). *Epilepsia*, 46(4):470–472.

Flynn, D. D., Ferrari-DiLeo, G., Mash, D. C., and Levey, A. I. (1995). Differential regulation of molecular subtypes of muscarinic receptors in Alzheimer's disease. *Journal of Neurochemistry*, 64(4):1888–1891.

Fortin, N. J., Agster, K. L., and Eichenbaum, H. B. (2002). Critical role of the hippocampus in memory for sequences of events. *Nature neuroscience*, 5(5):458–462.

Fox, S. E. (1989). Membrane potential and impedance changes in hippocampal pyramidal cells during theta rhythm. *Experimental Brain Research*, 77(2):283–294.

Frazier, C. J., Rollins, Y. D., Breese, C. R., Leonard, S., Freedman, R., and Dunwiddie, T. V. (1998). Acetylcholine activates an alpha-bungarotoxin-sensitive nicotinic current in rat hippocampal interneurons, but not pyramidal cells. *The Journal of Neuroscience*, 18(4):1187–1195.

Frazier, C. J., Strowbridge, B. W., and Papke, R. L. (2003). Nicotinic receptors on local circuit neurons in dentate gyrus: a potential role in regulation of granule cell excitability. *Journal of neurophysiology*, 89(6):3018–3028.

Freund, T. F. (1989). GABAergic septohippocampal neurons contain parvalbumin. *Brain research*, 478(2):375–381.

Freund, T. F. and Antal, M. (1988). GABA-containing neurons in the septum control inhibitory interneurons in the hippocampus. *Nature*, 336(6195):170–173.

Freund, T. F. and Buzsáki, G. (1996). Interneurons of the hippocampus. *Hippocampus*, 6(4):347–470.

Freund, T. F. and Katona, I. (2007). Perisomatic inhibition. *Neuron*, 56(1):33–42.

Friedman, A., Behrens, C. J., and Heinemann, U. (2007). Cholinergic dysfunction in temporal lobe epilepsy. *Epilepsia*, 48 Suppl 5:126–130.

Frotscher, M. and Léránth, C. (1985). Cholinergic innervation of the rat hippocampus as revealed by choline acetyltransferase immunocytochemistry: a combined light and electron microscopic study. *The Journal of Comparative Neurology*, 239(2):237–246.

Frotscher, M., Schlander, M., and Léránth, C. (1986). Cholinergic neurons in the hippocampus. A combined light- and electron-microscopic immunocytochemical study in the rat. *Cell and Tissue Research*, 246(2):293–301.

Frotscher, M., Vida, I., and Bender, R. (2000). Evidence for the existence of non-GABAergic, cholinergic interneurons in the rodent hippocampus. *Neuroscience*, 96(1):27–31.

Fuentealba, P., Begum, R., Capogna, M., Jinno, S., Márton, L. F., Csicsvari, J., Thomson, A., Somogyi, P., and Klausberger, T. (2008). Ivy cells: a population of nitric-oxide-producing, slow-spiking GABAergic neurons and their involvement in hippocampal network activity. *Neuron*, 57(6):917–929.

Fujita, Y. and Sato, T. (1964). Intracellular records from hippocampal pyramidal cells in rabbit during theta rhythm activity. *Journal of Neurophysiology*, 27:1012–1025.

Fyhn, M., Hafting, T., Witter, M. P., Moser, E. I., and Moser, M.-B. (2008). Grid cells in mice. *Hippocampus*, 18(12):1230–1238.

Garrido Sanabria, E. R., Castañeda, M. T., Banuelos, C., Perez-Cordova, M. G., Hernandez, S., and Colom, L. V. (2006). Septal GABAergic neurons are selectively vulnerable to pilocarpine-induced status epilepticus and chronic spontaneous seizures. *Neuroscience*, 142(3):871–883.

Gidon, A. and Segev, I. (2012). Principles governing the operation of synaptic inhibition in dendrites. *Neuron*, 75(2):330–341.

Giocomo, L. M. and Hasselmo, M. E. (2005). Nicotinic modulation of glutamatergic synaptic transmission in region CA3 of the hippocampus. *European Journal of Neuroscience*, 22(6):1349–1356.

Giovannini, M. G., Rakovska, A., Benton, R. S., Pazzagli, M., Bianchi, L., and Pepeu, G. (2001). Effects of novelty and habituation on acetylcholine, GABA, and glutamate release from the frontal cortex and hippocampus of freely moving rats. *Neuroscience*, 106(1):43–53.

Girardeau, G., Benchenane, K., Wiener, S. I., Buzsáki, G., and Zugaro, M. B. (2009). Selective suppression of hippocampal ripples impairs spatial memory. *Nature Neuroscience*, 12(10):1222–1223.

Givens, B. and Olton, D. S. (1994). Local modulation of basal forebrain: effects on working and reference memory. *The Journal of Neuroscience*, 14(6):3578–3587.

Gorelova, N. and Reiner, P. B. (1996). Role of the afterhyperpolarization in control of discharge properties of septal cholinergic neurons *in vitro*. *Journal of Neurophysiology*, 75(2):695–706.

Grandchamp, R. and Delorme, A. (2011). Single-trial normalization for event-related spectral decomposition reduces sensitivity to noisy trials. *Frontiers in Psychology*, 2.

Gray, R., Rajan, A. S., Radcliffe, K. A., Yakehiro, M., and Dani, J. A. (1996). Hippocampal synaptic transmission enhanced by low concentrations of nicotine. *Nature*, 383(6602):713–716.

Green, A., Ellis, K. A., Ellis, J., Bartholomeusz, C. F., Ilic, S., Croft, R. J., Phan, K. L., and Nathan, P. J. (2005). Muscarinic and nicotinic receptor modulation of object and spatial n-back working memory in humans. *Pharmacology, Biochemistry, and Behavior*, 81(3):575–584.

Green, J. D. and Arduini, A. A. (1954). Hippocampal electrical activity in arousal. *Journal of Neurophysiology*, 17(6):533–557.

Green, K. F. and Rawlins, J. N. (1979). Hippocampal theta in rats under urethane: generators and phase relations. *Electroencephalography and Clinical Neurophysiology*, 47(4):420–429.

Griffith, W. H. and Matthews, R. T. (1986). Electrophysiology of AChE-positive neurons in basal forebrain slices. *Neuroscience Letters*, 71(2):169–174.

Grybko, M., Sharma, G., and Vijayaraghavan, S. (2010). Functional distribution of nicotinic receptors in CA3 region of the hippocampus. *Journal of molecular neuroscience : MN*, 40(1-2):114–120.

Gulledge, A. T. and Kawaguchi, Y. (2007). Phasic cholinergic signaling in the hippocampus: functional homology with the neocortex? *Hippocampus*, 17(5):327–332.

Hafting, T., Fyhn, M., Molden, S., Moser, M.-B., and Moser, E. I. (2005). Microstructure of a spatial map in the entorhinal cortex. *Nature*, 436(7052):801–806.

Hajszan, T., Alreja, M., and Leranth, C. (2004). Intrinsic vesicular glutamate transporter 2-immunoreactive input to septohippocampal parvalbumin-containing neurons: Novel glutamatergic local circuit cells. *Hippocampus*, 14(4):499–509.

Han, Z. S., Buhl, E. H., Lörinczi, Z., and Somogyi, P. (1993). A high degree of spatial selectivity in the axonal and dendritic domains of physiologically identified local-circuit neurons in the dentate gyrus of the rat hippocampus. *The European Journal of Neuroscience*, 5(5):395–410.

Hangya, B., Borhegyi, Z., Nóra Szilágyi, Freund, T. F., and Varga, V. (2009). GABAergic neurons of the medial septum lead the hippocampal network during theta activity. *The Journal of Neuroscience*, 29(25):8094–8102.

Harris, K. D., Henze, D. A., Csicsvari, J., Hirase, H., and Buzsáki, G. (2000). Accuracy of tetrode spike separation as determined by simultaneous intracellular and extracellular measurements. *Journal of Neurophysiology*, 84(1):401–414.

Hasselmo (1999). Neuromodulation: acetylcholine and memory consolidation. *Trends in cognitive sciences*, 3(9):351–359.

Hasselmo, M. E. (2006). The role of acetylcholine in learning and memory. *Curr Opin Neurobiol*, 16(6):710–715.

Hasselmo, M. E., Bodelón, C., and Wyble, B. P. (2002). A proposed function for hippocampal theta rhythm: separate phases of encoding and retrieval enhance reversal of prior learning. *Neural computation*, 14(4):793–817.

Hasselmo, M. E. and Schnell, E. (1994). Laminar selectivity of the cholinergic suppression of synaptic transmission in rat hippocampal region CA1: computational modeling and brain slice physiology. *The Journal of Neuroscience*, 14(6):3898–3914.

Hasselmo, M. E. and Stern, C. E. (2013). Theta rhythm and the encoding and retrieval of space and time. *NeuroImage*.

Hájos, N., Papp, E. C., Acsády, L., Levey, A. I., and Freund, T. F. (1998). Distinct interneuron types express m2 muscarinic receptor immunoreactivity on their dendrites or axon terminals in the hippocampus. *Neuroscience*, 82(2):355–376.

Hölscher, C., Anwyl, R., and Rowan, M. J. (1997). Stimulation on the positive phase of hippocampal theta rhythm induces long-term potentiation that can be depotentiated by stimulation on the negative phase in area CA1 *in vivo*. *The Journal of Neuroscience*, 17(16):6470–6477.

Huerta, P. T. and Lisman, J. E. (1995). Bidirectional synaptic plasticity induced by a single burst during cholinergic theta oscillation in CA1 *in vitro*. *Neuron*, 15(5):1053–1063.

Huh, C. Y. L., Goutagny, R., and Williams, S. (2010). Glutamatergic neurons of the mouse medial septum and diagonal band of Broca synaptically drive hippocampal pyramidal cells: relevance for hippocampal theta rhythm. *The Journal of neuroscience*, 30(47):15951–15961.

Hyman, J. M., Wyble, B. P., Goyal, V., Rossi, C. A., and Hasselmo, M. E. (2003). Stimulation in hippocampal region CA1 in behaving rats yields long-term potentiation when delivered to the peak of theta and long-term depression when delivered to the trough. *The Journal of Neuroscience*, 23(37):11725–11731.

Ikonen, S., McMahan, R., Gallagher, M., Eichenbaum, H., and Tanila, H. (2002). Cholinergic system regulation of spatial representation by the hippocampus. *Hippocampus*, 12(3):386–397.

Isaac, J. T., Nicoll, R. A., and Malenka, R. C. (1995). Evidence for silent synapses: implications for the expression of LTP. *Neuron*, 15(2):427–434.

Jackson, J., Amilhon, B., Goutagny, R., Bott, J.-B., Manseau, F., Kortleven, C., Bressler, S. L., and Williams, S. (2014). Reversal of theta rhythm flow through intact hippocampal circuits. *Nature Neuroscience*, 17(10):1362–1370.

Jadhav, S. P., Kemere, C., German, P. W., and Frank, L. M. (2012). Awake hippocampal sharp-wave ripples support spatial memory. *Science (New York, N.Y.)*, 336(6087):1454–1458.

Ji, D. and Dani, J. A. (2000). Inhibition and disinhibition of pyramidal neurons by activation of nicotinic receptors on hippocampal interneurons. *Journal of Neurophysiology*, 83(5):2682–2690.

Ji, D., Lape, R., and Dani, J. A. (2001). Timing and location of nicotinic activity enhances or depresses hippocampal synaptic plasticity. *Neuron*, 31(1):131–141.

Jinno, S. and Kosaka, T. (2002). Immunocytochemical characterization of hippocamposeptal projecting GABAergic nonprincipal neurons in the mouse brain: a retrograde labeling study. *Brain Research*, 945(2):219–231.

Jones, M. W. and Wilson, M. A. (2005a). Phase precession of medial prefrontal cortical activity relative to the hippocampal theta rhythm. *Hippocampus*, 15(7):867–873.

Jones, M. W. and Wilson, M. A. (2005b). Theta rhythms coordinate hippocampal–prefrontal interactions in a spatial memory task. *PLoS Biol*, 3(12):e402.

Jones, S. and Yakel, J. L. (1997). Functional nicotinic ACh receptors on interneurones in the rat hippocampus. *The Journal of Physiology*, 504(Pt 3):603–610.

Jouvet, M. (1969). Biogenic amines and the states of sleep. *Science (New York, N.Y.)*, 163(3862):32–41.

Jung, R. and Kornmüller, A. E. (1938). Eine Methodik der Ableitung lokalisierter Potentialschwankungen aus subcorticalen Hirngebieten. *Archiv für Psychiatrie und Nervenkrankheiten*, 109(1):1–30.

Kaduszkiewicz, H., Zimmermann, T., Beck-Bornholdt, H.-P., and van den Bussche, H. (2005). Cholinesterase inhibitors for patients with Alzheimer's disease: systematic review of randomised clinical trials. *BMJ (Clinical research ed.)*, 331(7512):321–327.

Kahana, M. J., Sekuler, R., Caplan, J. B., Kirschen, M., and Madsen, J. R. (1999). Human theta oscillations exhibit task dependence during virtual maze navigation. *Nature*, 399(6738):781–784.

Kalappa, B. I., Gusev, A. G., and Uteshev, V. V. (2010). Activation of functional alpha7-containing nAChRs in hippocampal CA1 pyramidal neurons by physiological levels of choline in the presence of PNU-120596. *PloS One*, 5(11):e13964.

Kamondi, A., Acsády, L., Wang, X. J., and Buzsáki, G. (1998). Theta oscillations in somata and dendrites of hippocampal pyramidal cells *in vivo*: activity-dependent phase-precession of action potentials. *Hippocampus*, 8(3):244–261.

Kawakami, R., Shinohara, Y., Kato, Y., Sugiyama, H., Shigemoto, R., and Ito, I. (2003). Asymmetrical allocation of NMDA receptor epsilon2 subunits in hippocampal circuitry. *Science (New York, N.Y.)*, 300(5621):990–994.

Köhler, C., Chan-Palay, V., and Wu, J. Y. (1984). Septal neurons containing glutamic acid decarboxylase immunoreactivity project to the hippocampal region in the rat brain. *Anatomy and Embryology*, 169(1):41–44.

Kiss, J., Patel, A. J., Baimbridge, K. G., and Freund, T. F. (1990a). Topographical localization of neurons containing parvalbumin and choline acetyltransferase in the medial septum-diagonal band region of the rat. *Neuroscience*, 36(1):61–72.

Kiss, J., Patel, A. J., and Freund, T. F. (1990b). Distribution of septohippocampal neurons containing parvalbumin or choline acetyltransferase in the rat brain. *The Journal of Comparative Neurology*, 298(3):362–372.

Klausberger, T., Magill, P. J., Márton, L. F., Roberts, J. D. B., Cobden, P. M., Buzsáki, G., and Somogyi, P. (2003). Brain-state- and cell-type-specific firing of hippocampal interneurons in vivo. *Nature*, 421(6925):844–848.

Klausberger, T. and Somogyi, P. (2008). Neuronal diversity and temporal dynamics: the unity of hippocampal circuit operations. *Science*, 321(5885):53–57.

Klink, R. and Alonso, A. (1997). Muscarinic modulation of the oscillatory and repetitive firing properties of entorhinal cortex layer II neurons. *Journal of Neurophysiology*, 77(4):1813–1828.

Kocsis, B., Bragin, A., and Buzsáki, G. (1999). Interdependence of multiple theta generators in the hippocampus: a partial coherence analysis. *The Journal of Neuroscience*, 19(14):6200–6212.

Kohara, K., Pignatelli, M., Rivest, A. J., Jung, H.-Y., Kitamura, T., Suh, J., Frank, D., Kajikawa, K., Mise, N., Obata, Y., Wickersham, I. R., and Tonegawa, S. (2014). Cell type-specific genetic and optogenetic tools reveal hippocampal CA2 circuits. *Nature Neuroscience*, 17(2):269–279.

Konopacki, J., MacIver, M. B., Bland, B. H., and Roth, S. H. (1987). Carbachol-induced EEG 'theta' activity in hippocampal brain slices. *Brain Research*, 405(1):196–198.

Korovaichuk, A., Makarova, J., Makarov, V. A., Benito, N., and Herreras, O. (2010). Minor contribution of principal excitatory pathways to hippocampal LFPs in the anesthetized rat: a combined independent component and current source density study. *Journal of Neurophysiology*, 104(1):484–497.

Kowalczyk, T., Bocian, R., and Konopacki, J. (2013). The generation of theta rhythm in hippocampal formation maintained *in vitro*. *The European Journal of Neuroscience*, 37(5):679–699.

Kramis, R., Vanderwolf, C. H., and Bland, B. H. (1975). Two types of hippocampal rhythmical slow activity in both the rabbit and the rat: relations to behavior and effects of atropine, diethyl ether, urethane, and pentobarbital. *Experimental Neurology*, 49(1 Pt 1):58–85.

Kremin, T. and Hasselmo, M. E. (2007). Cholinergic suppression of glutamatergic synaptic transmission in hippocampal region CA3 exhibits laminar selectivity: Implication for hippocampal network dynamics. *Neuroscience*, 149(4):760–767.

Kunec, S., Hasselmo, M. E., and Kopell, N. (2005). Encoding and Retrieval in the CA3 Region of the Hippocampus: A Model of Theta-Phase Separation. *Journal of Neurophysiology*, 94(1):70–82.

Lapray, D., Lasztoczi, B., Lagler, M., Viney, T. J., Katona, L., Valenti, O., Hartwich, K., Borhegyi, Z., Somogyi, P., and Klausberger, T. (2012). Behavior-dependent specialization of identified hippocampal interneurons. *Nature neuroscience*, 15(9):1265–1271.

Lawrence, J. J., Grinspan, Z. M., Statland, J. M., and McBain, C. J. (2006a). Muscarinic receptor activation tunes mouse stratum oriens interneurones to amplify spike reliability. *The Journal of physiology*, 571(Pt 3):555–562.

Lawrence, J. J., Statland, J. M., Grinspan, Z. M., and McBain, C. J. (2006b). Cell type-specific dependence of muscarinic signalling in mouse hippocampal stratum oriens interneurones. *The Journal of Physiology*, 570(Pt 3):595–610.

Lawson, V. H. and Bland, B. H. (1993). The role of the septohippocampal pathway in the regulation of hippocampal field activity and behavior: analysis by the intraseptal microinfusion of carbachol, atropine, and procaine. *Experimental Neurology*, 120(1):132–144.

Leao, R. N., Targino, Z. H., Colom, L. V., and Fisahn, A. (2014). Interconnection and Synchronization of Neuronal Populations in the Mouse Medial Septum/Diagonal Band of Brocca. *Journal of Neurophysiology*, page jn.00367.2014.

Lee, H. S., Ghetti, A., Pinto-Duarte, A., Wang, X., Dziewczapolski, G., Galimi, F., Huitron-Resendiz, S., Piña-Crespo, J. C., Roberts, A. J., Verma, I. M., Sejnowski, T. J., and Heinemann, S. F. (2014). Astrocytes contribute to gamma oscillations and recognition memory. *Proceedings of the National Academy of Sciences of the United States of America*, 111(32):E3343–3352.

Lega, B. C., Jacobs, J., and Kahana, M. (2012). Human hippocampal theta oscillations and the formation of episodic memories. *Hippocampus*, 22(4):748–761.

Lein, E. S., Callaway, E. M., Albright, T. D., and Gage, F. H. (2005). Redefining the boundaries of the hippocampal CA2 subfield in the mouse using gene expression and 3-dimensional reconstruction. *The Journal of Comparative Neurology*, 485(1):1–10.

Leranth, C., Deller, T., and Buzsáki, G. (1992). Intraseptal connections redefined: lack of a lateral septum to medial septum path. *Brain Research*, 583(1-2):1–11.

Leung, L. S., Shen, B., Rajakumar, N., and Ma, J. (2003). Cholinergic activity enhances hippocampal long-term potentiation in CA1 during walking in rats. *The Journal of Neuroscience*, 23(28):9297–9304.

Lever, C., Burton, S., Jeewajee, A., O'Keefe, J., and Burgess, N. (2009). Boundary vector cells in the subiculum of the hippocampal formation. *The Journal of Neuroscience*, 29(31):9771–9777.

Levey, A. I., Edmunds, S. M., Koliatsos, V., Wiley, R. G., and Heilman, C. J. (1995). Expression of m1-m4 muscarinic acetylcholine receptor proteins in rat hippocampus and regulation by cholinergic innervation. *The Journal of Neuroscience*, 15(5):4077–4092.

Liebe, S., Hoerzer, G. M., Logothetis, N. K., and Rainer, G. (2012). Theta coupling between V4 and prefrontal cortex predicts visual short-term memory performance. *Nature Neuroscience*, 15(3):456–462, S1–2.

Lisman, J. E. and Jensen, O. (2013). The theta-gamma neural code. *Neuron*, 77(6):1002–1016.

Lovett-Barron, M., Kaifosh, P., Kheirbek, M. A., Danielson, N., Zaremba, J. D., Reardon, T. R., Turi, G. F., Hen, R., Zemelman, B. V., and Losonczy, A. (2014). Dendritic inhibition in the hippocampus supports fear learning. *Science (New York, N.Y.)*, 343(6173):857–863.

Léránth, C. and Frotscher, M. (1989). Organization of the septal region in the rat brain: cholinergic-GABAergic interconnections and the termination of hippocampo-septal fibers. *The Journal of Comparative Neurology*, 289(2):304–314.

MacDonald, C. J., Lepage, K. Q., Eden, U. T., and Eichenbaum, H. (2011). Hippocampal "time cells" bridge the gap in memory for discontiguous events. *Neuron*, 71(4):737–749.

Makarov, V. A., Makarova, J., and Herreras, O. (2010). Disentanglement of local field potential sources by independent component analysis. *Journal of Computational Neuroscience*, 29(3):445–457.

Mankin, E. A., Sparks, F. T., Slayyeh, B., Sutherland, R. J., Leutgeb, S., and Leutgeb, J. K. (2012). Neuronal code for extended time in the hippocampus. *Proceedings of the National Academy of Sciences of the United States of America*, 109(47):19462–19467.

Manseau, F., Danik, M., and Williams, S. (2005). A functional glutamatergic neurone network in the medial septum and diagonal band area. *The Journal of Physiology*, 566(Pt 3):865–884.

Markram, H. and Segal, M. (1990). Electrophysiological characteristics of cholinergic and non-cholinergic neurons in the rat medial septum-diagonal band complex. *Brain Research*, 513(1):171–174.

Marrosu, F., Portas, C., Mascia, M. S., Casu, M. A., Fà, M., Giagheddu, M., Imperato, A., and Gessa, G. L. (1995). Microdialysis measurement of cortical and hippocampal acetylcholine release during sleep-wake cycle in freely moving cats. *Brain Research*, 671(2):329–332.

Martinello, K., Huang, Z., Lujan, R., Tran, B., Watanabe, M., Cooper, E. C., Brown, D. A., and Shah, M. M. (2015). Cholinergic afferent stimulation induces axonal function plasticity in adult hippocampal granule cells. *Neuron*.

McQuiston, A. R. (2014). Acetylcholine release and inhibitory interneuron activity in hippocampal CA1. *Frontiers in Synaptic Neuroscience*, 6.

McQuiston, A. R. and Madison, D. V. (1999a). Muscarinic receptor activity has multiple effects on the resting membrane potentials of CA1 hippocampal interneurons. *The Journal of Neuroscience*, 19(14):5693–5702.

McQuiston, A. R. and Madison, D. V. (1999b). Nicotinic receptor activation excites distinct subtypes of interneurons in the rat hippocampus. *The Journal of Neuroscience*, 19(8):2887–2896.

Mendez, M. and Lim, G. (2003). Seizures in elderly patients with dementia: epidemiology and management. *Drugs & Aging*, 20(11):791–803.

Mesulam, M. M., Mufson, E. J., Wainer, B. H., and Levey, A. I. (1983). Central cholinergic pathways in the rat: an overview based on an alternative nomenclature (Ch1-Ch6). *Neuroscience*, 10(4):1185–1201.

Miller, J. W., Turner, G. M., and Gray, B. C. (1994). Anticonvulsant effects of the experimental induction of hippocampal theta activity. *Epilepsy Research*, 18(3):195–204.

Mizumori, S. J. and Williams, J. D. (1993). Directionally selective mnemonic properties of neurons in the lateral dorsal nucleus of the thalamus of rats. *The Journal of Neuroscience*, 13(9):4015–4028.

Mizuseki, K. and Buzsáki, G. (2013). Preconfigured, skewed distribution of firing rates in the hippocampus and entorhinal cortex. *Cell Reports*, 4(5):1010–1021.

Mizuseki, K., Sirota, A., Pastalkova, E., and Buzsáki, G. (2009). Theta oscillations provide temporal windows for local circuit computation in the entorhinal-hippocampal loop. *Neuron*, 64(2):267–280.

Morris, N. P., Harris, S. J., and Henderson, Z. (1999). Parvalbumin-immunoreactive, fast-spiking neurons in the medial septum/diagonal band complex of the rat: intracellular recordings *in vitro*. *Neuroscience*, 92(2):589–600.

Motley, S. E. and Kirwan, C. B. (2012). A parametric investigation of pattern separation processes in the medial temporal lobe. *The Journal of Neuroscience*, 32(38):13076–13085.

Nagel, G., Brauner, M., Liewald, J. F., Adeishvili, N., Bamberg, E., and Gottschalk, A. (2005). Light activation of channelrhodopsin-2 in excitable cells of Caenorhabditis elegans triggers rapid behavioral responses. *Current biology: CB*, 15(24):2279–2284.

Nagode, D. A., Tang, A.-H., Karson, M. A., Klugmann, M., and Alger, B. E. (2011). Optogenetic release of ACh induces rhythmic bursts of perisomatic IPSCs in hippocampus. *PloS One*, 6(11):e27691.

Nagode, D. A., Tang, A.-H., Yang, K., and Alger, B. E. (2014). Optogenetic identification of an intrinsic cholinergically driven inhibitory oscillator sensitive to cannabinoids and opioids in hippocampal CA1. *The Journal of Physiology*, 592(Pt 1):103–123.

Navarrete, M., Perea, G., de Sevilla, D. F., Gómez-Gonzalo, M., Núñez, A., Martín, E. D., and Araque, A. (2012). Astrocytes mediate *in vivo* cholinergic-induced synaptic plasticity. *PLoS Biology*, 10(2):e1001259.

Ohno, M., Yamamoto, T., and Watanabe, S. (1993). Blockade of hippocampal nicotinic receptors impairs working memory but not reference memory in rats. *Pharmacology Biochemistry and Behavior*, 45(1):89–93.

Ohno, M., Yamamoto, T., and Watanabe, S. (1994). Blockade of hippocampal M1 muscarinic receptors impairs working memory performance of rats. *Brain Research*, 650(2):260–266.

O'Keefe, J. and Dostrovsky, J. (1971). The hippocampus as a spatial map. Preliminary evidence from unit activity in the freely-moving rat. *Brain Research*, 34(1):171–175.

O'Keefe, J. and Nadel, L. (1978). *The Hippocampus as a Cognitive Map*. Oxford University Press, Oxford : New York.

O'Keefe, J. and Recce, M. L. (1993). Phase relationship between hippocampal place units and the EEG theta rhythm. *Hippocampus*, 3(3):317–330.

Oostenveld, R., Fries, P., Maris, E., and Schoffelen, J.-M. (2011). FieldTrip: Open source software for advanced analysis of MEG, EEG, and invasive electrophysiological data. *Computational intelligence and neuroscience*, 2011:156869.

Orr, G., Rao, G., Houston, F. P., McNaughton, B. L., and Barnes, C. A. (2001). Hippocampal synaptic plasticity is modulated by theta rhythm in the fascia dentata of adult and aged freely behaving rats. *Hippocampus*, 11(6):647–654.

Otmakhova, N. A., Otmakhov, N., and Lisman, J. E. (2002). Pathway-specific properties of AMPA and NMDA-mediated transmission in CA1 hippocampal pyramidal cells. *The Journal of Neuroscience*, 22(4):1199–1207.

Pavlides, C., Greenstein, Y. J., Grudman, M., and Winson, J. (1988). Long-term potentiation in the dentate gyrus is induced preferentially on the positive phase of theta-rhythm. *Brain Research*, 439(1-2):383–387.

Paxinos, G. and Franklin, K. B. J. (2008). *The Mouse Brain in Stereotaxic Coordinates, Compact, Third Edition: The coronal plates and diagrams*. Academic Press, Amsterdam, 3rd edition.

Penttonen and Buzsáki, G. (2003). Natural logarithmic relationship between brain oscillators. *Thalamus & Related Systems*, 2(02):145–152.

Perry, E. K., Morris, C. M., Court, J. A., Cheng, A., Fairbairn, A. F., McKeith, I. G., Irving, D., Brown, A., and Perry, R. H. (1995). Alteration in nicotine binding sites in Parkinson's disease, Lewy body dementia and Alzheimer's disease: possible index of early neuropathology. *Neuroscience*, 64(2):385–395.

Petsche, H., Stumpf, C., and Gogolak, G. (1962). The significance of the rabbit's septum as a relay station between the midbrain and the hippocampus. I. The control of hippocampus arousal activity by the septum cells. *Electroencephalography and Clinical Neurophysiology*, 14:202–211.

Pettit, D. L., Shao, Z., and Yakel, J. L. (2001). Beta-amyloid(1-42) peptide directly modulates nicotinic receptors in the rat hippocampal slice. *The Journal of Neuroscience: The Official Journal of the Society for Neuroscience*, 21(1):RC120.

Picciotto, M. R., Higley, M. J., and Mineur, Y. S. (2012). Acetylcholine as a neuromodulator: cholinergic signaling shapes nervous system function and behavior. *Neuron*, 76(1):116–129.

Pinto, L., Goard, M. J., Estandian, D., Xu, M., Kwan, A. C., Lee, S.-H., Harrison, T. C., Feng, G., and Dan, Y. (2013). Fast modulation of visual perception by basal forebrain cholinergic neurons. *Nature Neuroscience*, 16(12):1857–1863.

Quirk, G. J., Muller, R. U., Kubie, J. L., and Ranck, J. B. (1992). The positional firing properties of medial entorhinal neurons: description and comparison with hippocampal place cells. *The Journal of Neuroscience*, 12(5):1945–1963.

Quiroga, R. Q., Nadasdy, Z., and Ben-Shaul, Y. (2004). Unsupervised spike detection and sorting with wavelets and superparamagnetic clustering. *Neural Comput*, 16(8):1661–1687.

Radcliffe, K. A., Fisher, J. L., Gray, R., and Dani, J. A. (1999). Nicotinic modulation of glutamate and GABA synaptic transmission of hippocampal neurons. *Annals of the New York Academy of Sciences*, 868:591–610.

Raghavachari, S., Kahana, M. J., Rizzuto, D. S., Caplan, J. B., Kirschen, M. P., Bourgeois, B., Madsen, J. R., and Lisman, J. E. (2001). Gating of human theta oscillations by a working memory task. *The Journal of Neuroscience*, 21(9):3175–3183.

Raiteri, M., Leardi, R., and Marchi, M. (1984). Heterogeneity of presynaptic muscarinic receptors regulating neurotransmitter release in the rat brain. *Journal of Pharmacology and Experimental Therapeutics*, 228(1):209–214.

Rogers, J. L. and Kesner, R. P. (2003). Cholinergic modulation of the hippocampus during encoding and retrieval. *Neurobiology of Learning and Memory*, 80(3):332–342.

Rouse, S. T., Edmunds, S. M., Yi, H., Gilmor, M. L., and Levey, A. I. (2000). Localization of M2 muscarinic acetylcholine receptor protein in cholinergic and non-cholinergic terminals in rat hippocampus. *Neuroscience Letters*, 284(3):182–186.

Rouse, S. T., Gilmor, M. L., and Levey, A. I. (1998). Differential presynaptic and postsynaptic expression of M1–M4 muscarinic acetylcholine receptors at the perforant pathway/granule cell synapse. *Neuroscience*, 86(1):221–232.

Rutishauser, U., Ross, I. B., Mamelak, A. N., and Schuman, E. M. (2010). Human memory strength is predicted by theta-frequency phase-locking of single neurons. *Nature*, 464(7290):903–907.

Rye, D. B., Wainer, B. H., Mesulam, M. M., Mufson, E. J., and Saper, C. B. (1984). Cortical projections arising from the basal forebrain: A study of cholinergic and noncholinergic components employing combined retrograde tracing and immunohistochemical localization of choline acetyltransferase. *Neuroscience*, 13(3):627–643.

Sargolini, F., Fyhn, M., Hafting, T., McNaughton, B. L., Witter, M. P., Moser, M.-B., and Moser, E. I. (2006). Conjunctive representation of position, direction, and velocity in entorhinal cortex. *Science (New York, N.Y.)*, 312(5774):758–762.

Scharfman, H. E. (2007). The CA3 "backprojection" to the dentate gyrus. *Progress in Brain Research*, 163:627–637.

Scharfman, H. E. and Myers, C. E. (2012). Hilar mossy cells of the dentate gyrus: a historical perspective. *Frontiers in neural circuits*, 6:106.

Schomburg, E. W., Fernández-Ruiz, A., Mizuseki, K., Berényi, A., Anastassiou, C. A., Koch, C., and Buzsáki, G. (2014). Theta phase segregation of input-specific gamma patterns in entorhinal-hippocampal networks. *Neuron*, 84(2):470–485.

Scoville, W. B. and Milner, B. (1957). Loss of recent memory after bilateral hippocampal lesions. *Journal of neurology, neurosurgery, and psychiatry*, 20(1):11–21.

Seguela, P., Wadiche, J., Dineley-Miller, K., Dani, J. A., and Patrick, J. W. (1993). Molecular cloning, functional properties, and distribution of rat brain alpha7: a nicotinic cation channel highly permeable to calcium. *The Journal of Neuroscience*, 13(2):596–604.

Serafin, M., Williams, S., Khateb, A., Fort, P., and Mühlethaler, M. (1996). Rhythmic firing of medial septum non-cholinergic neurons. *Neuroscience*, 75(3):671–675.

Serrano-Pozo, A., Frosch, M. P., Masliah, E., and Hyman, B. T. (2011). Neuropathological alterations in Alzheimer disease. *Cold Spring Harbor Perspectives in Medicine*, 1(1):a006189.

Sershen, H., Balla, A., Lajtha, A., and Vizi, E. S. (1997). Characterization of nicotinic receptors involved in the release of noradrenaline from the hippocampus. *Neuroscience*, 77(1):121–130.

Sharma, G. and Vijayaraghavan, S. (2001). Nicotinic cholinergic signaling in hippocampal astrocytes involves calcium-induced calcium release from intracellular stores. *Proceedings of the National Academy of Sciences of the United States of America*, 98(7):4148–4153.

Sharma, G. and Vijayaraghavan, S. (2003). Modulation of presynaptic store calcium induces release of glutamate and postsynaptic firing. *Neuron*, 38(6):929–939.

Sharp, P. E. and Green, C. (1994). Spatial correlates of firing patterns of single cells in the subiculum of the freely moving rat. *The Journal of Neuroscience*, 14(4):2339–2356.

Shen, J.-x. and Yakel, J. L. (2012). Functional alpha7 nicotinic ACh receptors on astrocytes in rat hippocampal CA1 slices. *Journal of Molecular Neuroscience*, 48(1):14–21.

Shin, J., Kim, D., Bianchi, R., Wong, R. K. S., and Shin, H.-S. (2005). Genetic dissection of theta rhythm heterogeneity in mice. *Proceedings of the National Academy of Sciences of the United States of America*, 102(50):18165–18170.

Shinoe, T., Matsui, M., Taketo, M. M., and Manabe, T. (2005). Modulation of synaptic plasticity by physiological activation of M1 muscarinic acetylcholine receptors in the mouse hippocampus. *The Journal of Neuroscience*, 25(48):11194–11200.

Shinohara, Y., Hirase, H., Watanabe, M., Itakura, M., Takahashi, M., and Shigemoto, R. (2008). Left-right asymmetry of the hippocampal synapses with differential subunit allocation of glutamate receptors. *Proceedings of the National Academy of Sciences of the United States of America*, 105(49):19498–19503.

Shipton, O. A., El-Gaby, M., Apergis-Schoute, J., Deisseroth, K., Bannerman, D. M., Paulsen, O., and Kohl, M. M. (2014). Left-right dissociation of hippocampal memory processes in mice. *Proceedings of the National Academy of Sciences of the United States of America*, 111(42):15238–15243.

Shirey, J. K., Xiang, Z., Orton, D., Brady, A. E., Johnson, K. A., Williams, R., Ayala, J. E., Rodriguez, A. L., Wess, J., Weaver, D., Niswender, C. M., and Conn, P. J. (2008). An allosteric potentiator of M4 mAChR modulates hippocampal synaptic transmission. *Nature Chemical Biology*, 4(1):42–50.

Siapas, A. G., Lubenov, E. V., and Wilson, M. A. (2005). Prefrontal phase locking to hippocampal theta oscillations. *Neuron*, 46(1):141–151.

Sirota, A., Montgomery, S., Fujisawa, S., Isomura, Y., Zugaro, M., and Buzsáki, G. (2008). Entrainment of neocortical neurons and gamma oscillations by the hippocampal theta rhythm. *Neuron*, 60(4):683–697.

Skaggs, W. E., McNaughton, B. L., Wilson, M. A., and Barnes, C. A. (1996). Theta phase precession in hippocampal neuronal populations and the compression of temporal sequences. *Hippocampus*, 6(2):149–172.

Smith, M. L., Deadwyler, S. A., and Booze, R. M. (1993). 3-D reconstruction of the cholinergic basal forebrain system in young and aged rats. *Neurobiology of Aging*, 14(4):389–392.

Solstad, T., Boccara, C. N., Kropff, E., Moser, M.-B., and Moser, E. I. (2008). Representation of geometric borders in the entorhinal cortex. *Science*, 322(5909):1865–1868.

Soltesz, I. and Deschenes, M. (1993). Low- and high-frequency membrane potential oscillations during theta activity in CA1 and CA3 pyramidal neurons of the rat hippocampus under ketamine-xylazine anesthesia. *Journal of Neurophysiology*, 70(1):97 –116.

Sotty, F., Danik, M., Manseau, F., Laplante, F., Quirion, R., and Williams, S. (2003). Distinct electrophysiological properties of glutamatergic, cholinergic and GABAergic rat septohippocampal neurons: novel implications for hippocampal rhythmicity. *J Physiol*, 551(Pt 3):927–943.

Stackman, R. W. and Taube, J. S. (1998). Firing properties of rat lateral mammillary single units: head direction, head pitch, and angular head velocity. *The Journal of Neuroscience*, 18(21):9020–9037.

Stancampiano, R., Cocco, S., Cugusi, C., Sarais, L., and Fadda, F. (1999). Serotonin and acetylcholine release response in the rat hippocampus during a spatial memory task. *Neuroscience*, 89(4):1135–1143.

Stark, E., Eichler, R., Roux, L., Fujisawa, S., Rotstein, H. G., and Buzsáki, G. (2013). Inhibition-induced theta resonance in cortical circuits. *Neuron*, 80(5):1263–1276.

Suzuki, W. A., Miller, E. K., and Desimone, R. (1997). Object and place memory in the macaque entorhinal cortex. *Journal of Neurophysiology*, 78(2):1062–1081.

Swanson, L. W. and Cowan, W. M. (1979). The connections of the septal region in the rat. *The Journal of Comparative Neurology*, 186(4):621–655.

Szabó, G. G., Holderith, N., Gulyás, A. I., Freund, T. F., and Hájos, N. (2010). Distinct synaptic properties of perisomatic inhibitory cell types and their different modulation by cholinergic receptor activation in the CA3 region of the mouse hippocampus. *European Journal of Neuroscience*, 31(12):2234–2246.

Takata, N., Mishima, T., Hisatsune, C., Nagai, T., Ebisui, E., Mikoshiba, K., and Hirase, H. (2011). Astrocyte calcium signaling transforms cholinergic modulation to cortical plasticity *in vivo*. *The Journal of Neuroscience*, 31(49):18155–18165.

Tang, A.-H., Karson, M. A., Nagode, D. A., McIntosh, J. M., Uebele, V., Renger, J., Klugmann, M., Milner, T. A., and Alger, B. E. (2011). Nerve terminal nAChRs initiate quantal GABA release from perisomatic interneurons by activating axonal T-type (Ca_v3) Ca^{2+} channels and Ca^{2+} release from stores. *The Journal of Neuroscience*, 31(38):13546–13561.

Taube, J. S. (1995). Head direction cells recorded in the anterior thalamic nuclei of freely moving rats. *The Journal of Neuroscience*, 15(1 Pt 1):70–86.

Taube, J. S. and Muller, R. U. (1998). Comparisons of head direction cell activity in the postsubiculum and anterior thalamus of freely moving rats. *Hippocampus*, 8(2):87–108.

Taube, J. S., Muller, R. U., and Ranck, J. B. (1990). Head-direction cells recorded from the postsubiculum in freely moving rats. II. Effects of environmental manipulations. *The Journal of Neuroscience*, 10(2):436–447.

Tort, A. B. L., Komorowski, R. W., Manns, J. R., Kopell, N. J., and Eichenbaum, H. (2009). Theta-gamma coupling increases during the learning of item-context associations. *Proc Natl Acad Sci U S A*.

Tóth, K., Borhegyi, Z., and Freund, T. F. (1993). Postsynaptic targets of GABAergic hippocampal neurons in the medial septum-diagonal band of broca complex. *The Journal of neuroscience*, 13(9):3712–3724.

Tóth, K., Freund, T. F., and Miles, R. (1997). Disinhibition of rat hippocampal pyramidal cells by GABAergic afferents from the septum. *The Journal of Physiology*, 500(Pt 2):463–474.

Tulving, E. (2002). Episodic memory: from mind to brain. *Annual review of psychology*, 53:1–25.

Tulving, E. and Donaldson, W. (1972). *Organization of Memory*. Academic Press Inc, New York.

Umbriaco, D., Garcia, S., Beaulieu, C., and Descarries, L. (1995). Relational features of acetylcholine, noradrenaline, serotonin and GABA axon terminals in the stratum radiatum of adult rat hippocampus (CA1). *Hippocampus*, 5(6):605–620.

Vallés, A. S., Borroni, M. V., and Barrantes, F. J. (2014). Targeting brain alpha7 nicotinic acetylcholine receptors in Alzheimer's disease: Rationale and current status. *CNS drugs*, 28(11):975–987.

Van Der Zee, E. A., De Jong, G. I., Strosberg, A. D., and Luiten, P. G. (1993). Muscarinic acetylcholine receptor-expression in astrocytes in the cortex of young and aged rats. *Glia*, 8(1):42–50.

van Loo, K. M. J., Schaub, C., Pernhorst, K., Yaari, Y., Beck, H., Schoch, S., and Becker, A. J. (2012). Transcriptional regulation of T-type calcium channel $Ca_v3.2$: bi-directionality by early growth response 1 (Egr1) and repressor element 1 (RE-1) protein-silencing transcription factor (REST). *The Journal of biological chemistry*, 287(19):15489–15501.

Vandecasteele, M., Varga, V., Berényi, A., Papp, E., Barthó, P., Venance, L., Freund, T. F., and Buzsáki, G. (2014). Optogenetic activation of septal cholinergic neurons suppresses sharp wave ripples and enhances theta oscillations in the hippocampus. *Proceedings of the National Academy of Sciences of the United States of America*.

Vanderwolf, C. H. (1969). Hippocampal electrical activity and voluntary movement in the rat. *Electroencephalography and Clinical Neurophysiology*, 26(4):407–418.

Varga, V., Hangya, B., Kránitz, K., Ludányi, A., Zemankovics, R., Katona, I., Shigemoto, R., Freund, T. F., and Borhegyi, Z. (2008). The presence of pacemaker HCN channels identifies theta rhythmic GABAergic neurons in the medial septum. *The Journal of physiology*, 586(16):3893–3915.

Vertes, R. P. and Kocsis, B. (1997). Brainstem-diencephalo-septohippocampal systems controlling the theta rhythm of the hippocampus. *Neuroscience*, 81(4):893–926.

Vilaró, M. T., Palacios, J. M., and Mengod, G. (1990). Localization of M5 muscarinic receptor mRNA in rat brain examined by in situ hybridization histochemistry. *Neuroscience Letters*, 114(2):154–159.

Villarreal, D. M., Gross, A. L., and Derrick, B. E. (2007). Modulation of CA3 afferent inputs by novelty and theta rhythm. *The Journal of neuroscience: the official journal of the Society for Neuroscience*, 27(49):13457–13467.

Volterra, A. and Meldolesi, J. (2005). Astrocytes, from brain glue to communication elements: the revolution continues. *Nature Reviews Neuroscience*, 6(8):626–640.

Wainer, B. H., Levey, A. I., Rye, D. B., Mesulam, M. M., and Mufson, E. J. (1985). Cholinergic and non-cholinergic septohippocampal pathways. *Neuroscience Letters*, 54(1):45–52.

Wall, S. J., Yasuda, R. P., Li, M., Ciesla, W., and Wolfe, B. B. (1992). Differential regulation of subtypes m1-m5 of muscarinic receptors in forebrain by chronic atropine administration. *The Journal of Pharmacology and Experimental Therapeutics*, 262(2):584–588.

Wang, H. Y., Lee, D. H., D'Andrea, M. R., Peterson, P. A., Shank, R. P., and Reitz, A. B. (2000a). Beta-amyloid(1-42) binds to alpha7 nicotinic acetylcholine receptor with high affinity. Implications for Alzheimer's disease pathology. *The Journal of Biological Chemistry*, 275(8):5626–5632.

Wang, H. Y., Lee, D. H., Davis, C. B., and Shank, R. P. (2000b). Amyloid peptide A beta(1-42) binds selectively and with picomolar affinity to alpha7 nicotinic acetylcholine receptors. *Journal of Neurochemistry*, 75(3):1155–1161.

Wess, J. (2003). Novel insights into muscarinic acetylcholine receptor function using gene targeting technology. *Trends in Pharmacological Sciences*, 24(8):414–420.

Widmer, H., Ferrigan, L., Davies, C. H., and Cobb, S. R. (2006). Evoked slow muscarinic acetylcholinergic synaptic potentials in rat hippocampal interneurons. *Hippocampus*, 16(7):617–628.

Wiener, S. I. (1993). Spatial and behavioral correlates of striatal neurons in rats performing a self-initiated navigation task. *The Journal of Neuroscience*, 13(9):3802–3817.

Williams, P. A., Larimer, P., Gao, Y., and Strowbridge, B. W. (2007). Semilunar granule cells: glutamatergic neurons in the rat dentate gyrus with axon collaterals in the inner molecular layer. *The Journal of neuroscience*, 27(50):13756–13761.

Winson, J. (1978). Loss of hippocampal theta rhythm results in spatial memory deficit in the rat. *Science (New York, N.Y.)*, 201(4351):160–163.

Woolf, N. J. (1991). Cholinergic systems in mammalian brain and spinal cord. *Progress in Neurobiology*, 37(6):475–524.

Woolf, N. J., Eckenstein, F., and Butcher, L. L. (1984). Cholinergic systems in the rat brain: I. projections to the limbic telencephalon. *Brain Research Bulletin*, 13(6):751–784.

Wu, M., Hajszan, T., Leranth, C., and Alreja, M. (2003a). Nicotine recruits a local glutamatergic circuit to excite septohippocampal GABAergic neurons. *The European Journal of Neuroscience*, 18(5):1155–1168.

Wu, M., Newton, S. S., Atkins, J. B., Xu, C., Duman, R. S., and Alreja, M. (2003b). Acetylcholinesterase inhibitors activate septohippocampal GABAergic neurons via muscarinic but not nicotinic receptors. *The Journal of Pharmacology and Experimental Therapeutics*, 307(2):535–543.

Wu, M., Shanabrough, M., Leranth, C., and Alreja, M. (2000). Cholinergic excitation of septohippocampal GABA but not cholinergic neurons: implications for learning and memory. *The Journal of Neuroscience*, 20(10):3900–3908.

Yamasaki, M., Matsui, M., and Watanabe, M. (2010). Preferential Localization of Muscarinic M1 Receptor on Dendritic Shaft and Spine of Cortical Pyramidal Cells and Its Anatomical Evidence for Volume Transmission. *The Journal of Neuroscience*, 30(12):4408–4418.

Yoshida, M., Fransén, E., and Hasselmo, M. E. (2008). mGluR-dependent persistent firing in entorhinal cortex layer III neurons. *The European Journal of Neuroscience*, 28(6):1116–1126.

Yoshida, M. and Hasselmo, M. E. (2009). Persistent firing supported by an intrinsic cellular mechanism in a component of the head direction system. *The Journal of Neuroscience*, 29(15):4945–4952.

Young, B. J., Otto, T., Fox, G. D., and Eichenbaum, H. (1997). Memory representation within the parahippocampal region. *The Journal of Neuroscience*, 17(13):5183–5195.

Zhang, H., Lin, S.-C., and Nicolelis, M. A. L. (2010). Spatiotemporal coupling between hippocampal acetylcholine release and theta oscillations *in vivo*. *The Journal of Neuroscience*, 30(40):13431–13440.

Zoli, M., Léna, C., Picciotto, M. R., and Changeux, J. P. (1998). Identification of four classes of brain nicotinic receptors using beta2 mutant mice. *The Journal of Neuroscience*, 18(12):4461–4472.

C. Contributions

The *in vitro* patch clamp recordings of identified ChAT$^+$ and PV$^+$ MSvDB neurons during optogenetic stimulation of these neurons (see Figures 3.2, 3.22, 3.27, and Table 3.1), and the patch clamp recordings of unidentified MSvDB neurons during optogenetic stimulation of ChAT$^+$ MSvDB neurons and fibers (see Figures 3.23, 3.24, and 3.25) were carried out by Oliver Braganza and Milan Pabst. Classification of unidentified neurons into putative PV$^+$ and non-PV$^+$ MSvDB neurons based on electrophysiological properties was done by Dr. Heinz Beck, who was blind to the effects of the optogenetic stimulation.